Early time dynamics & longitudinal structure of high-energy heavy-ion collisions

UNIVERSITÄT BIELEFELD

Pragya Singh

A thesis submitted in
partial fulfillment of the requirements
for the degree of Doctor rerum naturalium

Department of Physics
Universität Bielefeld

Referee 1   JProf. Sören Schlichting
Referee 2   Prof. Nicolas Borghini

August 24, 2021

Acknowledgement

Declaration

I, Pragya Singh, declare that this thesis titled "Early time dynamics & longitudinal structure of high-energy heavy-ion collisions" has not been previously submitted to any examination office. Only the sources and literature indicated have been used. The results presented in the thesis are largely based on

- S. Schlichting and P. Singh, "3-D structure of the Glasma initial state – Breaking boost-invariance by collisions of extended shock waves in classical Yang-Mills theory" Phys.Rev.D 103 (2021) 1, 014003, arxiv.2010.11172 [1]

and the following manuscripts, that are currently being finalized

- A. Ipp, D. Müller, S. Schlichting and P. Singh, "Space-time structure of $3+1$ D color fields in high energy nuclear collisions"

- B. Schenke, S. Schlichting and P. Singh, "Longitudinal structure of initial state in p-Pb collisions"

Signed:

_____

Date:

_____

Abstract

We investigate the out-of-equilibrium dynamics of heavy-ion collisions by performing real-time lattice simulations, accompanied by analytical considerations within the framework of the Color Glass Condensate (CGC) effective theory of QCD. The central aim of this work is to relax the assumption of boost invariance and to gain insights into the longitudinal structure of the fireball.

In the first main part of the thesis, we simulate the 3+1 D classical Yang-Mills dynamics of the collisions of longitudinally extended nuclei, described by eikonal color charges in the CGC framework. By varying the longitudinal thickness of the colliding nuclei, we discuss the violations of boost invariance and explore how the boost invariant high-energy limit is approached. Subsequently, we develop a more realistic model of the 3 D color charge distributions, and explore the rapidity profiles and the longitudinal fluctuations that emerges naturally within our framework.

In the second main part, we perform an analytic calculation of the color fields in heavy-ion collisions, by considering the collision of extended nuclei in the dilute limit of the Color Glass Condensate effective field theory of high-energy QCD. Based on general analytic expressions for the color fields in the forward light cone, we evaluate the rapidity profile of the transverse pressure within a simple specific model of the nuclear collision geometry and compare our results to 3+1D classical Yang-Mills simulations.

In the third part of this thesis, we study the rapidity dependence of initial state momentum correlations and event-by-event geometry in p+Pb collisions at LHC energies ($\sqrt{s} = 5.02$ TeV) within the 3+1 D IP-Glasma model. We find that the event geometry is correlated across large rapidity intervals whereas initial state momentum correlations are relatively short range in rapidity. Based on our results, we discuss implications for the relevance of both effects in explaining the origin of collective phenomena in small systems.

List of Figures

Table of Contents

Chapter 1

Introduction

The standard model of particle physics provides a satisfactory picture of the elementary particles and the interaction between these particles. However, the current comprehension of the Quantum Chromo Dynamics (QCD), the theory of strong interaction between quarks and gluon, is only partially amenable. Understanding the properties of QCD at extreme condition is challenging as it would require profound knowledge into the non-equilibrium dynamics of the system. This work aims to contribute towards the understanding of non-equilibrium dynamics of QCD which prevails at a very early stage in heavy-ion collisions.

The heavy-ion collision (HIC) experiment carried out at the Large Hadron Collider (LHC) at CERN and the Relativistic Heavy Ion Collider (RHIC) at BNL, collide nuclei at high center of mass energies to create extreme conditions of high temperature and density, in order to understand the theory of QCD beyond the standard vacuum, and to recreate the universe a few microseconds after the Big Bang. This miniature version of microsecond old universe creates a new state of matter called Quark Gluon Plasma (QGP) [2, 3], which consists of quasi-free quarks and gluons. QGP is a consequence of one of interesting properties of non-Abelian gauge theories, asymptotic freedom [4, 5], which weakens the interaction between the constituent partons as the energy scale increases. Understanding the creation and evolution of QGP is one of motivations behind HIC. The QGP created in HICs behaves as a nearly perfect fluid for a significant part of its lifetime [6–8]. Since we are interested in the addressing the out of equilibrium dynamics, we will focus on establishing the initial condition for QGP formation rather than accessing its properties.

A pictorial representation of heavy-ion collision is shown in Fig. 1.1 where two Lorentz contracted nuclei are coming towards each other almost at the speed of light. Each incident nuclei consists of many quarks (q), anti-quarks ($\bar{q}$) and gluons, which due to quantum fluctuations leads to additional $q\bar{q}$ pairs and gluons. This highly complex system of partons (quarks and gluons) on passing through each other create longitudinal fields which then eventually decays to $q\bar{q}$ and gluons. Clearly, this highly entropic system is far from local thermal equilibrium and hence the resultant partons melts to form Quark Gluon Plasma. Now as the two nuclei moves further away from each other, the QGP expands and cools down. Subsequently, the QGP temperature falls below the QCD cross over temperature ($T_c \simeq 155$ MeV) [9] at which the QGP falls apart into hadrons, which following a few hadronic re-scatterings, freely streams towards the detector.

However, due to fundamental confining property of QCD, the deconfined QGP is not directly observed and hence one relies on the rapidity and transverse momentum spectrum of the hadronic remnants of QGP state which helps us in understanding the creation and evolution of quark-gluon plasma. HICs are multi-messenger experiments which in addition to typical soft hadron production allow to study e.g. hard probes (jets), electromagnetic probes (photons, dileptons). As QCD is such a complex theory [10], characterisation of HICs from a single theory is currently not possible and hence one calls for the development of effective theories/ models to describe the formation and evolution of a fireball. In this context, a nucleus-nucleus collision can be roughly said to go through these three main stages:

(i) *Pre-equilibrium*: This describes the earliest stage which entails the description of dense colliding nuclei along with the initial partonic collision that evolves to provide a state sufficiently close to equilibrium [12]. The system is in this state for incredibly short time $\tau \sim 0.1 - 1.0$ fm/c.

(ii) *Hydrodynamic expansion*: This comprises of QGP which being very close to a perfect fluid, can be described by the relativistic hydrodynamics. Here the fireball expands rapidly and cools down unless the temperature is below some critical value, at which the deconfined plasma hadronizes [13]
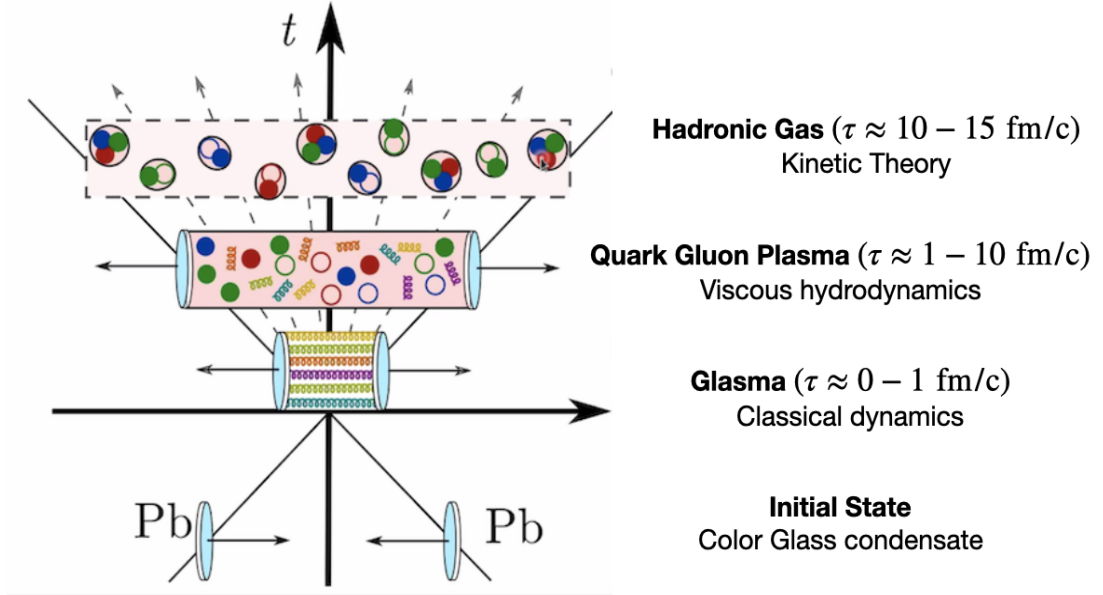
Figure 1.1: Different stages of heavy-ion collisions along with the theory used to study them. This figure is from A Mazeliauskas' talk [11]

(iii) *Hadronic stage & Freeze-out*: Here, the system undergoes multiple inelastic and elastic collision, prior to reaching a state of kinetic freeze-out [14] where hadrons can no longer interact and then streams towards the detector.

As clearly seen, most of the space-time dynamics of the fireball is dominated by hydrodynamic expansion which in turn requires the macroscopic properties of initial state such as energy momentum tensor $(T^{\mu\nu})$, conserved currents (J^{μ}) as an input. Therefore we are more interested in studying the pre-equilibrium or the initial stage of HIC, without which the proper characterisation of QGP properties is not possible. Although, there are numerous models for the initial state [15–21] which basically relies on the assumption that at a very high energy, collision is boost invariant and hence the system can be treated as a collision of infinitesimally thin shock waves. This effectively simplifies the problem to a great detail and helps in understanding the transverse dynamics of the fireball but the resultant initial condition is constructively $2 + 1$D. However, recent observation at RHIC and LHC [22–25] supports the theoretical understanding that exempting the boost-invariant approximation, will naturally give rise to the longitudinal dynamics.

Among various models that provide the framework for studying the initial condition,

the most accepted one is the Color-Glass condensate (CGC) [26, 27], an effective theory of high energy QCD that describes the dense nuclei prior to the collision and their initial energy deposition. The underlying idea behind CGC is the separation of scales at very high energy into hard and soft constituents. The hard constituents like valence quark or large-x (longitudinal momentum fraction) gluons carries most of the momentum of the colliding hadron and are frozen due to time dilation. These large-x partons radiates soft gluons which leads to an increasing gluon density at small-x. When two such dense nuclei collide at high-energy, a dense state of gluonic matter, called Glasma [28] is created, and due to large occupation number their dynamics can be treated classically. The CGC theory and other theoretical and numerical techniques relevant to this thesis are introduced in Chapter 2

CGC has lead to a development of various successful models like impact-parameter dependent Glasma (IP-Glasma) [18, 19] and KLN [15, 16], that have revolutionized our understanding for a broad range of observable at mid-rapidity, like event-by-event anisotropic flow [29, 30] and charged hadron multiplicity [19, 31] at LHC energies. Within the CGC framework, various (semi-) analytical studies [32–38] have been performed in context of characterising the properties of Glasma at very early times. Despite the substantial improvements in modelling of a realistic nucleus [18] or using event-by-event viscous hydrodynamics simulations [39, 40], our knowledge is limited in regards to the longitudinal dynamics of the fireball or the rapidity dependence of the observable.

The experiments at RHIC and recent measurements of longitudinal fluctuations at LHC, have triggered an interest in studying 3D initial state geometry. The rapidity dependence have been considered in various ways: either by generalising the boost invariant IP-Glasma model to 3+1D by including the JIMWLK evolution of the incoming nuclear distribution [41, 42], by introducing source terms that deposits energy over a range of space-time rapidities [43], or by including correction to eikonal approximation based on finite width of the target [44, 45]. Although these models provide some handle in the rapidity direction, still a very limited number of first principle insight is available beyond the boost invariant approximation.

A natural way to comprehend the longitudinal dynamics of fireball is by relaxing

the assumption of boost-invariant collision. The Chapter 3 of this thesis deals with the development of a framework to perform 3+1D classical Yang-Mills simulations of the initial energy deposition in heavy-ion collisions, which as in [46–48] take into account the finite longitudinal extent of the colliding nuclei. Within a simple model of the color charge distribution of each nucleus, we perform a detailed investigation of the dynamics during and shortly after the collision as a function of the longitudinal thickness of the colliding nuclei, and contrast our results with the high-energy limit of infinitely thin shocks. Subsequently, we develop a more physical model that connects the color charge distributions in the colliding nuclei to parton distributions inside the nuclei, and we discuss the rapidity profiles and fluctuations that emerge within this model.

With a framework for incorporating longitudinal dynamics and a realistic model for heavy-ion collision, we could have done a lot of phenomenology to understand the initialization of collision at the LHC and RHIC energies. Since the simulations are very expensive, we gained new analytical insights into the 3+1 D structure in Chapter 4 by investigating the problem perturbatively in the dilute limit. By solving the linearized Yang-Mills equation, we obtain the gauge fields solution in the future light-cone which can be used to compute the different components of energy momentum tensor. Within a simple model of color charge distribution, we focus exclusively on transverse pressure and examine the effectiveness of our analytical results by comparing them to non-perturbative classical Yang-Mills equations. Subsequently, we obtain further insights into the dependence of rapidity profiles on various limits of our nuclear model.

In last few decades, experiments have provided various signature for the QGP formation in the heavy ion collision [49–51], among these the most prominent ones are anisotropic flow and jet quenching. For a particle with low transverse momenta p_T, the angular correlation between pseudorapidity $\Delta\eta$ and azimuthal angle $\Delta\phi$ shows peak centered around ($\Delta\phi = 0$), known as ridge. The natural explanation for this long-range correlation or anisotropic flow in heavy-ion collision is provided by relativistic hydrodynamics where the anisotropy in final state momentum distributions is explained entirely via the response to the initial state geometry in the transverse

plane. More recently, similar signals to those in heavy ion collisions have been found in the produced particle spectra of small collision systems, e.g. p+A, or even p+p collisions [52–55] where applicability of hydrodynamics is highly debated as the system size decreases and gradients become larger [56]. An alternative mechanisms that could generate the observed anisotropies without requiring the creation of a nearly perfect fluid, is given by CCG [57–73] where anisotropic momentum distributions are the result of color correlations in the incoming nuclei's gluon distributions.

Event geometry and initial state correlations have been invoked as possible explanations of long range azimuthal correlations observed in high multiplicity p-p and p-Pb collisions. Chapter 5 shows an application of a 3+1D CGC model to the phenomenological study of azimuthal correlations in p+Pb collisions. In order to make the simulations computationally feasible, we follow the approach of extending the IP-Glasma model to 3 D using JIMWLK rapidity evolution of the incoming nuclear gluon distribution [41] and study the rapidity dependence of initial state momentum correlations and event-by-event geometry in $\sqrt{s} = 5.02$ TeV p+Pb collisions. The whole new idea is to exploit the longitudinal dependence of the correlations to investigate to what extent the above plausible mechanism could explain the collectivity in small systems.

Finally, in Chapter 6 we have summarized our important results and given an overview of the future expansion of the work done.

Chapter 2

Theoretical Background

In this chapter, we introduce the fundamental concepts that are needed in the later chapters. We start by summarizing the basics of QCD in Section 2.1 and then give a broad overview of CGC along with the introduction of a model for high energy description of a nucleus in Section 2.2. For this simple model, we derive the evolution equation for the boost invariant Glasma in Section 2.3 and later layout the technique for solving these equations on lattice in Section 2.4. Before we embark on a journey into 3+1 D, we try to summarise some of the salient features of boost-invariant Glasma in Section 2.5 and then briefly introduce the JIMWLK equation in Section 2.6

2.1 Preliminary Quantum Chromodynamics

Before we start, we would like to emphasise that throughout this thesis, we will be working in natural units i.e $\hbar = 1$ and $c = 1$, and unless stated we will employ the Minkowski coordinate $x^\mu = (t, x, y, z)$ with space-time metric defined as

$$g_{\mu\nu} = \text{diag}(+1, -1, -1, -1)$$

QCD – the theory of strong interaction of colored quarks and gluons, is a non-Abelian gauge theory based on $SU(3)$ symmetry group. The QCD Lagrangian is given as

$$\mathcal{L}_{QCD} = \int d^4x \left(-\frac{1}{4} F^a_{\mu\nu}(x) F^{\mu\nu a}(x) - \sum \bar{\psi}^{\bar{a}}_f(x) \left(i \slashed{D}^{\bar{a}\bar{b}} - m_f \delta_{\bar{a}\bar{b}} \right) \psi^{\bar{b}}_f(x) \right) \tag{2.1}$$

where $\bar{\psi}_f$ are the fermion fields with flavoured index f characterising the different quark species u, d, s, c, b, t, with different mass and electric charge. The quarks are considered in fundamental representation such that the color indices $\bar{a}, \bar{b}$ runs from 1 to $N_c = 3$. The operator $\slashed{D}^{\bar{a}\bar{b}} \equiv \gamma^\mu D_\mu^{\bar{a}\bar{b}}$ involves the Dirac γ-matrices and the covariant derivative which acts on the fermion field as

$$D_\mu^{\bar{a}\bar{b}} \psi_{\bar{b}} = \partial_\mu \psi^{\bar{a}} - ig(A_\mu)^{\bar{a}\bar{b}} \psi_{\bar{b}} \tag{2.2}$$

where g is the coupling constant. The carriers of the interaction are the gluons fields $A_\mu(x)$ which themselves are coloured and hence self interacting. For a local gauge transformation $G(x) \in SU(N_c)$ with

$$GG^\dagger = \mathbb{1} = G^\dagger G$$

$$\det G = 1$$

the gauge fields transforms under adjoint representation of the $SU(N_c)$ group as

$$A_\mu^{(G)}(x) = G(x)A_\mu(x)G^\dagger(x) + \frac{i}{g}G(x)\partial_\mu G^\dagger(x) \tag{2.3}$$

The algebra element A_μ can be expressed in terms of its color components as

$$A_\mu(x) = A_\mu^a(x)t^a \tag{2.4}$$

where the color index a runs from 1 to $N_c^2 - 1$. The generators t^a of the $su(N_c)$ Lie algebra in the fundamental representation are $N_c \times N_c$ traceless Hermitian matrices with normalization

$$\mathrm{Tr}[t^a, t^b] = \frac{1}{2}\delta^{ab} \tag{2.5}$$

The generators in $SU(2)$ gauge group are related to Pauli Matrices by $t^a = \sigma^a/2$ whereas in $SU(3)$ are related to Gell-Mann matrices λ^a by $t^a = \lambda^a/2$. The commutation relation of generators

$$[t^a, t^b] = if^{abc}t^c \tag{2.6}$$

involves antisymmetric structure constants f^{abc} which for the $SU(2)$ gauge group are given in terms of Levi-Civita symbol as $f^{abc} = \epsilon^{abc}$. The anti-commutators of the generators are related to symmetric structure constant d^{abc}

$$\{t^a, t^b\} = \frac{1}{N_c}\delta^{ab} + d^{abc}t^c \tag{2.7}$$

The component of field strength tensor $F_{\mu\nu} = F_{\mu\nu}^a t^a$ in Eq. (2.1) is given as

$$F_{\mu\nu}^a(x) = \partial_\mu A_\nu^a - \partial_\nu A_\mu^a + gf^{abc}A_\mu^b A_\nu^c \tag{2.8}$$

We note that the non-Abelian nature of QCD leads to non-linear term in the above equation. By using the transformation of the gauge fields Eq. (2.3), one can easily show that the fields strength tensor transforms as

$$F_{\mu\nu}^{(G)}(x) = G(x)F_{\mu\nu}(x)G^\dagger(x) \tag{2.9}$$

The above construction manifests the invariance of QCD Lagrangian under a local $SU(3)$ gauge transformation. The two terms in Eq. (2.1) are individually referred as Yang-Mills fields and the matter fields. For rest of the dissertation, we will only consider the Yang-Mills part of the Lagrangian and the coupling of the fermionic field with the bosonic field will be replaced by the source terms of the form $J_\mu A^\mu$.

We note that the Yang-Mills Lagrangian due to the self-interacting nature of gluons already gives rise to cubic and quartic order terms. The reason for neglecting the quark degree of freedom will become more obvious from the following section where we will see that the out-of-equilibrium study of heavy-ion collision is dominated by gluonic contribution. Moreover, at weak coupling, the large occupation numbers of partons leads to classical-statistical approximation, but fermions due to Pauli exclusion principle wouldn't fit into the classical description and hence the lattice discretization of fermions will be significantly more challenging [74, 75] and therefore, beyond the scope of present work.

2.2 Color Glass Condensate

We note that for further discussion, we will be using light-cone coordinates (LC) $(x^+, x^-, \boldsymbol{x}_\perp)$ which can be expressed in terms of Minkowski coordinate

$$x^\pm = \frac{t+z}{\sqrt{2}} \qquad \boldsymbol{x}_\perp = \boldsymbol{x}_\perp \tag{2.10}$$

and the corresponding metric is given as:

$$g^{\mu\nu} = \begin{pmatrix} 0 & 1 & 0 & 0 \\ 1 & 0 & 0 & 0 \\ 0 & 0 & -1 & 0 \\ 0 & 0 & 0 & -1 \end{pmatrix} \tag{2.11}$$

The partonic content of the nucleus is an important element in the study of a hadronic collision and is explored via Deep Inelastic Scattering (DIS) experiment where in order to be visible in the scattering process, the timescale of the interaction should be greater than the inverse of the resolution of the probe i.e the virtuality of the photon (Q). Besides the valence quantum numbers of nucleons, one observes fluctuations of sea quarks and additional gluons in a DIS experiment [76]. Intuitively, the observation at DIS can be pictured as in Fig. 2.1 where on probing the hadron at higher energies, one resolves more and more short lived fluctuations. The time dilation affects the lifetime of the fluctuation and also ceases the interaction of the partons, due to which they appear to be asymptotically free during the hadronic collision, whereas Lorentz contraction compresses the geometry of the nucleon. The repercussion of these two effects have been observed at HERA [77, 78] in terms of an increase in gluon distribution number which mainly outnumbers the distribution measurement of any other partons like sea quarks.

As partonic content increases, calculating scattering amplitude becomes quite complicated with the perturbation theory as one has to keep track of fairly large number of Feynman diagrams. Therefore, despite the weak coupling, this regime of high parton density is treated non-perturbatively.
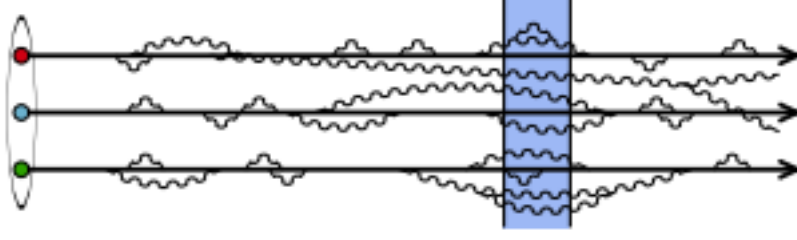
Figure 2.1: Fluctuations encountered in a highly boosted nucleon represented by wavy lines. Thick lines are the valence quarks. This figure is adapted from [27]

One may think, if gluon keeps on increasing, wouldn't it lead to an infinite cross section? The bound in the total cross section is provided by a dynamical scale known as saturation momentum Q_s which is much larger than the non-perturbative scale Λ_{QCD} where QCD becomes strongly coupled and intrinsically non-perturbative. When the gluon density becomes large as $x \to 0$, non linear effects like recombination of gluon becomes important. The saturation momentum measures the strength of the non-linear interaction among the gluons. To summarise, we start with x such that the momentum of virtual photon is much larger than the saturation momentum $(Q \gg Q_s)$. As x decreases the number of gluons increases and eventually there comes a time when $Q < Q_s$, in which case, the rise in the number of gluons becomes slow [79]. This is termed as saturation as the cross-section saturates [80, 81] because the number of the gluons stops growing.

An effective theory, Color Glass Condensate is used to study the processes in the saturation regime [26, 82]. CGC is based on the assumption that both projectile and target are in infinite momentum frame (IMF) i.e travelling at the speed of the light. In an IMF, x^+ is equivalent to time and the corresponding conjugate variable, p^- plays the role of energy. Now, if we consider a nucleus moving in $+z$ direction with a large line cone momentum P^+, then with the help of uncertainty principle we can deduce the temporal extent of the parton as

$$\tau = \frac{2xP^+}{\boldsymbol{k}_\perp^2} \tag{2.12}$$

where $x = p^+/P^+$ is the parton momentum fraction and p^+ is the momentum of parton. Similarly, the longitudinal extent is given as

$$\Delta x^- = \frac{1}{xP^+} \tag{2.13}$$

This points to the fact that there is a separation of scale between the soft gluon ($x \ll 1$) and hard partons ($x \sim 1$). As clear from above, small-x partons have a large longitudinal extent and therefore can resolve a lot of color charges. Similarly one finds

$$\tau|_{x \ll 1} \ll \tau|_{x \simeq 1} \tag{2.14}$$

In the high energy limit of a hadronic matter, time dilation ceases the evolution of hard or the large-x partons. Thus soft gluons (wee partons) sees the valence partons as frozen, infinitely thin sources of color charges. These large-x partons are then considered as an eikonal currents, moving along the light cone and are described by a color charge density $\rho^a(x)$ which retrieves the information of the color current. For a nucleus moving in $+z$ direction, the color current is given as

$$J_a^\mu(x) = \delta^{\mu+} \rho_a(x^-, \boldsymbol{x}_\perp) \tag{2.15}$$

where $\boldsymbol{x}_\perp = x, y$ denotes the transverse Lorentz indices and $a = 1, .., N_c^2 - 1$ are the color index. Since the valence partons are assumed to be static, the x^+ dependency no longer persists. The other components are not that relevant because of the choice of the frame which enhances the J^+ current by a Lorentz factor. The highly boosted nuclei will have a very narrow support along the x^- direction and hence in the ultra-relativistic limit, we can write

$$\rho_a(x^-, \boldsymbol{x}_\perp) = \delta(x^-)\rho_a(\boldsymbol{x}_\perp) \tag{2.16}$$

We would like to emphasise that these assumptions Eqs. (2.15) and (2.16) makes the system invariant under boosts. The main aim of the thesis is to add correction to this leading order eikonal approximation by taking finite nuclear thickness into

account.[1] With this source current, we can determine the pre-collision gauge field of the single nucleus using classical Yang-Mills equation

$$[D_\mu, F^{\mu\nu}] = J^\nu \tag{2.17}$$

We chose axial gauge $A^- = A_+ = 0$ along with a solution of the form $A^\mu(x^-, \boldsymbol{x}_\perp)$ based on the assumption that sources don't have any x^+ dependency. The $F^{\mu-}$ component of the field strength tensor vanishes because $A^- = 0$ and the ansatz has no x^+ dependence . The Yang-Mills equations then reads:

$$[D_-, F^{-+}] + [D_i, F^{i+}] = J^+ \tag{2.18}$$

$$[D_+, F^{+-}] + [D_i, F^{i-}] = 0 \tag{2.19}$$

$$[D_+, F^{+i}] + [D_-, F^{-i}] + [D_j, F^{ji}] = 0 \tag{2.20}$$

The second equation is trivial as both the terms are zero. Now in order to solve Eqs. (2.18) and (2.20), we adopt the additional gauge choice $A^i = 0$, which makes Eq. (2.20) trivial, while Eq. (2.18) becomes

$$\partial_i \partial^i A^+(x^-, \boldsymbol{x}_\perp) = \rho(x^-, \boldsymbol{x}_\perp) \tag{2.21}$$

To summarise, the overall solution of a *single* nucleus moving in right direction is given as

$$A^- = A^i = 0, \qquad A^+(x^-, \boldsymbol{x}_\perp) = -\frac{1}{\nabla_\perp^2} \rho(x^-, \boldsymbol{x}_\perp) \tag{2.22}$$

We see that this choice of gauge also preserves the current conservation equation

$$[D_\mu, J^\mu] = \partial_+ J^+ - ig[A_+, J^+] = 0 \tag{2.23}$$

Using Fourier transformation, we can explicitly solve the 2-dimensional Poisson equation appearing in Eq. (2.22).

$$A_a^+(x^-, \boldsymbol{x}_\perp) = \int \frac{d^2 \boldsymbol{k}_\perp}{(2\pi)^2} \frac{\tilde{\rho}_a(x^-, \boldsymbol{k}_\perp)}{\boldsymbol{k}_\perp^2} e^{i\boldsymbol{k}_\perp \boldsymbol{x}_\perp} \tag{2.24}$$

---

[1] Other sub-eikonal correction like $x^\pm$ dependence of color currents is beyond the scope of present work.

where we have defined the Fourier transform of the color charge density as

$$\tilde{\rho}_a(x^-, \boldsymbol{k}_\perp) = \int d^2\boldsymbol{x}_\perp \rho_a(x^-, \boldsymbol{x}_\perp)e^{-i\boldsymbol{k}_\perp \boldsymbol{x}_\perp} \tag{2.25}$$

It is clear from the above equations that the profile of function ρ sets the shape of the color field A^+. Even though the solution turns out to be quite simple in the Lorentz gauge, it turns out that light-cone ($A^\pm = 0$) or the axial gauge ($A^0 = 0$) turns out to more convenient for practical purposes. Hence, we need to find a gauge transformation $V(x)$ which eliminates the A^+ fields. Using gauge transformation properties

$$A^\mu(x) \to V(x)A^\mu(x)V^\dagger(x) + \frac{i}{g}V(x)\partial^\mu V^\dagger(x) \tag{2.26}$$

we find that this can be achieved by an x^+ independent gauge transformation of the form $V(x) = V(x^-, \boldsymbol{x}_\perp)$, such that it satisfies

$$\partial^+ V^\dagger(x^-, \boldsymbol{x}_\perp) = igA^+(x^-, \boldsymbol{x}_\perp)V^\dagger(x^-, \boldsymbol{x}_\perp) \tag{2.27}$$

The above equation has a following path-ordered solution

$$V(x^-, \boldsymbol{x}_\perp) = \mathcal{P}\exp\left(-ig\int_{-\infty}^{x^-} dy^- A^+(y^-, \boldsymbol{x}_\perp)\right) \tag{2.28}$$

and we use the following convention for path ordering: $A^\mu(x)A^\mu(y) = A^\mu(x)A^\mu(y)$ if $x > y$, i.e x comes later. The gauge transformation $V(x^-, \boldsymbol{x}_\perp)$ is termed as light-like Wilson line and is realized as the re-summation of multiple gluon interaction. The fields and the currents in the new gauge are obtained after applying the gauge transformation. The gauge fields reads

$$A^\pm_{LC} = 0 \qquad A^i_{LC}(x^-, \boldsymbol{x}_\perp) = \frac{i}{g}V(x^-, \boldsymbol{x}_\perp)\partial^i V^\dagger(x^-, \boldsymbol{x}_\perp) \tag{2.29}$$

where the subscript LC denotes the light cone gauge. The currents are given by

$$J^+_{LC}(x^-, \boldsymbol{x}_\perp) = V(x^-, \boldsymbol{x}_\perp)\rho(x^-, \boldsymbol{x}_\perp)V^\dagger(x^-, \boldsymbol{x}_\perp) \qquad J^-_{LC} = J^i_{LC} = 0 \tag{2.30}$$

One can obtain an explicit expression for the transverse fields as

$$A_{LC}^i(x^-, \boldsymbol{x}_\perp) = -\int_{-\infty}^{x^-} dy^- V(x^-, \boldsymbol{x}_\perp) \partial^i A^+(y^-, \boldsymbol{x}_\perp) V^\dagger(x^-, \boldsymbol{x}_\perp) \qquad (2.31)$$

We notice that in order to determine the color field, one must specify the form of color charge density $\rho(x)$. Thus, the CGC framework must include the description of the color charge density.

This idea of specifying the color charge along with treating them classically originates from the McLerran-Venugopalan (MV) model [83, 84]. The main argument that goes in the development of the model is that for small-x or large nucleus with atomic mass A, the density of valence quark degree of freedom per unit transverse area is very high and scales as $A^{1/3}$. As these color sources are associated with different nucleons, they must be uncorrelated in the longitudinal as well as the transverse direction for two different points in the transverse plane. Now since we are summing the contribution of many uncorrelated color charges, the central limit theorem states that the distribution functional $W[\rho]$ should be Gaussian

$$W[\rho] = \frac{1}{Z} \exp\left(-\int dx^- d^2\boldsymbol{x}_\perp \frac{\rho_a(x^-, \boldsymbol{x}_\perp)\rho_a(x^-, \boldsymbol{x}_\perp)}{2g^2\mu^2(x^-)} \right) \qquad (2.32)$$

where Z is a normalization constant and μ^2 – the only dimensionful parameter of the model, corresponds to the density of charge squared fluctuation per unit transverse area in between the slices x^- and $x^- + dx^-$ and

$$\int dx^- \mu^2(x^-) \sim A^{1/3} \qquad (2.33)$$

Based on a given distribution, the expectation value of an observable $\mathcal{O}$ is obtained by averaging over different realization of color charges as:

$$\langle \mathcal{O} \rangle = \int \mathcal{D}\rho \, \mathcal{O}[\rho] \, W[\rho] \qquad (2.34)$$

We can complete the description of the MV model by specifying the form of color

charges, which are viewed as a stochastic fluctuation, and therefore can be expressed in terms of the following correlation functions:

$$\langle \rho^a(x^-, \boldsymbol{x}_\perp) \rangle = 0 \tag{2.35}$$

$$\langle \rho^a(x^-, \boldsymbol{x}_\perp) \rho^b(y^-, \boldsymbol{y}_\perp) \rangle = g^2 \mu^2(x^-) \delta^{ab} \delta(x^- - y^-) \delta^{(2)}(\boldsymbol{x}_\perp - \boldsymbol{y}_\perp) \tag{2.36}$$

where the one point function reflects color neutrality whereas the two point function assumes large nucleus to be thin but with finite longitudinal support and transversely homogeneous color charges.

The MV model with the finite longitudinal support can be pictured as an ensemble of infinitesimal sheets of fluctuating color charges. For numerical simulations, one usually considers a heavy nucleus as N 2-dimensional sheets of uncorrelated color charges stacked on top of each other. Due to the path ordering involved in the definition of light-like Wilson line, one should be very careful in dealing with the MV model. This model due to its simplified assumption provides a good description for a heavy nucleus and helps in a better understanding of the small-x behaviour based on underlying principles of QCD.

With this, we can collect all the results for a single nucleus moving either in positive-z or negative-z direction. The color current and the gauge field in the covariant gauge is given as

$$J^{\mu,a}_{R,L}(x) = \delta^{\mu\pm} \rho^a_{R,L}(x^\mp, \boldsymbol{x}_\perp) \tag{2.37}$$

$$A^{\pm,a}_{R,L}(x^\mp, \boldsymbol{x}_\perp) = -\frac{1}{\nabla^2_\perp} \rho^a_{R,L}(x^\mp, \boldsymbol{x}_\perp) \tag{2.38}$$

Using Fourier transformation, we can rewrite the above solution as

$$A^{\pm,a}_{R,L}(x^\mp, \boldsymbol{x}_\perp) = \int \frac{d^2 \boldsymbol{k}_\perp}{(2\pi)^2} \frac{\tilde{\rho}^a_{R,L}(x^\mp, \boldsymbol{x}_\perp)}{\boldsymbol{k}^2_\perp} e^{i\boldsymbol{k}_\perp \cdot \boldsymbol{x}_\perp} \tag{2.39}$$

where the subscript R, L is used to denote the right $(+z)$ and the left $(-z)$ direction.

The corresponding solution of the gauge field in the LC or the axial gauge $A^{\pm} = A^0 = 0$ is given by

$$A^{i,a}_{R,L}(x^{\mp}, \boldsymbol{x}_{\perp}) = \frac{i}{g} V_{R,L}(x^{\mp}, \boldsymbol{x}_{\perp}) \partial^i V^{\dagger}_{R,L}(x^{\mp}, \boldsymbol{x}_{\perp}) \tag{2.40}$$

with the light-like Wilson line defined as

$$V_{R,L}(x^{\mp}, \boldsymbol{x}_{\perp}) = \mathcal{P} \exp\left(-ig \int_{-\infty}^{x^{\mp}} dy^{\mp} A^{\pm}_{R,L}(y^{\mp}, \boldsymbol{x}_{\perp}) \right) \tag{2.41}$$

The color charge density which goes in the above expression is taken to be a stochastic variable which fluctuates locally and is given by the MV model as

$$\langle \rho^a_{R,L}(x^{\mp}, \boldsymbol{x}_{\perp}) \rangle = 0 \tag{2.42}$$

$$\langle \rho^a_{R,L}(x^{\mp}, \boldsymbol{x}_{\perp}) \rho^b_{R,L}(y^{\mp}, \boldsymbol{y}_{\perp}) \rangle = g^2 \mu^2 \delta^{ab} \delta(x^{\mp} - y^{\mp}) \delta^{(2)}(\boldsymbol{x}_{\perp} - \boldsymbol{y}_{\perp}) \tag{2.43}$$

So far everything looks good but Eq. (2.39), which blows up for small values of transverse momentum $\boldsymbol{k}_{\perp}$. One possible way to treat this divergence is by excluding the zero transverse momentum mode but usually it is cured by introducing an infrared regulator m in the denominator as in [18, 85]

$$A^{\pm,a}_{R,L}(x^{\mp}, \boldsymbol{x}_{\perp}) = \int \frac{d^2\boldsymbol{k}_{\perp}}{(2\pi)^2} \frac{\tilde{\rho}^a_{R,L}(x^{\mp}, \boldsymbol{x}_{\perp})}{\boldsymbol{k}_{\perp}^2 + m^2} e^{i\boldsymbol{k}_{\perp}\cdot\boldsymbol{x}_{\perp}} \tag{2.44}$$

This regulator is of the same order as of the non-perturbative scale Λ_{QCD} and numerical simulation strongly depend on it. One way to think of this infrared regulator is that it chops off the long Coulomb tails generated by the charge density of the nucleus. In simple words it is equivalent to Debye mass which sets scale for screening of the color charges. In order to keep the form of Eq. (2.38) as it is, we modify the charge density by introducing the infrared regulator as

$$\tilde{\rho}^a_{R,L}(x^{\mp}, \boldsymbol{k}_{\perp}) \rightarrow \frac{\boldsymbol{k}_{\perp}^2}{\boldsymbol{k}_{\perp}^2 + m^2} \tilde{\rho}^a_{R,L}(x^{\mp}, \boldsymbol{k}_{\perp}) \tag{2.45}$$

Since, we are working in the LC gauge, it is straightforward to see that the only

non-zero field strength tensors in Minkowski space are F^{i0} and F^{iz}. Using this we can determine the transverse electric and magnetic field of the nucleus as

$$E^i = F^{0i} = \partial^0 A^i \tag{2.46}$$

$$B^i = -\frac{1}{2}\epsilon^{ijk}F_{jk} = \epsilon^{ijz}\partial_z A_j \tag{2.47}$$

We note that the fields are orthogonal to each other and to the direction of propagation of nucleus, and only lives on the 2-dimensional sheet where the charges exist. These fields can be interpreted as the QCD analogue of the Lienard-Wiechert fields, which are the electromagnetic fields of the moving point charge.

2.3   Collision of ultra-relativistic hadrons

So far we have accustomed ourselves to the solution of single nucleus moving at the speed of light. With this information in hand, we can describe the ultra-relativistic collision as the collision of two coloured glass sheets as discussed in more details in [86]

In Fig. 2.2 the space-time diagram of the collision is shown which consists of four well-defined regions. In the backward light cone i.e region I, the solution is trivial and is given as $A^\mu = 0$. Unless the two sheets pass through each other, the resultant solution in region II and III is given in terms of the pure gauge fields of the incoming nuclei. Overall we have color charges present on the boundary of light cone with static fields behind them. Now for the region IV which is in the casual contact with the collision point, one has to solve the equations of motion with sources on the boundary of light cone. Since it is not possible to solve the Yang-Mills equation by simultaneously taking charges on the both the edges and then obtaining a single gauge transform which would result in a pure gauge solution in the forward light cone, a matter is produced which is called Glasma [86]. This is different from abelian analogue where solution in forward light cone is given as a sum of two pure gauge, and classically, no matter is produced.

Now in order to determine the gauge fields in the forward light-cone, we have to
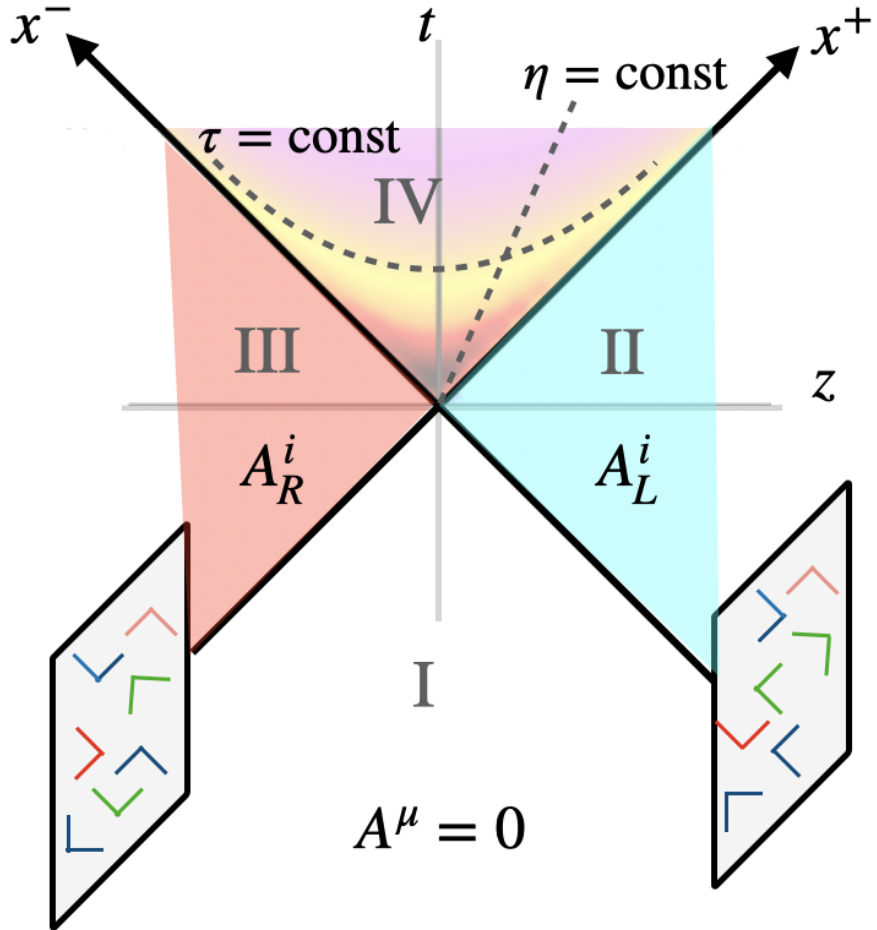
Figure 2.2: Space-time diagram for the collision of two infinitesimally thin CGC sheets moving at the speed of light, shown along with the transverse electric and magnetic field of the sheets. The solution in the region II and III is given by the pure gauge solution of the single sheets whereas the solution in the region IV is determined numerically or (semi-) analytically.

solve the source-less Yang Mill equation along with the boundary condition present at the edges of light cone. The combined color current and the solution from the region II and III is

$$J^\mu(x) = \delta^{\mu+}\delta(x^-)\rho_L(\boldsymbol{x}_\perp) + \delta^{\mu-}\delta(x^+)\rho_R(\boldsymbol{x}_\perp) \tag{2.48}$$

$$A^\pm = 0 \qquad A^i = \Theta(x^-)(-x^+)A_R^i(\boldsymbol{x}_\perp) + \Theta(x^+)(-x^-)A_L^i(\boldsymbol{x}_\perp) \tag{2.49}$$

Now since the source currents are only restricted to the boundary of the light cone, the solution in the forward light-cone ought to be boost-invariant. Hence it would be convenient to work in the $\tau - \eta$ coordinate system

$$\tau = \sqrt{2x^+x^-}, \qquad \eta = \frac{1}{2}\ln\left[\frac{x^+}{x^-}\right] \tag{2.50}$$

with gauge fields given as

$$A^\tau = \frac{1}{\tau}\left(x^+A^- + x^-A^+\right) \tag{2.51}$$

$$A^\eta = \frac{1}{\tau^2}\left(x^-A^+ - x^+A^-\right) \tag{2.52}$$

For $A^\tau = 0$ gauge, the solution in the forward light-cone can be assumed to be

$$A^i(x) = \alpha^i(\tau, \boldsymbol{x}_\perp) \tag{2.53}$$

$$A^\eta(x) = \alpha^\eta(\tau, \boldsymbol{x}_\perp) \tag{2.54}$$

which is independent of η because the incoming nuclei are infinitesimally thin. The solution at the boundary $(\tau \to 0)$ is obtained by matching the combined solution of region II and III, as given in Eq. (2.49), with the solution in forward light cone Eq. (2.53)

$$\alpha^i(\tau \to 0, \boldsymbol{x}_\perp) = A_R^i(\boldsymbol{x}_\perp) + A_L^i(\boldsymbol{x}_\perp) \tag{2.55}$$

$$\alpha^\eta(\tau \to 0, \boldsymbol{x}_\perp) = \frac{ig}{2}\left[A_R^i(\boldsymbol{x}_\perp), A_L^i(\boldsymbol{x}_\perp)\right] \tag{2.56}$$

$$\partial_\tau \alpha^{i,\eta}(\tau \to 0, \boldsymbol{x}_\perp) = 0 \tag{2.57}$$

With this initial condition, the solution for $\tau > 0$ can be obtained numerically [86].

In addition to the fields of the incoming nuclei, the above gauge fields, give rise to longitudinal electric and longitudinal magnetic fields

$$E^z(\tau \to 0, \boldsymbol{x}_\perp) = ig\delta^{ij}\Big[A_R^i(\boldsymbol{x}_\perp), A_L^j(\boldsymbol{x}_\perp)\Big] \tag{2.58}$$

$$B^z(\tau \to 0, \boldsymbol{x}_\perp) = ig\epsilon^{ij}\Big[A_R^i(\boldsymbol{x}_\perp), A_L^j(\boldsymbol{x}_\perp)\Big] \tag{2.59}$$

which are correlated over transverse distance scales on the size $\mathcal{O}(1/Q_s)$. In [28], the authors discuss the natural explanation for the occurrence of longitudinal color fields in terms of induced charge density.

We can conclude this by summarising the collision as: As the incoming nuclei with the transverse fields move away from each other after the collision, chromo-electric and chromo-magnetic field in form of elongated tubes fills up the space. At later times, these flux tubes give rise to their transverse counterpart and evolve, until all components are comparable to each other. The Glasma refers to these chromo-electric and chromo-magnetic fields which populates the initial stage of the collision.

2.4   Real-time lattice simulation

In the last section, we outlined the results for single nuclei before the collision and determined the initial condition for the Glasma fields. Over the years, different approaches have been put forward in order to obtain the gauge fields after the collision. Most of the initial approximate solutions were based on the power expansion of the valence charge [87] and thereby relied on the assumption that the classical fields are weak. Many (semi-) analytic results [32–35] hinges on the idea that the classical description breaks down very soon after the collision and hence one can solve the Yang-Mills equation in a power series in τ. Despite the rigorous mathematics, it is extremely difficult to compute higher order terms and make an agreeable comparison with the existing results. A better way to solve the classical Yang-Mills equation is to use numerical methods.

Real time lattice gauge theory is based on discretizing the classical Yang-Mills theory on space-time lattice. In this approach, we consider points (x, y, z) on a cubic lattice

of dimension $N_x \times N_y \times N_z$ with lattice spacing a_μ in μ-direction. To begin with, we will consider the time to be a continuous variable and will be discretized later. The lattice analogue of our gauge fields is given in terms of link variables $U_\mu(x)$

$$U_\mu(x) = \exp\left(iga_\mu A_\mu^a(x + a_\mu/2)t^a\right) \tag{2.60}$$

where $\mu = t, x, y, z$ is used to denote the Lorentz indices in Minkwoski coordinates, t^a are the fundamental generators of $su(N_c)$ Lie Algebra normalized as $tr[t^a, t^b] = \delta^{ab}/2$ and g is the gauge coupling. A physical picture of the link variable is that it is the smallest space-like Wilson line that one considers while connecting the two adjacent lattice sites x and $x + a_\mu$

$$U_\mu(x) = \mathcal{P}\exp\left(ig\int_x^{x+a_\mu} dx^\mu A_\mu(x)\right) \tag{2.61}$$

To enforce the gauge invariance of the action, the link variables transforms as

$$U_\mu^{(G)}(x) = G(x)U_\mu(x)G^\dagger(x + a_\mu) \tag{2.62}$$

where $G(x) \in SU(N_c)$ are local gauge transformation. Before constructing the lattice gauge action, we introduce another term called plaquette $U_{\mu\nu}(x)$ which are the smallest, closed loops on the lattice.

$$U_{\mu\nu}(x) = U_\mu(x)U_\nu(x + a_\mu)U_\mu^\dagger(x + a_\nu)U_\nu^\dagger(x) \tag{2.63}$$

where a link variable in negative direction is defined using

$$U_\mu^\dagger(x) = U_{-\mu}(x + a_\mu) \tag{2.64}$$

It can be easily seen that the trace of the plaquette is a gauge invariant object. On taking the continuum limit $a_\mu \to 0$, one finds that the plaquette is related to the field strength tensor

$$U_{\mu\nu}(x) = \exp\left(iga_\mu a_\nu F_{\mu\nu}^a(x + a_\mu/2 + a_\nu/2)t^a + \mathcal{O}(ga^3)\right) \tag{2.65}$$

Unlike the link variable which connects the adjacent lattice points, plaquette are defined in the center of the loop and relates to the flux through the enclosed area.

Since in the forthcoming discussion, we will be working in the axial gauge $A^t = 0$, the corresponding link variable are given as $U_t = \mathbb{1}$. At this stage one can express, electric field in terms of plaquette but to make quantities dimensionless on lattice, we introduce some factors while connecting the continuum electric field to its lattice counterpart

$$E^I(x) = \frac{ga^3}{a_I} E^{I,cont}(x + a_t/2 + a_I/2) \tag{2.66}$$

We note that $I, J = x, y, z$ will be used to denotes the spatial Lorentz indices.

2.4.1 Equation of Motion

The lattice analogue of the Yang-Mills equations of motion can be derived using Hamiltonian formalism. By performing the Legendre transform

$$\mathcal{H} = E_a^\mu \left(\partial_x^0 A_\mu^a \right) - \mathcal{L} \tag{2.67}$$

the Yang-Mills Hamiltonian in the continuum form takes the form

$$H = \int d^3 x \mathcal{H}, \qquad \mathcal{H} = \frac{1}{2\sqrt{-g_c}} (-g^{IJ}) E_a^{I,cont} E_a^{J,cont} + \frac{\sqrt{-g_c}}{4} F_{IJ}^a F_a^{IJ} \tag{2.68}$$

where summation is implied over α, β. Now based on the plaquette and the lattice electric field, the lattice Hamiltonian is defined as

$$H = \sum_{x,I} \frac{a_I^2}{g^2 \sqrt{-g_c} a^3} (-g^{II}) \frac{E_{a,x}^I E_{a,x}^I}{2} + \sum_{x,I,J} \frac{\sqrt{-g_c} a^3}{g^2 a_I^2 a_J^2} (-g^{II})(-g^{JJ}) \text{ReTr} \left[\mathbb{1} - U_{IJ}(x) \right] \tag{2.69}$$

where g_c is the metric determinant defined as $g_c := det(g_{\mu\nu})$.

Using the lattice Hamiltonian, the lattice equation of motion are derived from their continuum analogues via

$$\partial_{x^0} E_{a,x}^I = -\left(\frac{ga^3}{a_I} \right) \frac{\partial H}{\partial A_{I,x}^a} \tag{2.70}$$

$$\partial_{x^0} A_{I,x}^a = \left(\frac{ga^3}{a_I} \right) \frac{\partial H}{\partial E_{a,x}^I} \tag{2.71}$$

where the factors are associated with the mapping of continuum variables to lattice variables. By solving Eq. (2.71) one gets;

$$\partial_{x^0} A^a_{I,x} = \frac{a_I}{g\sqrt{-g}a^3}(-g^{II})E^I_{a,x} \tag{2.72}$$

On using the definition of gauge links, we get

$$\partial_{x^0} U_{I,x} = \sum_y a^3 \frac{\partial U_{I,x}}{\partial A^a_{I,y}}\partial_{x^0} A^a_{I,y} = (-iga_I)\left(\partial_{x^0} A^a_{I,x} t^a\right) \tag{2.73}$$

which leads to the following expression for the evolution of the lattice gauge links

$$\partial_{x^0} U_{I,x} = -i\frac{a_I^2}{\sqrt{g_c}a^3}(-g_{II})E^I_{a,x} t^a U_{I,x} \tag{2.74}$$

In order to determine the equation of motion for the electric field, we first look at the derivative of lattice Hamiltonian with respect to the gauge field

$$\frac{\partial H}{\partial A^a_{I,x}} = \left(\frac{a_I}{ga^3}\right)\sum_J \frac{\sqrt{-g_c}a^3}{a_I^2 a_J^2}(-g^{II})(-g^{JJ})\mathrm{ReTr}\left[\mathrm{it}^{\mathrm{a}}\left(\mathrm{U_{IJ}(x)} + \mathrm{U_{-JI}(x)} - \mathrm{U_{I-J}(x)} - \mathrm{U_{JI}(x)}\right)\right] \tag{2.75}$$

By using the anti symmetric properties of the field strength tensor, we can compactify the above expression by using $U_{\mu\nu} = -U_{\nu\mu}$

$$\frac{\partial H}{\partial A^a_{I,x}} = 2\left(\frac{a_I}{ga^3}\right)\sum_J \frac{\sqrt{-g_c}a^3}{a_I^2 a_J^2}(-g^{II})(-g^{JJ})\mathrm{ReTr}\left[\mathrm{it}^{\mathrm{a}}\left(\mathrm{U_{IJ}(x)} - \mathrm{U_{I-J}(x)}\right)\right] \tag{2.76}$$

Note that the above expressions are for source-less Lagrangian. The source can be introduced to the EOMs of the electric field as in the continuum as

$$\partial_{x^0} E^I_{a,x} = \left(-2\sqrt{-g_c}a^3\right)\left(\frac{-g^{II}}{a_I^2}\right)\sum_j \left(\frac{-g^{JJ}}{a_J^2}\right)\mathrm{ReTr}\left[\mathrm{it}^{\mathrm{a}}\left(\mathrm{U_{IJ}(x)} - \mathrm{U_{I-J}(x)}\right)\right] - \mathrm{j}^{\mathrm{I}}_{\mathrm{a,x}} \tag{2.77}$$

where $j^I_{a,x}$ denotes the color charge density at the lattice site.

While Eqs. (2.74) and (2.77) provide the EOMs for the gauge links and electric fields discretized on a spatial lattice, evidently, in order to solve Eqs. (2.74) and (2.77) numerically, it also becomes necessary to discretize their time evolution. For small temporal lattice spacing ($a_t \to 0$), one can solve the equations on lattice using

Leapfrog Algorithm which involves formulating the problem at integer and half-integer time steps. We purposely defined our electric fields at half-integer time step in Eq. (2.66) which leads to solving the gauge fields at full time steps.

$$U_I(x + a_t) = \exp\left(-i\frac{a_I^2 a_t}{\sqrt{g_c}a^3}(-g_{II})E^I\left(x + \frac{a_t}{2}\right)\right)U_I(x) \tag{2.78}$$

The plaquette involved in the Eq. (2.77) are solved at full time steps, such that

$$E_a^i\left(x + \frac{a_t}{2}\right) = E_a^I\left(x - \frac{a_t}{2}\right) + \left(-2\sqrt{-g_c}a^3\right)\left(\frac{-g^{II}}{a_I^2}\right) \times$$

$$\sum_J \left(\frac{-g^{JJ}}{a_J^2}\right)\mathrm{ReTr}\left[\mathrm{it}^\mathrm{a}\left(\mathrm{U_{IJ}(x)} - \mathrm{U_{I-J}(x)}\right)\right] - \mathrm{j}_{a,x}^I \tag{2.79}$$

Along with the evolution equations, we can also derive the Gauss Law constraint by writing the equation of motion for the electric field and the gauge link in term of Algebra valued fields as

$$\partial_{x^0} E_x^I = \left(-i\sqrt{-g_c}a^3\right)\left(\frac{-g^{II}}{a_I^2}\right)\sum_j \left(\frac{-g^{JJ}}{a_J^2}\right)\left[\left(U_{IJ}(x) - U_{I-J}(x)\right)\right] - j_x^I \tag{2.80}$$

and

$$\partial_{x^0}U_{I,x} = -i\frac{a_I^2}{\sqrt{g_c}a^3}(-g_{II})E_x^I U_{I,x} \qquad \partial_{x^0}U_{I,x}^\dagger = -i\frac{a_I^2}{\sqrt{g_c}a^3}(-g_{II})U_{I,x}^\dagger E_x^I \tag{2.81}$$

The covariant derivative in the Gauss constraint $D_I E^I - j^0 = 0$ can be expanded to give

$$\sum_I E_x^I - U_{I,x-I}^\dagger E_{x-I}^I U_{I,x-I} - j^0 = 0 \tag{2.82}$$

Taking the time derivative of the above equation, one gets following contribution from the derivative of gauge links

$$\partial_{x^0}U_{I,x-I}^\dagger E_{x-I}U_{I,x-I} + U_{I,x-I}^\dagger E_{x-I}\partial_{x^0}U_{I,x-I} = 0 \tag{2.83}$$

and following contribution on taking the derivative of electric field $\Big(\text{Eq. }(2.80)\Big)$ and that of current

$$\sum_{IJ} U_{IJ}(x) - U_{I-J}(x) - U_{I,x-I}^{\dagger}\Big(U_{IJ}(x-I) - U_{I-J}(x-I)\Big)U_{I,x-I} - D_I j^I - \partial_{x^0} j^0$$

$$(2.84)$$

The first two terms vanishes and the last two term yields current conservation equation. Therefore, the evolution equation for the Gauss law is also satisfied i.e

$$\partial_{x^0}\Big(D_I(x)E_x^I - j_x^0\Big) = 0 \tag{2.85}$$

As can be seen from the above equation that the conservation of Gauss law depends on the evolution of fields and currents. For relevant initial condition, the Gauss law constraint has to be satisfied but evolution on the lattice involves various discretization errors which leads to a small violation.

2.4.2 Initial Condition

In order to obtain the solution of boost-invariant Glasma in the forward light cone, one has to recast the initial conditions on the lattice in terms of lattice variable i.e transverse gauge links U_i and longitudinal electric fields E^{η}.

As the transverse gauge links on the boundary of light cone are given as the sum of pure gauge solution of the incoming nuclei, we will start by putting one nucleus on lattice. We start by sampling the color charge density ρ_k in the transverse plane according to

$$\Big\langle \rho_k^a(x,y)\rho_l^b(\bar{x},\bar{y})\Big\rangle = \delta^{ab}\delta^{kl}\delta(x-\bar{x})\delta(y-\bar{y})\frac{g^2\mu^2(x,y)}{N_s a_x a_y} \tag{2.86}$$

where the indices $k,l = 1,2,...,N_s$ represents discretized sheets along x^- or x^+ coordinate. With this, the color charge density at each lattice site is given as

$$\rho_{L/R}^a(x,y) = \sum_{k_x,k_y} e^{2\pi i\left(\frac{k_x x}{N_x} + \frac{k_y y}{N_y}\right)} \frac{\boldsymbol{k}_\perp^2}{\boldsymbol{k}_\perp^2 + m^2} \sum_{x',y'} \frac{g\mu(x,y)}{\sqrt{N_s a_x a_y}} \zeta^a(x',y') e^{-2\pi i\left(\frac{k_x x'}{N_x} + \frac{k_y y'}{N_y}\right)}$$

$$(2.87)$$

We have regularised the color charge density by introducing the infrared regulator as mentioned in Eq. (2.45). On top of infrared regularisation, one could also introduce a cut-off scale Λ to make the problem UV finite. Here, $\zeta(x, y)$ are Gaussian random numbers and on a lattice of size $N_x \times N_y$. Usually one takes a square lattice such that $N_x = N_y$, along with equidistant transverse lattice spacing.

The above equation includes back and forth, discrete Fourier transformation which are quite easy to implement on a lattice. k_x, k_y are discretized momentum with squared lattice momentum given as

$$\boldsymbol{k}_\perp^2 = \frac{4}{a_x^2} \sin^2\left(\frac{\pi k_x}{N_x}\right) + \frac{4}{a_y^2} \sin^2\left(\frac{\pi k_y}{N_y}\right) \tag{2.88}$$

The Wilson line at each lattice site is then fabricated as

$$V_{L/R}(x, y) = \prod_{i=1}^{N_s} \exp\left(-ig\frac{\rho_{L/R}^a(x, y)t^a}{\nabla^2}\right) \tag{2.89}$$

With this, the gauge links in Region II and III of Fig. 2.2 is obtained from the Wilson line using a fairly simple relation

$$U_{i,\,L/R}(\boldsymbol{x}_\perp) = V_{L/R}(\boldsymbol{x}_\perp)V_{L/R}^\dagger(\boldsymbol{x}_\perp + a_i) \tag{2.90}$$

The lattice equivalent of Eq. (2.55) which is the solution of gauge links at the boundary of the light-cone, has been derived in [88] and is given as

$$\mathrm{Tr}\left[t_a\left(\left(\mathbb{1} + U_i\right)\left(U_{i,L}^\dagger + U_{i,R}^\dagger\right)\right)\right] = 0 \tag{2.91}$$

This simple looking equation is highly non-trivial to solve as it involves $N_c^2 - 1$ equations. For $SU(2)$ group, the solution can be compactly expressed as

$$U_i(\boldsymbol{x}_\perp) = \left(U_{i,L} + U_{i,R}\right)\left(U_{i,L}^\dagger + U_{i,R}^\dagger\right)^{-1} \tag{2.92}$$

For $N_c > 2$, the technique is outlined in [83] and an iterative solution is available in

[89]. The initial electric field on lattice has also been derived in [88] and takes the form

$$E^\eta(\boldsymbol{x}_\perp) = \frac{-i}{4g} \sum_{i=1,2} \frac{1}{a_i^2} \Big[\Big(U_i(\boldsymbol{x}_\perp) - 1\Big)\Big(U_{i,L}^\dagger(\boldsymbol{x}_\perp) - U_{i,R}^\dagger(\boldsymbol{x}_\perp)\Big)$$
$$+ \Big(U_i(\boldsymbol{x}_\perp - a_\perp) - 1\Big)\Big(U_{i,L}^\dagger(\boldsymbol{x}_\perp - a_\perp) - U_{i,R}^\dagger(\boldsymbol{x}_\perp - a_\perp)\Big) - h.c. \Big] \quad (2.93)$$

where "h.c" stands for hermitian conjugate of the spelled out term. One can easily check that on expanding the gauge links to first order, the above expression matches with the continuum result (2.58). These initial conditions are then fed into the leapfrog algorithm to obtain the solution at desired proper time τ.

2.5 Attributes of Boost-invariant Glasma

Over the years, series of work has been done in unfolding the transverse geometry of fireball. In this section, we will put together the standard results obtained via numerical simulation of $2 + 1$D Glasma. Our main concern will be the different components of energy momentum tensor $T^{\mu\nu}$

$$T^{\mu\nu} = \text{Tr}\Big[-F^{\mu\rho}F^\nu{}_\rho + \frac{1}{4}g^{\mu\nu}F^{\rho\sigma}F_{\rho\sigma} \Big] \quad (2.94)$$

Since MV model is transversely homogeneous, only diagonal components of the energy momentum tensor survives on averaging over the color charges densities, which are given as

$$T^{\mu\nu} = \text{diag}\Big(\varepsilon, p_T, p_T, p_L\Big) \quad (2.95)$$

where $\varepsilon = \frac{1}{\tau}\frac{dE}{d^2\mathbf{x}_\perp d\eta}$ is the energy density, p_T is the transverse pressure and p_L is the longitudinal pressure. Since classical Yang-Mills theory is a conformal field theory, the energy momentum tensor is traceless, and the energy density ε is connected to the longitudinal and transverse pressure as $\varepsilon = 2p_T + p_L$. These pressure components
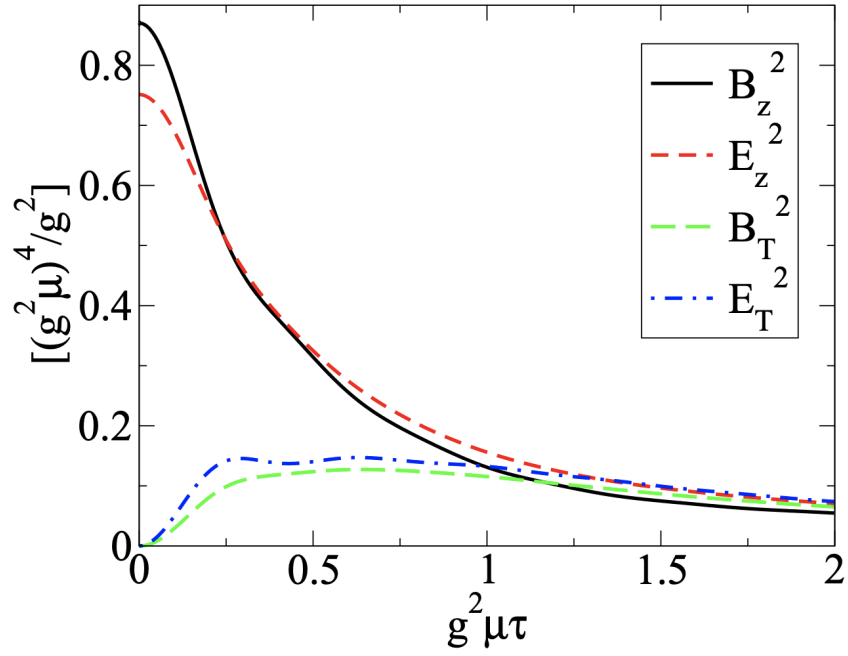
Figure 2.3: Longitudinal and transverse components of the electric and magnetic field computed on 512×512 lattice with $g^2 \mu R_A = 67.7$. This result is taken from ref. [90]

can be expressed in terms of transverse and longitudinal components of electric and magnetic fields as

$$p_T = E_L^2 + B_L^2 \tag{2.96}$$

$$p_L = E_T^2 + B_T^2 - E_L^2 - B_L^2 \tag{2.97}$$

In the proper-time rapidity (τ, η) coordinates, these components are given as

$$E_T^2 = \left\langle \text{Tr}\left[F_{\tau i} F_{\tau i}\right] \right\rangle \tag{2.98}$$

$$B_L^2 = \left\langle \frac{1}{2} \text{Tr}\left[F_{ij} F_{ij}\right] \right\rangle \tag{2.99}$$

$$B_T^2 = \left\langle \frac{1}{\tau^2} \text{Tr}\left[F_{i\eta} F_{i\eta}\right] \right\rangle \tag{2.100}$$

$$E_L^2 = \left\langle \frac{1}{\tau^2} \text{Tr}\left[F_{\tau\eta} F_{\tau\eta}\right] \right\rangle \tag{2.101}$$

where $\langle \rangle$ represents averaging over the transverse plane.

The different components of the electric and magnetic fields are shown in Fig. 2.3 where numerical simulation was performed on a lattice with $N_x = N_y = 512$ in [90].

The color charge distribution was based on MV model where a dimensionless parameter $g^2\mu R_A$ controls the weak or strong-field limit. This dimensionless combination takes into account the coupling constant g, the MV parameter μ which is related to the saturation momentum, and the nuclear radius R_A. We start with $\tau \to 0$ where only longitudinal color fields exists and are expected to be as equal as given by Eqs. (2.58) and (2.59). The discrepancy in the results in Fig. 2.3 is explained in term of the breaking of rotational invariance by modes near the Brillouin zones [90].

The initial coherent longitudinal fields leads to an interesting consequence - the longitudinal pressure $p_L(\tau \to 0)$ is negative. The energy momentum tensor at early times,

$$T^{\mu\nu}(\tau = 0) = \mathrm{diag}(\varepsilon, \varepsilon, \varepsilon, -\varepsilon) \qquad (2.102)$$

reflects that we start with an anisotropic system. Subsequently, at $\tau > 0$, the fields loose their coherence and decay into quasi-particles with transverse momentum $\sim Q_s$ but vanishing longitudinal momentum in the local rest-frame. Therefore, at late times $\tau \geq 1/g^2\mu$ particles with zero longitudinal momentum lead to vanishing longitudinal pressure $p_L = 0$.

$$T^{\mu\nu}(\tau \geq 1/g^2\mu) = \mathrm{diag}(\varepsilon, \varepsilon/2, \varepsilon/2, 0) \qquad (2.103)$$

As the macroscopic properties of initial state $(T^{\mu\nu}, J^\mu)$ are set as an input for hydrodynamic model, this anisotropy could turn out to be a serious problem. One could think, if this anisotropic behaviour has something to do with the boost-invariant solution. Hence in order to study the isotropization of system at mid rapidity, small fluctuation was considered on top of boost-invariant Glasma [91–94], and these lead to the conclusion that 2+1D Glasma is unstable and rapidity dependent fluctuation drives the system towards isotropization. A more lucid treatment of this problem is by introducing an intermediate kinetic theory [95, 96] that connects the anisotropic system of classical fields to a fully isotropic hydrodynamics system.

As Glasma expands behind the outgoing nuclei the energy density decreases with time $\varepsilon \sim 1/\tau$ (Fig. 2.3) but since we are working in the boost-invariant limit, energy
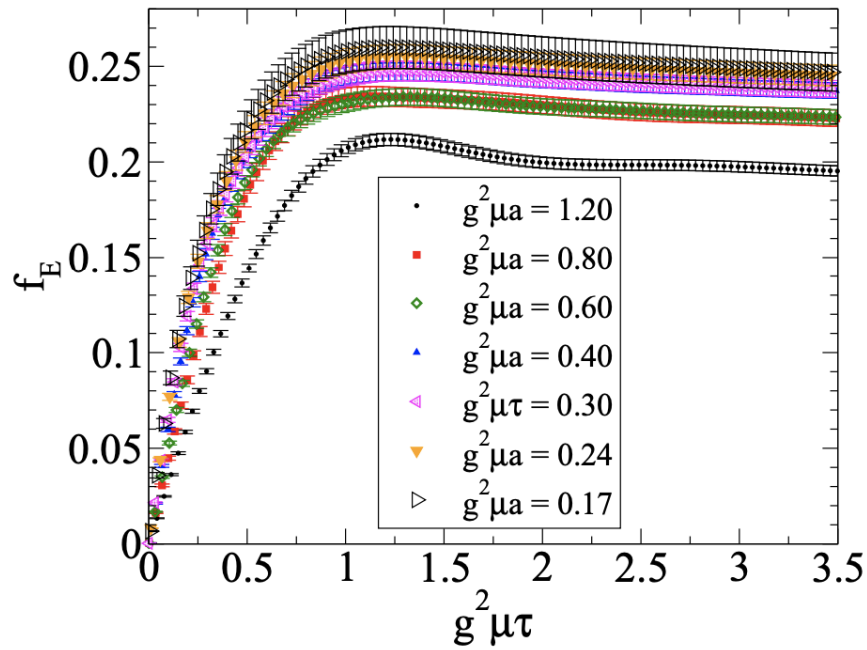
Figure 2.4: Energy per unit rapidity $f_E = \frac{g^2}{\pi R_A^2 (g^2\mu)^3} \frac{dE}{d\eta}$ as a function of proper time for different lattice spacing a. This plot is taken from ref [90]

per unit rapidity $dE/d\eta$ remains constant as shown in Fig. 2.4. In both perturbative solutions and numerical simulations [86, 90, 97] based on MV model, the energy density is found to be UV divergent at $\tau = 0$. However this logarithmic divergence dies out at late proper times ($\tau \sim 1/g^2\mu$) and hence one can regulate this behaviour in the continuum limit ($a \to 0$) for any $\tau > 0$ by introducing an ultraviolet cutoff $\Lambda \geq Q_s \propto g^2\mu$.

The Glasma expansion ceases the non-linear interaction and by the time $\tau \sim 1/Q_s$, the fields can be be treated as an ensemble of particles [28, 98, 99]. To compute the gluon distribution, one solves the linearized, source-free Yang-Mills equation in the forward light cone using the initial condition (2.55) – (2.57). Since gluon number is not a gauge invariant quantity, its computation requires the fixation of a residual gauge freedom. The standard technique is to use a Coulomb gauge $\partial_i A^i(\tau, \boldsymbol{x}_\perp) = 0$ on top of the global axial gauge $A^\tau = 0$ [98–101], at the time of measurement as it minimises the initial gauge fields. In [98, 99], the number distribution of produced gluon was computed by identifying the Hamiltonian of linearized Yang-Mills system with that of free field. In [66, 102], the gluon distribution at a particular time

τ is obtained by projecting the gauge fixed equal time correlation functions on to transversely polarized gluon modes

$$\frac{dN}{d^2\boldsymbol{k}_\perp dy} = \frac{1}{(2\pi)^2} \sum_{\lambda,a} \left| \tau g^{\mu\nu} \left(\xi_\mu^{\lambda,\boldsymbol{k}_\perp}(\tau) \partial_\tau A_\nu^a(\tau, \boldsymbol{k}_\perp) \right) \right|^2 \tag{2.104}$$

where $g^{\mu\nu}(1, -1, -1, -\tau^{-2})$ denotes the Bjorken metric and $\lambda = 1, 2$ labels the two transverse polarizations. The mode function takes the following form in the Coulomb gauge [102]

$$\xi_\mu^{(1),\boldsymbol{k}_\perp}(\tau) = \frac{\sqrt{\pi}}{2|\boldsymbol{k}_\perp|} \begin{pmatrix} -k_y \\ kx \\ 0 \end{pmatrix} H_0^{(2)}(|\boldsymbol{k}_\perp|\tau) \tag{2.105}$$

$$\xi_\mu^{(2),\boldsymbol{k}_\perp}(\tau) = \frac{\sqrt{\pi}}{2|\boldsymbol{k}_\perp|} \begin{pmatrix} 0 \\ 0 \\ \boldsymbol{k}_\perp \tau \end{pmatrix} H_1^{(2)}(|\boldsymbol{k}_\perp|\tau) \tag{2.106}$$

where $\boldsymbol{k}_\perp = (k_x, k_y)$ and $H_p^{(2)}$ denotes the Hankel functions of the section type and order p. On relating the final multiplicity of hadrons to initial gluon multiplicity, a ballpark value was obtained for number of inelastic gluon production and bounds were set for charge density parameter $g^2\mu$ at RHIC and LHC energies [103].

2.6 Renormalization equation & beyond the boost-invariance

So far the separation of the partonic content of a nucleus into large x sources and small x fields has been done arbitrarily by introducing a cutoff scale $\Lambda^+ = xP^+$ as shown in Fig. 2.5. The cutoff lead to the formation of MV model which we used to develop the initial conditions for the boost-invariant collision. One might wonder what happens if we lower the cutoff to Λ'^+. In order for the classical description to hold, the semi-fast modes with $\Lambda'^+ < k^+ < \Lambda^+$, have to be treated as the new color sources $\delta\rho$ that will radiate the small-x gluons. That means lowering the cutoff will induce color sources $\delta\rho$ such that the total sources $\rho' = \rho + \delta\rho$, will lead to a new
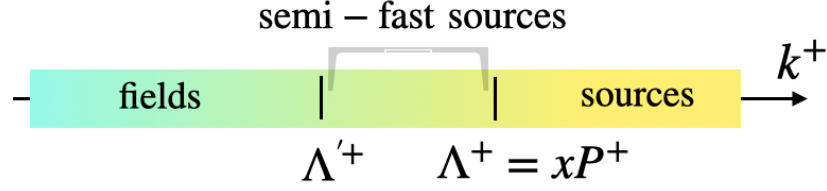
Figure 2.5: A sketch showing the separation of scales based on CGC for a hadron with longitudinal momentum P^+ along with a new cutoff $\Lambda'^+ < \Lambda^+$

distribution function $W_{\Lambda'^+}[\rho']$, similar to Eq. (2.32) but with additional quantum fluctuations that are integrated out in charged squared fluctuation μ^2. Therefore the quantum evolution to smaller x precisely results in the renormalization group equation, known as the JIMWLK evolution equation (eponymous for the authors Jalilian-Marian, Iancu, McLerran, Weigert, Leonidov and Kovner) [104]. The JIMWLK equation can be compactly written as [105–107]

$$\frac{\partial W_Y[\alpha]}{\partial Y} = -\mathcal{H}_{\text{JIMWLK}} W_Y[\alpha] \tag{2.107}$$

where W_Y denotes the weight function at rapidity Y, α is the gauge field for a given color charge density and $\mathcal{H}_{\text{JIMWLK}}$ is JIMWLK Hamiltonian given as

$$\mathcal{H}_{\text{JIMWLK}} = -\frac{1}{2} \int_{\boldsymbol{x}_\perp \boldsymbol{y}_\perp} \frac{\delta}{\delta \alpha^a(\boldsymbol{x}_\perp)} \chi^{ab}(\boldsymbol{x}_\perp, \boldsymbol{y}_\perp) \frac{\delta}{\delta \alpha^b(\boldsymbol{y}_\perp)} \tag{2.108}$$

where $\int_{\boldsymbol{x}_\perp \boldsymbol{y}_\perp}$ denotes the integration over the transverse coordinates $\boldsymbol{x}_\perp$ and $\boldsymbol{y}_\perp$. The kernel $\chi^{ab}(\boldsymbol{x}_\perp, \boldsymbol{y}_\perp)$ is related to the two point function of induced charge correlator as $\chi^{ab} \propto \langle \delta \rho_a(\boldsymbol{x}_\perp) \delta \rho_b(\boldsymbol{y}_\perp) \rangle$

For the purpose of numerical implementation, it is useful to express the JIMWLK equation as a functional Langevin equation for the Wilson lines V [106, 108]. The JIMWLK equation in term of Langevin step has been derived in [109] as

$$V_{\boldsymbol{x}_\perp}(Y + dY) = \exp\left\{ -i \frac{\sqrt{\alpha_s dY}}{\pi} \int_{\boldsymbol{z}_\perp} K_{\boldsymbol{x}_\perp - \boldsymbol{z}_\perp} \cdot \left(V_{\boldsymbol{z}_\perp} \xi_{\boldsymbol{z}_\perp} V_{\boldsymbol{z}_\perp}^\dagger \right) \right\} \times$$
$$V_{\boldsymbol{x}_\perp}(Y) \exp\left\{ i \frac{\sqrt{\alpha_s dY}}{\pi} \int_{\boldsymbol{z}_\perp} K_{\boldsymbol{x}_\perp - \boldsymbol{z}_\perp} \cdot \xi_{\boldsymbol{z}_\perp} \right\} \tag{2.109}$$

where $\alpha_s = g^2/4\pi$ is the coupling constant $\xi_{\boldsymbol{z}_\perp} = \left(\xi^a_{\boldsymbol{z}_\perp, 1} t^a, \xi^a_{\boldsymbol{z}_\perp, 2} t^a \right)$ is the noise term

which is related to the emission of semi-fast gluon by the hard partons. One and two-point function of the noise term is given as

$$\langle \xi^a_{\boldsymbol{x}_\perp,i}(Y) \rangle = 0 \tag{2.110}$$

$$\langle \xi^a_{\boldsymbol{x}_\perp,i}(Y)\xi^b_{\boldsymbol{y}_\perp,j}(Y') \rangle = \delta^{ab}\delta^{ij}\delta^{(2)}_{\boldsymbol{x}_\perp \boldsymbol{y}_\perp}\delta(Y - Y') \tag{2.111}$$

where i and j are the transverse components of the vector $\boldsymbol{x}_\perp$ and $\boldsymbol{y}_\perp$. Perturbatively, the JIMWLK kernel is given as

$$K_{\boldsymbol{x}_\perp - \boldsymbol{z}_\perp} = \frac{(\boldsymbol{x}_\perp - \boldsymbol{z}_\perp)}{(\boldsymbol{x}_\perp - \boldsymbol{z}_\perp)^2} \tag{2.112}$$

In transverse space this kernel leads to gluon emission at large transverse distances which is unphysical (due to confinement) and violates the Froissart bound of cross section. To curb this behavior, one frequently introduces the infrared regulator m [110]

$$K_{\boldsymbol{x}_\perp - \boldsymbol{z}_\perp} = m|\boldsymbol{x}_\perp - \boldsymbol{z}_\perp|K_1(m|\boldsymbol{x}_\perp - \boldsymbol{z}_\perp|)\frac{(\boldsymbol{x}_\perp - \boldsymbol{z}_\perp)}{(\boldsymbol{x}_\perp - \boldsymbol{z}_\perp)^2} \tag{2.113}$$

where $K_1(x)$ is the modified Bessel function of the second kind. Overall, the JIM-WLK evolution contains two parameters: α_s which controls the evolution speed, and m which mimics the confinement.

Basically, the evolution to small x can be formulated in rapidity. Taking this rapidity dependence into account, various simulation techniques [41, 42] have been developed to study the collisions beyond the boost-invariance by evolving the initial Wilson line V_{Y_0} via JIMWLK equation

$$V_{Y_0} \xrightarrow{JIMWLK} V_{Y_0 \pm dY} \tag{2.114}$$

In [41], Wilson lines at different rapidity collides with one another using the boost-invariant initial condition in order to obtain the 3+1 D Glasma at late times. Although, this work sets a premise for interesting phenomenology, one still needs to explore the initial state from the first principles. With this, we will now try to work on our first goal of solving the 3+1D classical Yang-Mills equation by taking the finite longitudinal thickness of the incoming nuclei into account.

Chapter 3

3D Structure of Glasma Initial State

Following chapter deals with simulation of 3+1 D Glasma on lattice. In section 3.1 we mention the general formalism to discretize 3+1 D classical Yang-Mills equation on lattice along with the initialization of gauge fields and currents. In section 3.2 we present result from our numerical simulations for MV model and explore the longitudinal dynamics of the fireball in addition to simultaneous comparison to boost-invariant results. We develop a realistic model for heavy-ion collision in Section 3.3 which we then use to study the effects of fluctuation at RHIC energies.

3.1   General formalism for $3+1$ D collisions in Yang-Mills theory

Based on the Color Glass Condensate (CGC) effective description of high-energy QCD, the initial state energy deposition and early time dynamics in high-energy heavy-ion collisions can be described semi-classically by solving classical Yang-Mills equations of motion for the gluon fields A^μ in the presence of fluctuating color charges ρ, which characterize the nuclear parton content. Even though a complete analytical treatment of the Yang-Mills equation is not possible, it is remarkable that the initial state immediately after the collision ($\tau = 0^+$) can be determined analytically for boost-invariant collisions in the high-energy limit [28, 87]. Beyond the time of the collision $\tau = 0$, where a far-from-equilibrium Glasma is produced [88, 111], the

classical Yang-Mills dynamics becomes highly non-linear, and additional analytic insights can only be obtained in the limit where one or both of the two sources are considered to be weak such that the equations of motion linearize.

Nevertheless, important insights into the early time non-equilibrium dynamics have been established based on numerical simulations [18, 92, 93, 99], where in order to describe the non-linear dynamics of the boost invariant Glasma, the effectively 2+1 dimensional classical Yang-Mills equations are discretized on a lattice and solved numerically in the forward light cone i.e. for $\tau > 0$. Below we explain how to generalize this setup to simulate the collision of nuclei with a finite longitudinal thickness in 3+1D collisions, where in contrast to the boost invariant high-energy limit, the entire space-time dynamics of the collision has to be simulated numerically, including the explicit evolution of color charges before, during and after the collision.

Due to the computational complexity of $3 + 1$ D simulations, we will perform all of our simulations for the $SU(2)$ gauge group rather than the physical gauge group $SU(3)$ of QCD. Even though we do not expect to see any qualitative changes between the $SU(2)$ and $SU(3)$ dynamics, quantitative values of observables will change, and should therefore not be compared directly to experimental results.

3.1.1   Discretization of gauge fields and currents

We follow standard procedure in the context of classical-statistical lattice gauge theory simulations [86, 112] and start by discretizing the classical Yang-Mills Hamiltonian in temporal axial $A^t = 0$ gauge on a three dimensional $N_x \times N_y \times N_z$ lattice with lattice spacing a_μ in the $\hat{\mu}$ direction [88, 99]

$$H_{YM} = \sum_{x,I,J} \frac{\sqrt{-g}a^3}{g^2 a_I^2 a_J^2}(-g_{II})(-g_{JJ})\mathrm{ReTr}\Big[1 - U_{IJ}(x)\Big] + \sum_{x,I} \frac{a_I^2}{g^2\sqrt{-g}a^3}(-g_{II})\frac{E_{a,x}^I E_{a,x}^I}{2}$$

(3.1)

where x denotes the lattice site, $a = 1 \cdots N_c^2 - 1$ is the color index and $g_{\mu\nu} = (+1, -1, -1, -1)$ denotes the Minkowski metric. In order to have consistent index notation from here after: We will use $I, J = x, y, z$ to denote the spatial Lorentz indices, $i, j = x, y$ to denote the transverse Lorentz indices, and α, β, μ, ν to denote the

four dimensional Lorentz indices in Minkowski $(t, \mathbf{x}_\perp, z)$ or light-cone $(x^+, x^-, \mathbf{x}_\perp)$ co-ordinates, with $\mathbf{x}_\perp = (x, y)$ denoting the transverse coordinates. Within the Hamiltonian formalism Eq. (3.1), the electric field strength is represented in terms of the lattice electric field variables,

$$E^I_{a,x} = \frac{ga^3}{a_I}\sqrt{-g}(-g^{IJ})\partial_0 A_{a,J}(x + \hat{I}/2 + \hat{t}/2) \tag{3.2}$$

while the magnetic field strength is given in terms of the lattice plaquette variables

$$U_{x,IJ} = U_{x,I}U_{x+\hat{I},J}U^\dagger_{x+\hat{J},I}U^\dagger_{x,J}$$
$$\simeq \exp\left(iga_I a_J F_{IJ}(x + \hat{I}/2 + \hat{J}/2)\right) \tag{3.3}$$

which are formed of SU(N_c) group valued lattice gauge links

$$U_{x,I} \simeq \exp\left(iga_I A^I(x + \hat{I}/2)\right). \tag{3.4}$$

The pre-factors in the definitions in Eqns. 3.2, 3.3 have been arranged such that all lattice variables are explicitly dimensionless. Within the CGC framework the incoming nuclei are described by eikonal color currents $J^\mu_{R/L}(x)$ which propagate along the light cones and provide a source

$$J^\mu(x) = J^\mu_R(x) + J^\mu_L(x) \tag{3.5}$$

for the classical gluon fields, where the subscripts R and L represent the nuclei coming in from the right and left respectively. Before the collision the initial conditions for the currents $J^\mu_{R/L}(x)$ in covariant $(\partial_\mu A^\mu = 0)$ gauge are given in terms of the color charge densities $\rho^a_{R/L}(x^\pm, \mathbf{x}_\perp)$ of the two colliding nuclei as

$$J^\mu_R(x) = \delta^{\mu-}\rho^a_R(x^+, \mathbf{x}_\perp)t^a$$
$$J^\mu_L(x) = \delta^{\mu+}\rho^a_L(x^-, \mathbf{x}_\perp)t^a \tag{3.6}$$

where t^a are generators in the fundamental representation. However, during the collision both currents $J^\mu_{R/L}(x)$ will receive a color-rotation, which in the 3+1 D setup has to be calculated by solving dynamical equations of motions for the currents

$J^\mu_{R/L}(x)$. We therefore also discretize the color currents on the lattice, where by keeping track of the relevant light-cone ($\pm$) components, the currents are defined as

$$
\begin{aligned}
J^\pm_{x,dyn}(t) &= \quad ga^3 \frac{J^0_{R/L}(x+\hat{z}/2)\pm J^z_{R/L}(x+\hat{z}/2)}{\sqrt{2}} \\
J^\pm_{x,stat}(t+\frac{a_t}{2}) &= \quad ga^3 \frac{J^0_{R/L}(x+\hat{t}/2)\pm J^z_{R/L}(x+\hat{t}/2)}{\sqrt{2}}
\end{aligned}
\tag{3.7}
$$

with "dynamical" (dyn) and "static" (stat) currents on alternating half-integer time slices, as usual in a leap-frog scheme.

3.1.2 Equations of Motion & Gauss Law

By performing the variation of the lattice Hamiltonian w.r.t to electric fields and gauge fields, one obtains the Hamiltonian equations of motion for the lattice gauge link and electric field variables. We employ a leap frog algorithm with time step $a_t = 0.08 \times min(a_z, a_\perp)$, where gauge links are defined at every full time step whereas the electric fields are calculated for every half-integer time step, such that the update rule for the lattice gauge links takes the form

$$
U_{I,x}(t+a_t) = \exp\left(-i\frac{a_I^2 a_t}{\sqrt{-g}a^3}(-g_{II})E_{I,x}(t+\frac{a_t}{2})\right)U_{I,x}(t)
\tag{3.8}
$$

whereas for the evolution of the lattice electric fields one also has to take into account the coupling to the eikonal currents, such that the update rule for the lattice electric fields is given by

$$
E^i_{a,x}(t+a_t/2) - E^i_{a,x}(t-a_t/2) = (-2\sqrt{-g}a^3 a_t)\left(\frac{-g_{ii}}{a_i^2}\right)\sum_j\left(\frac{-g_{jj}}{a_j^2}\right)\times
$$
$$
\text{ReTr}\left[it^a\left(U_{ij}(x)-U_{i-j}(x)\right)\right]
\tag{3.9}
$$

$$
E^z_{a,x}(t+a_t/2) - E^z_{a,x}(t-a_t/2) = (-2\sqrt{-g}a^3 a_t)\left(\frac{-g_{zz}}{a_z^2}\right)\sum_i\left(\frac{-g_{ii}}{a_i^2}\right)\times
$$
$$
\text{ReTr}\left[it^a\left(U_{zi}(x)-U_{z-i}(x)\right)\right] - a_t\frac{J^+_{a,x,dyn}(t)-J^-_{a,x,dyn}(t)}{\sqrt{2}a_z}
$$
$$
\tag{3.10}
$$

Due to the explicit appearance of the currents on the rhs of Eq. 3.10, the color currents $J_x^\pm(t)$ also have to be treated as dynamical degree of freedom as – in contrast to the boost-invariant high-energy limit – they are present not only on the infinitesimal boundary of the light-cone but throughout the entire simulation volume and thus affect the evolution of the classical Yang-Mills fields. Since in the eikonal limit the different components of the current are related by $J_{R/L}^0(x) = \mp J_{R/L}^z(x)$, it is straightforward to construct the dynamical equation of motion of the currents from the (covariant) charge conservation equation $D_\mu J^\mu = 0$ as $\partial_0 J^\pm(x) = \mp D_z J^\pm(x)$, and we employ the following update rules

$$J_{x,dyn}^\pm(t + a_t) - J_{x,dyn}^\pm(t) = \mp a_t D_z^F J_{x,stat}^\pm(t + \frac{a_t}{2})$$

$$J_{x,stat}^\pm(t + \frac{a_t}{2}) - J_{x,stat}^\pm(t - \frac{a_t}{2}) = \mp a_t D_{x,z}^B J_{x,dyn}^\pm(t) \tag{3.11}$$

where $D_\mu^{F/B}$ denotes the forward and backward covariant derivatives

$$D_{x,\mu}^F X = \left(U_{x,\mu} X_{(x+i),\mu} U_{x,\mu}^\dagger - X_{x,\mu} \right)/a_\mu$$

$$D_{x,\mu}^B X = \left(X_{x,\mu} - U_{(x-i),\mu}^\dagger X_{(x-i),\mu} \, U_{(x-i),\mu} \right)/a_\mu \tag{3.12}$$

We note that due to the leap-frog discretization in Eqns. 3.11, the dynamical currents do not propagate exactly at the speed of light, but instead satisfy the same lattice dispersion relation as the lattice gauge fields, which converges to a light-like dispersion in the continuum limit. This is different from CPIC method where the color charges have light-like dispersion and the dispersion of the gauge field depends upon the details of the numerical scheme [113]. However, as in CPIC, the lattice version of the Gauss law constraint

$$D_{x,I}^B E_x^I(t + \frac{a_t}{2}) = \frac{1}{\sqrt{2}} \left(J_{stat}^+(t + \frac{a_t}{2}) + J_{stat}^-(t + \frac{a_t}{2}) \right) \tag{3.13}$$

is automatically satisfied at each time, as long as it is satisfied by the initial conditions, as can be checked straightforwardly by evaluating the time derivative of Eq. 3.13

$$\partial_0\Big(D_{x,I}E_x^I - J^0\Big) = \partial_0\Big(E_{x,I} - U^\dagger_{(x-I),I}E^I_{(x-I)}\ U_{(x-I),I} - J^0\Big)$$
$$= D_I\Big(-J^I - \mathrm{ReTr}\Big[it^a\Big(U_{ij}(x) - U_{i-j}(x)\Big)\Big]\Big) - \partial_0 J^0$$
$$= -D_\mu J^\mu = 0 \tag{3.14}$$

where the second equality comes from the equation of motion of gauge links and fields as in Eqs. 3.8,-3.10. The gauge part vanishes which then leaves us with current continuity equation as seen in the third equality.

3.1.3 Initial Conditions for 3+1D collisions

Since for 3+1 D collisions of extended nuclei, one has to simulate the dynamics of the color charges before, during and after the collision, the initial conditions for the above evolution equations have be formulated at Minkowski time $t_0 < 0$ before the collision, where the colliding nuclei are well separated from each other. Since the color charges inside the two nuclei do not interact with each other before the wave-packets overlap, the initial conditions are then determined by the superposition of the analytic solutions for the gauge fields in the presence of the individual color charges of the two nuclei, as illustrated in Fig. 3.1.

Specifically, in the covariant $\partial_\mu A^\mu = 0$ gauge, the solution to classical Yang-Mills equations before the collision takes the form

$$A^\pm_{cov.}(x^\mp, \boldsymbol{x}_\perp) = -\frac{1}{\nabla_\perp^2}\rho_{\mathrm{L,R}}(x^\mp, \boldsymbol{x}_\perp) \qquad A^i_{cov.} = 0 \tag{3.15}$$

where we have explicitly assumed that – at the initial time $t < 0$– the incoming nuclei are well separated from each other, such that color charge distributions $\rho_{\mathrm{L,R}}(x^\mp, \boldsymbol{x}_\perp)$ of the two nuclei do not interact with each other.

We note that in $\partial_\mu A^\mu = 0$ gauge the gauge potentials $A^\pm$, only have support in the vicinity of the two light-cones, where color charges are present, as seen in top panel of Fig. 3.1. However, for real time lattice simulation it is convenient to employ the
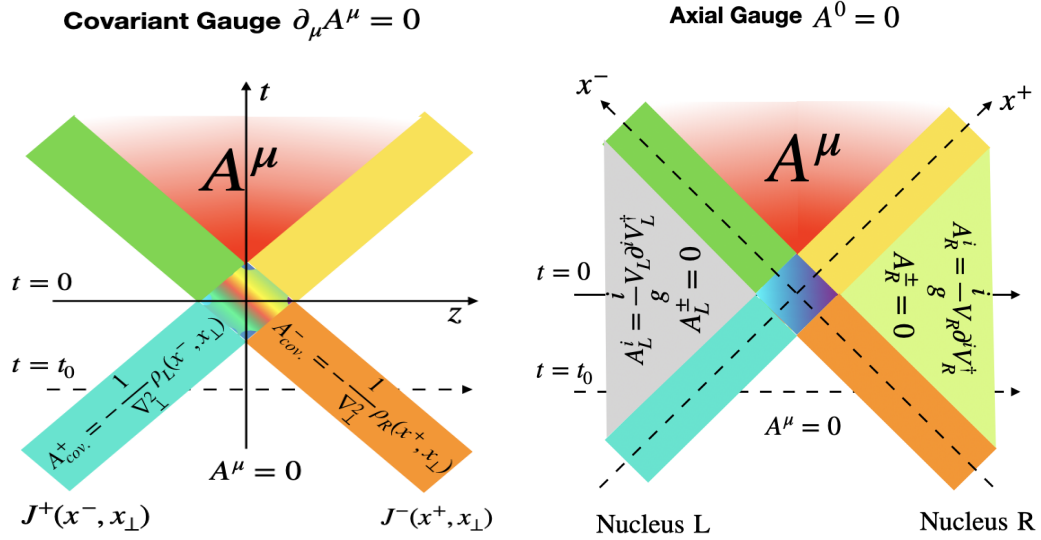
Figure 3.1: Gauge fields for the two colliding nuclei with finite longitudinal extent $(R_\gamma \simeq \frac{R}{\gamma})$ in covariant gauge (left) and light-cone or temporal axial gauge (right).

temporal axial ($A^0 = 0$) gauge condition, and the corresponding initial conditions can be obtained by performing a gauge transformation, which eliminates the gauge potentials $A^\pm$ prior to the collision. By following previous works [85, 114, 115], the corresponding gauge transformation can be expressed as

$$V(x) = V_R(x^+, \boldsymbol{x}_\perp) V_L(x^-, \boldsymbol{x}_\perp) \tag{3.16}$$

where the light-like Wilson lines $V_{L/R}$ associated with the left and right moving nuclei are determined by

$$\begin{aligned}
\partial_+ V_R(x^+, \boldsymbol{x}_\perp) &= ig A_{cov.}^- V_R(x^+, \boldsymbol{x}_\perp), \\
\partial_- V_L(x^-, \boldsymbol{x}_\perp) &= ig A_{cov.}^+ V_L(x^-, \boldsymbol{x}_\perp)
\end{aligned} \tag{3.17}$$

such that $V_{L/R}$ are given by the light-like Wilson lines

$$\begin{aligned}
V_R(x^+, \boldsymbol{x}_\perp) &= \mathcal{P} \exp\left(+ ig \int_{-\infty}^{x^+} dy^+ A_{cov.}^-(y^+, \boldsymbol{x}_\perp) \right), \\
V_L(x^-, \boldsymbol{x}_\perp) &= \mathcal{P} \exp\left(+ ig \int_{-\infty}^{x^-} dy^- A_{cov.}^+(y^-, \boldsymbol{x}_\perp) \right)
\end{aligned} \tag{3.18}$$

The initial condition in temporal axial gauge after performing this gauge transformation is given by

$$A^{\pm} = 0 \qquad A^i = \frac{i}{g} V \partial^i V^{\dagger} \qquad (3.19)$$

which is illustrated on the right panel of Fig. 3.1. By initializing the simulation, at a sufficiently early time $t = t_0$, where the incoming nuclei are well separated from each other, one finds that at each particular point z at most one of the two Wilson lines $V_{L/R}$ is different from the identity, and the Wilson lines in Eq. (3.16) effectively commute. Similarly, at each particular point z the corresponding gauge fields A^i vanish, or reduce to the well known solutions $A^i_{L/R}$ for individual nuclei in the respective light-cone gauge [99, 114, 115], as indicated in Fig. 3.1.

So far we have discussed the structure of the initial conditions in the continuum, and we will now address the corresponding lattice implementation. Starting from a given distribution of color charges $\rho_{L/R}(t_0, z, \boldsymbol{x}_{\perp})$ at initial time t_0 (as shown in Fig. 3.1) discretized on a spatial x, y, z grid, we first compute the covariant gauge $A^{\pm}_{cov.}(t_0, z, \boldsymbol{x}_{\perp})$ fields according to Eq. 3.15, and subsequently construct the discretized version $V_{L/R}(t_0, z, \boldsymbol{x}_{\perp})$ of the light-like Wilson lines. Since before the collision, the Wilson lines $V_R(x^+, \boldsymbol{x}_{\perp})$ are independent of x^-, the light-like Wilson lines $V_R(t_0, z, \boldsymbol{x}_{\perp})$ can be defined to end on the lattice points x, y, z at initial time t_0 as illustrated in the left panel of Fig. 3.2.

If we consider the left moving nucleus, which is initially located on the right hand side of the lattice, the corresponding Wilson line $V_R(t_0, z, \boldsymbol{x}_{\perp})$ is equal to the identity for all points z which at the time t_0 are located to the left of the incoming color charges. Starting from $V_R(t_0, z = 0, \boldsymbol{x}_{\perp}) = \mathbb{1}$ at the left boundary of the lattice ($z_i = 0$), the Wilson lines $V_R(t_0, z, \boldsymbol{x}_{\perp})$ for $z > 0$ can be constructed successively based on the relation

$$V_R(t_0, z + a_z, \boldsymbol{x}_{\perp}) = \mathcal{P} \exp\left(+ig \int_{x_2^+ = \frac{t_0+z}{\sqrt{2}}}^{x_1^+ = \frac{t_0+z+a_z}{\sqrt{2}}} dz^+ A^-_{cov.}(z^+, \boldsymbol{x}_{\perp})\right) V_R(t_0, z, \boldsymbol{x}_{\perp})$$

$$(3.20)$$

Exploiting again the invariance of the $A^-_{cov.}(x^+, \boldsymbol{x}_{\perp})$ gauge fields under shifts along
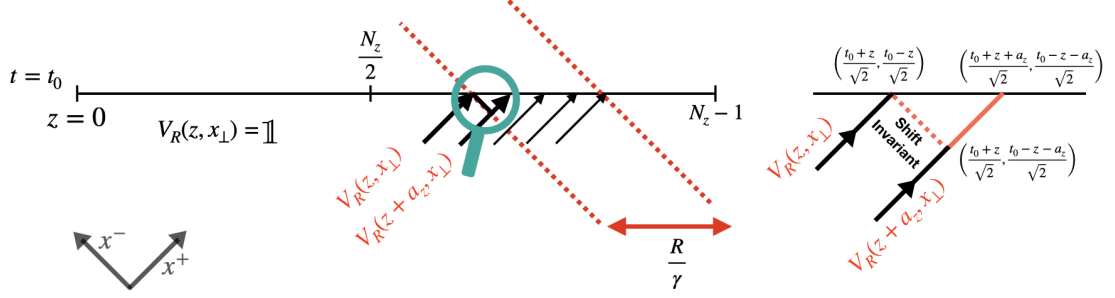
Figure 3.2: Illustration of light-like Wilson lines on t-z grid for the left moving nucleus with a finite longitudinal extent ($R_\gamma = \frac{R}{\gamma}$)

the x^- direction, the additional color rotation in Eq. 3.20 can then be approximated by parametrising the part

$$Q = \mathcal{P} \exp\left(+ ig \int_{x_2^+ = \frac{t_0+z}{\sqrt{2}}}^{x_1^+ = \frac{t_0+z+a_z}{\sqrt{2}}} dz^+ A_{cov.}^-(z^+, \boldsymbol{x}_\perp) \right)$$

as indicated in the right panel of Fig. 3.2. Using $z^+(s) = x_1^+ + s(x_2^+ - x_1^+)$ with $s \in [0,1]$, we get

$$
\begin{aligned}
Q &= \mathcal{P} \exp\left(ig(x_2^+ - x_1^+) \int_0^1 ds A_{cov}^-\left(x_1^+ + s(x_2^+ - x_1^+), \boldsymbol{x}_\perp\right) \right) \\
&= \mathcal{P} \exp\left(ig\frac{a_z}{\sqrt{2}} \int_0^1 ds A_{cov}^-\left(x_1^+ + s(x_2^+ - x_1^+), \boldsymbol{x}_\perp\right) \right) \\
&\simeq \mathcal{P} \exp\left(+ ig\frac{a_z}{\sqrt{2}} A_{cov.}^-\left(\boldsymbol{x}_\perp, x_1^+ \text{ or } x_2^+\right) \right)
\end{aligned}
\tag{3.21}
$$

Based on this, Eq. 3.20 can be modified as

$$V_R(t_0, z + a_z, \boldsymbol{x}_\perp) = \mathcal{P} \exp\left(+ ig\frac{a_z}{\sqrt{2}} A_{cov.}^-\left(t_0, z, \boldsymbol{x}_\perp\right) \right) V_R(t_0, z, \boldsymbol{x}_\perp) \tag{3.22}$$

The discretized Wilson lines for the nuclei coming from the right and left direction is then given by

$$V_{R,L}(t, \boldsymbol{x}_\perp, z) = \prod_{z_i} \exp\left(\frac{\pm iga_z}{\sqrt{2}} A_{R,L}^\mp(t, \boldsymbol{x}_\perp, z_i) \right) \tag{3.23}$$

The initial condition for the lattice gauge links are then determined from the Wilson lines as

$$U_i(t, \vec{x}) = V(\boldsymbol{x}_\perp, z)V^\dagger(\boldsymbol{x}_\perp + \hat{i}, z) \qquad U_z(t, \vec{x}) = \mathbb{1} \qquad (3.24)$$

which is obtained by expanding the exponential in Eq. 3.4 to first order. Next, in order to initialize the lattice electric fields $E_{x,I}\left(t + \frac{a_t}{2}\right)$, we make use of the update rule for the gauge links in Eq. 3.8, to express

$$E_{x,I}\left(t + \frac{a_t}{2}\right) = \frac{-ia^3}{a_I^2 a_t}\log\left(U_{x,I}(t + a_t)U_{x,I}^\dagger(t)\right) \qquad (3.25)$$

which relates the electric fields to the gauge links at times t_0 and $t_0 + a_t$. By following the same procedure as outlined above, the gauge links $U_{x,i}(t + a_t)$ are constructed from the color charges propagated by a single time step according to

$$\rho_{L,R}^a(t + a_t, \boldsymbol{x}_\perp, z) = \frac{1}{N_z}\sum_{k_z} e^{\frac{2\pi i k_z z}{N_z}} \begin{Bmatrix} e^{\mp i\omega a_t} : k_z < \frac{N_z}{2} \\ e^{\pm i\omega a_t} : k_z \geq \frac{N_z}{2} \end{Bmatrix} \sum_{z'} e^{\frac{-2\pi i k_z z'}{N_z}} \rho_{L,R}^a(t, \boldsymbol{x}_\perp, z')$$

$$(3.26)$$

with

$$\omega^2 = \frac{2}{a_z^2}\left(1 - \cos\left(\frac{2\pi k_z}{N_z}\right)\right),$$

such that the evolution of the color charges in the initialization step satisfies the lattice dispersion.

While the above procedure provide initial conditions for the lattice gauge links and electric fields in temporal axial gauge, the color charges $\rho_{L/R}(t_0, \boldsymbol{x}_\perp, z)$ are still given in covariant gauge. Instead of performing a gauge transformation of the charges, we exploit Gauss Law to determine the static currents as

$$J_{stat}^\pm\left(t + \frac{a_t}{2}, \boldsymbol{x}_\perp, z\right) = \sqrt{2}\sum_{i=1,2} D_i E^i\left(t + \frac{a_t}{2}, \boldsymbol{x}_\perp, z\right) \qquad (3.27)$$

where the factor of $\sqrt{2}$ comes from the transformation between Minkowski and light-cone coordinates. This fixes the Gauss Law for initial condition and therefore should
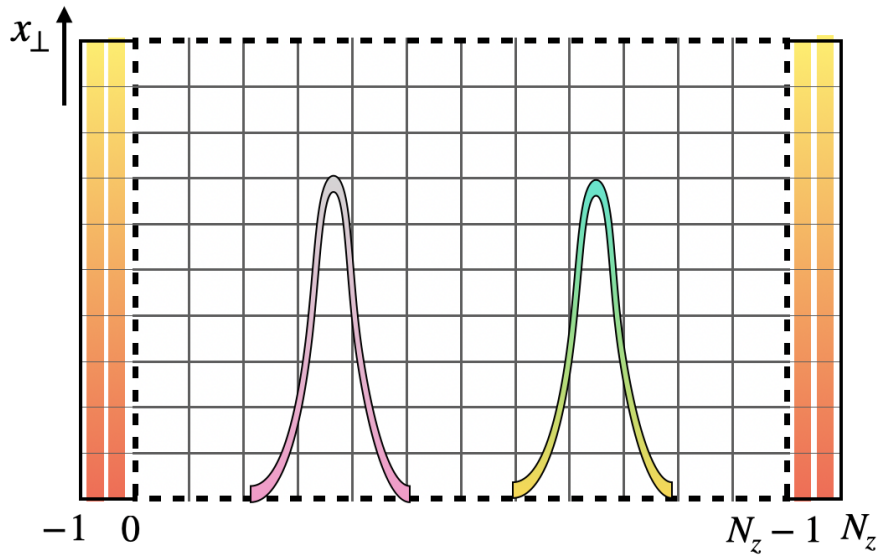
Figure 3.3: A sketch showing the front view of the simulation box with inactive transverse planes on the longitudinal edges. The dotted area portrays the real simulation box which due to fixed boundary condition requires extra cells (colored area) to compute fields at the boundary.

remain fixed at later times too. The initial value of the dynamical currents J_{dyn} is set by performing half a time step of evolution as

$$
J_{dyn}^{\pm}(t + a_t, \boldsymbol{x}_\perp, z) = \pm \frac{a_z}{a_t} \frac{1}{N_z} \sum_{k_z} e^{\frac{2\pi i k_z z}{N_z}} \begin{Bmatrix} 1 & : k_z = 0 \\ \left(\frac{e^{\pm i\omega a_t} - 1}{1 - e^{\frac{-2\pi i k_z}{N_z}}} \right) & : k_z < \frac{N_z}{2} \\ 0 & : k_z = \frac{N_z}{2} \\ \left(\frac{e^{\mp i\omega a_t} - 1}{1 - e^{\frac{-2\pi i k_z}{N_z}}} \right) & : k_z > \frac{N_z}{2} \end{Bmatrix} \times
$$
$$
\sum_{z'} e^{\frac{-2\pi i k_z z'}{N_z}} J_{stat}^{\pm}\left(t + \frac{a_t}{2}, \boldsymbol{x}_\perp, z'\right) \tag{3.28}
$$

With these initial condition, the successive dynamics namely during the collision - diamond shaped collision region in Fig. 3.1, and after collision, is then simulated numerically.

3.1.4   Ghost cells and Observables

Starting from the initial conditions outlined above, we simulate the dynamics of the collision in Minkowksi coordinates $x^\mu = (t, x, y, z)$ by solving the classical Yang-

Mills equations for the lattice gauge links and electric fields, along with the evolution equations for the eikonal currents. Since we use axial gauge, the gauge fields are non-zero and different in the limit $z \to \pm\infty$, such that periodic boundary condition can not be used. Therefore we implement fixed boundary condition with some ghost cells which remain inactive during the evolution as shown in Fig. 3.3. The entire transverse plane at $z = -1$ and $z = N_z$ are then set equal to plane $z = 0$ and $z = N_z - 1$ respectively.

While in principle the evolution can be performed up to arbitrary late times, in practice the incoming nuclei will approach these fixed boundaries from where color charges can not traverse any further. Therefore the simulation has to be stopped before this occurs.

When investigating the initial energy deposition during the collision and early-time dynamics of the Glasma, we will primarily focus on the evolution of energy momentum tensor $T^{\mu\nu}(x)$, which we compute as

$$
T^{00}(x) = \frac{1}{2}\Big(E_{loc}^2(x) + B_{loc}^2(x)\Big)
$$

$$
T^{IJ}(x) = \frac{1}{2}\Big(E_{loc}^2(x) + B_{loc}^2(x)\Big)\delta^{IJ} - E_{loc}^{I,a}(x)B_{loc}^{J,a}(x)
$$

$$
T^{0I}(x) = \epsilon^{IJK}\Big(E_{loc}^{J,a}(x) \times B_{loc}^{K,a}(x)\Big) \tag{3.29}
$$

where $E_{loc}^2(x) = E_{loc}^{I,a}(x)E_{loc}^{I,a}(x)$, and $E_{loc}(x)$ and $B_{loc}(x)$ are local electric and magnetic fields. Note that electric field is naturally evaluated at $x + a_I/2 + a_t/2$ whereas magnetic field is evaluated at $x + a_I/2 + a_J/2$. To define them at same lattice position, we calculate the electric and magnetic fields using smeared operator definitions

$$
E_{I,loc}^a(x) = \frac{a_I}{2a^3}\Big(E_I^a(x) + U_I^\dagger(x - \hat{I})E_I^a(x - \hat{I})U_I(x - \hat{I})\Big)
$$

$$
B_{loc}^{I,a}(x) = \epsilon^{IJK}\frac{a_I}{4a^3}\,\mathrm{ReTr}\Big(it^a\Big(U_{JK}(x) + U_{J-K}(x)
$$

$$
+ U_{-J-K}(x) + U_{-JK}(x)\Big)\Big) . \tag{3.30}
$$

with gauge links U in the magnetic field definition, saved at $t + dt/2$. As the main

motive of our simulation is to understand the longitudinal structure of the fields, we will frequently perform averages over the transverse plane, which we denote as

$$\left\langle T^{00}(t,z) \right\rangle_\perp = \frac{1}{N_x N_y} \sum_{\boldsymbol{x}_\perp} T^{00}(t, \boldsymbol{x}_\perp, z) \tag{3.31}$$

Based on the symmetries in particular model of nucleus, most of the components of energy momentum tensor might vanish on averaging over the color charge density. For example, rotational symmetry in MV model gives vanishing energy flux $T^{0i}, i = 1, 2$ in the transverse direction.

Besides the space-time evolution of the energy momentum tensor, we will also consider the evolution of the field intensity of longitudinal ($\parallel$) and transverse ($\perp$) components of the (chromo-) electromagnetic fields

$$B_\parallel^2(x) = \frac{2}{a_x^2 a_y^2} \mathrm{ReTr}\Big[\mathbb{1} - U_{xy}(x)\Big]$$

$$B_\perp^2(x) = \sum_{i=x,y} \frac{2}{a_i^2 a_z^2} \mathrm{ReTr}\Big[\mathbb{1} - U_{iz}(x)\Big]$$

$$E_\parallel^2(x) = \frac{1}{2 a_x^2 a_y^2} \sum_{a=1}^{N_c^2-1} \Big[E_z^a(x)\Big]^2$$

$$E_\perp^2(x) = \sum_{i=x,y} \frac{1}{2 a_i^2 a_z^2} \sum_{a=1}^{N_c^2-1} \Big[E_i^a(x)\Big]^2 \tag{3.32}$$

3.2   3+1D Collisions of individual color charges

Based on the above simulation framework, we will now study the initial energy deposition and early time dynamics of the Glasma. Before we turn to simulations involving realistic models of the color charge distributions of the colliding nuclei, it proves insightful to first consider the collision of individual ensembles of color charges, to test the framework and develop an intuitive picture of the underlying dynamics.

We follow the previous works [84, 88], and sample the transverse distribution of color charges based on the McLerran-Venugopalan (MV) model as

$$\rho_{L/R}^{a\,(2D)}(x,y) = \sum_{k_x,k_y} e^{2\pi i\left(\frac{k_x x}{N_x} + \frac{k_y y}{N_y}\right)} \frac{k^2}{k^2 + m^2} e^{-k^2/2\Lambda^2}$$
$$\sum_{x',y'} Q_s \sqrt{a_x a_y} \zeta^a(x',y') e^{-2\pi i\left(\frac{k_x x'}{N_x} + \frac{k_y y'}{N_y}\right)} \tag{3.33}$$

where $\zeta(x,y)$ are Gaussian random numbers. To cure the infrared divergence of the model, we introduce a regulator $m \sim \Lambda_{QCD}$ which enforces color neutrality on low momentum modes by cutting off the long radiative tails. Even though lattice spacing a_I introduces a momentum cut off of order $1/a_I$, we manually introduce another regulator Λ at the level of color charge distribution to make our simulations UV finite. These regulators are set in terms of a dimensionful scale Q_s as $m/Q_s = 1$ and $\Lambda/Q_s = 5$.

Subsequently, the three dimensional color charge distribution

$$\rho_{L/R}^a(x,y,z) = \rho_{L/R}^{a\,(2D)}(x,y)a_z T(z) \tag{3.34}$$

is obtained by multiplying the transverse color charge distribution with the same Gaussian profile at each point

$$T(z) = \frac{1}{\sqrt{2\pi R_\gamma^2}} e^{-z^2/2R_\gamma^2} \tag{3.35}$$

where the dimensionful parameter $R_\gamma = R/\gamma$ controls the longitudinal extent of the nucleus.

Since the initial color charge distributions are characterized in terms of the dimensionful scales Q_s and R_γ, the latter can be used to set the scale of the lattice calculation by specifying the value of $Q_s a_\perp$ and R_γ/a_z. Generally, the (transverse) lattice spacing has to be chosen sufficiently small to avoid discretization errors $Q_s a_\perp \ll 1$, while at the same time the transverse simulation volume $N_\perp a_\perp$ should be large com-

pared to the color charge correlation length $\sim 1/m$. In nutshell, we have following hierarchy in transverse scales

$$a_\perp \ll \frac{1}{Q_s} \leq \frac{1}{m} \ll N_\perp a_\perp$$

Similarly, the longitudinal color charge distribution has to be smooth on the scale of a single lattice spacing $a_z \ll R_\gamma$, while at the same time the longitudinal extend of the lattice $N_z a_z$ has to be sufficiently large to allow for a long enough time evolution after the collision. Within the above setup, we have varied both the lattice spacings $Q_s a_\perp$, R_γ / a_z as well as the lattice length $Q_s N_\perp a_\perp$ and $R_\gamma / N_z a_z$ to check that discretization errors do not play a significant role, and if not stated otherwise we will present results for $N_\perp = 128$, $N_z = 2048$ with $Q_s a_\perp = 0.125$ and $R_\gamma / a_z = 16$ in the following.

3.2.1 Stable propagation of color charges before and after the collision

Before we address the dynamics of the collision, we briefly verify that – within our numerical setup – the color charges of the individual nuclei propagate in a stable fashion. We illustrate this behavior in Fig. 3.4, where the top panel shows the evolution of the longitudinal profiles of the color charge distribution $\rho(t, x, y, z) = \sqrt{\rho_a(t, x, y, z)\rho_a(t, x, y, z)}$ at a randomly chosen point x, y in the transverse plane. By comparing the initial color charge distribution $\rho_a(t_0, x, y, z)$ determined according to Eq. 3.27, to the charge density $\rho_a(t_0, x, y, z) = V_{ab}(t_0, x, y, z)\rho_b^{\text{cov.}}(t_0, x, y, z)$ re-constructed from the color charge distribution in covariant gauge, we observe an excellent agreement demonstrating that the re-construction of the charge density based on Gauss's law works as expected. By comparing the dynamically evolved charge distribution $\rho_a(t, x, y, z)$ to the translated initial conditions $\rho_a(t_0, x, y, z - c(t - t_0))$, we can further confirm that for sufficiently small lattice spacing $a_z \ll R$, the numerical dispersion of the currents is small, such that over the relevant time scales the nuclei propagate in a stable fashion at almost the speed the light.

Beside the stable propagation of the color charges, it is also important that the gluon fields induced by the color charges propagate in a stable way along side the charges,
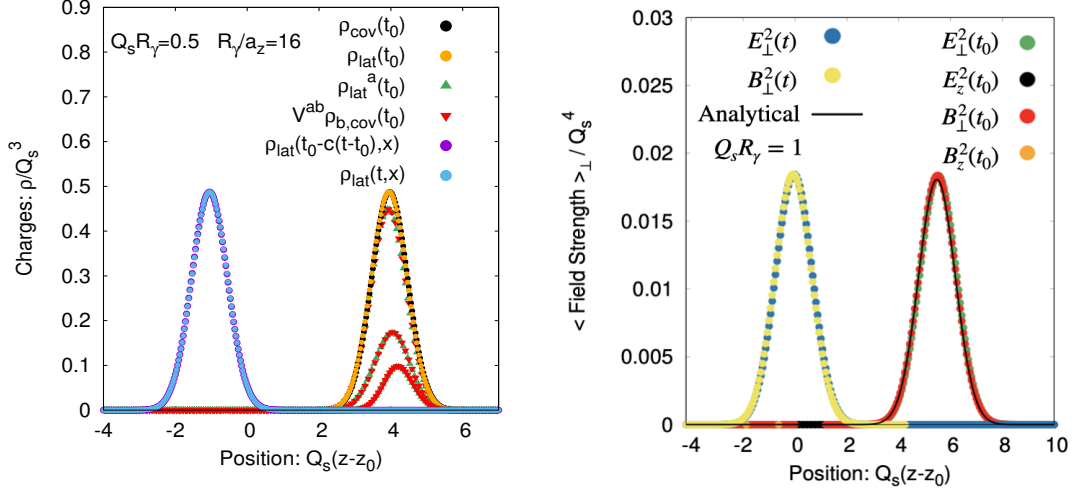
Figure 3.4: Longitudinal profile of the color charges along with the different color components at initial time t_0 and after propagation for a time $t - t_0 = 5/Q_s$ (left). Electric and magnetic field strengths of the left moving nucleus along with the analytically obtained result at initial time t_0 and at some later time $t - t_0 = 5/Q_s$, prior to the collision (right).

as can be seen from the bottom panel of Fig. 3.4, where we show the evolution of the longitudinal profiles of the average electric and magnetic field strengths $\langle E_\perp^2(t, z) \rangle_\perp$, $\langle B_\perp^2(t, z) \rangle_\perp$, $\langle E_\parallel^2(t, z) \rangle_\perp$ and $\langle B_\parallel^2(t, z) \rangle_\perp$. By comparing the longitudinal field strength profiles in Fig. 3.4 at different times, one again concludes the nuclei propagate in a stable fashion over the relevant time scales. Moreover, using the two point function of the color charge distribution in the momentum space

$$\langle \tilde{\rho}^a(\mathbf{k}_\perp, z) \tilde{\rho}^b(\mathbf{k}_\perp', z') \rangle = (2\pi)^2 Q_s^2 T(z) T(z') \delta^{ab} \delta^2(\mathbf{k}_\perp + \mathbf{k}_\perp') \tag{3.36}$$

one can also the compute the field strengths before the collision as

$$\begin{aligned}
\left\langle E^{ia}(z, x_\perp) E^{ib}(z', y_\perp) \right\rangle &= \left\langle \partial_x^i A^{-a}(z, x_\perp) \partial_y^i A^{-b}(z', y_\perp) \right\rangle \\
&= \int \frac{d^2\mathbf{k}_\perp}{(2\pi)^2} \int \frac{d^2\mathbf{k}_\perp'}{(2\pi)^2} \frac{k^i}{\mathbf{k}_\perp^2} \frac{k'^i}{\mathbf{k}_\perp'^2} \left\langle \tilde{\rho}^a(z, k_\perp) \tilde{\rho}^b(z', k_\perp') \right\rangle e^{i\mathbf{k}_\perp x_\perp + i\mathbf{k}_\perp' y_\perp}
\end{aligned} \tag{3.37}$$

On plugging in the value of the above two-point function and taking the limit $(z', y_\perp) \to (z, x_\perp)$, the trace of the correlation function $\left\langle \left(E_i^a(x_\perp, z) \right)^2 \right\rangle$ is given as

$$E_\perp^2(t_0, z) = \frac{1}{2} \frac{Q_s^2}{2} (N_c^2 - 1) T(z)^2 \int \frac{d\mathbf{k}_\perp}{2\pi} \frac{1}{\mathbf{k}_\perp} \left(\frac{\mathbf{k}_\perp^2}{\mathbf{k}_\perp^2 + m^2} \right)^2 e^{\frac{-\mathbf{k}_\perp^2}{\lambda^2}} \tag{3.38}$$

where the factor of $1/2$ in the front accounts for the conversion of light-cone coordinate to Minkowski coordinate. As seen in Fig. 3.4, the analytical result matches with the results reproduced by our real-time lattice simulations, indicating the residual discretization errors are indeed small.

3.2.2 Evolution of the fields during and after the collision

Now that we have established the validity of our setup, we will analyze the energy deposition and early time dynamics of the collisions. Before we present our numerical results, we briefly recall the structure of the Glasma fields in the high-energy boost invariant limit [28, 86, 87] which will serve as a basis for comparison. Before the collision, the incoming nuclei feature the transverse electric and magnetic fields known as the Weiszaecker-Williams fields (WW)

$$E_{WW}^i = \partial^0 A_{R/L}^i \qquad B_{WW}^i = \epsilon^{ij}\partial^z A_{R/L}^j \qquad (3.39)$$

localized in narrow strips along the light-cones. Even though the structure of the fields during the collisions is not analytically accessible, it is well established that the initial state immediately after the collision ($\tau = 0^+$) features boost invariant longitudinal electric and magnetic fields in the forward light-cone

$$E^\eta(\tau = 0, \boldsymbol{x}_\perp) = -ig\delta^{ij}V^\dagger(\boldsymbol{x}_\perp)\Big[A_L^i(\boldsymbol{x}_\perp), A_R^j(\boldsymbol{x}_\perp)\Big]V(\boldsymbol{x}_\perp)$$

$$B^\eta(\tau = 0, \boldsymbol{x}_\perp) = -ig\epsilon^{ij}V^\dagger(\boldsymbol{x}_\perp)\Big[A_L^i(\boldsymbol{x}_\perp), A_R^j(\boldsymbol{x}_\perp)\Big]V(\boldsymbol{x}_\perp) \qquad (3.40)$$

where $V(\boldsymbol{x}_\perp)$ is defined in Eq. 3.16 and we adapted the usual $\tau = \sqrt{t^2 - z^2}$ and $\eta = \tanh^{-1}(z/t)$ coordinates, with longitudinal electric and magnetic fields in the Milne coordinates defined as $E^\eta = \frac{1}{\tau}F_{\tau\eta}$ and $B^\eta = -\frac{1}{2}\epsilon^{ij}F_{ij}$, which at mid-rapidity ($\eta = 0$) are equivalent to the fields in Minkowski coordinates i.e $E^\eta|_{\eta=0} = E^z, B^\eta|_{\eta=0} = B^z$.

Subsequently, for $\tau > 0$ the initial Glasma flux tubes in Eq. 3.40 begin to expand in spatial direction leading to decoherence of strong chromo-electric and chromo-magnetic fields. After a time scale $\sim 1/Q_s$, the evolution essentially becomes free streaming, resulting in a state of approximately vanishing longitudinal pressure $p_L = T^\eta_\eta \simeq 0$ [28]. While the evolution of the boost-invariant Glasma produced in the
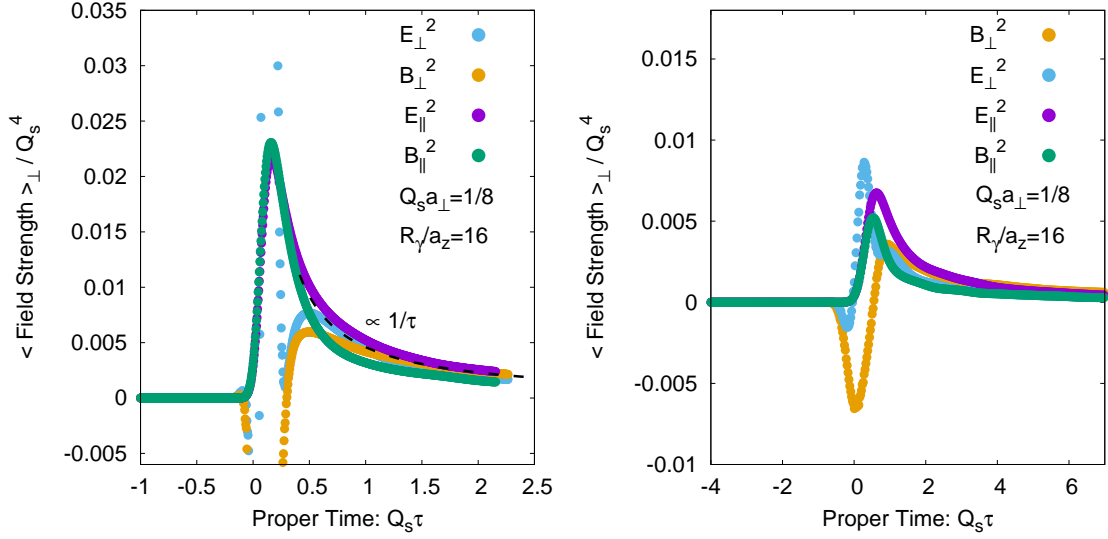
Figure 3.5: Evolution of longitudinal and transverse components of the electric and magnetic fields at the center of the collision for different longitudinal thickness: $Q_s R_\gamma = 0.0625$ (left) and $Q_s R_\gamma = 0.5$ (right).
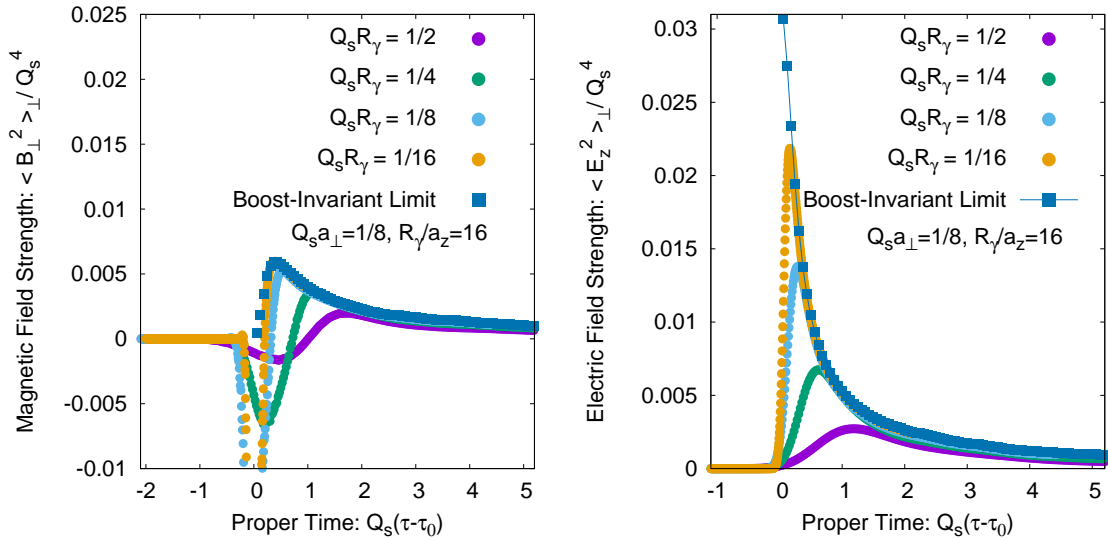
Figure 3.6: Evolution of transverse magnetic (left) and longitudinal electric (right) fields at the center of the collision for different longitudinal thickness $Q_s R_\gamma$ along with the boost invariant limit.

forward light-cone has been explored to detailed extent within numerical simulations [18, 28, 92] and (semi-)analytic calculations [86], we further note that also in the boost-invariant high-energy limit the eikonal charges receive a color rotation during the collision, and the transverse electric and magnetic fields continue to exist in narrow strips along the light-cones.

Beyond the high-energy boost invariant limit, the formation of the Glasma begins as soon as the color charge distributions of the incoming nuclei start to overlap and persists over an extended period of time until the colliding nuclei have passed through each other. Now in order to analyze the formation of the 3+1D Glasma, we first consider the evolution of the fields at the center of the collision ($z = 0$), where one has $\tau = t$ and $\eta = 0$ such that the descriptions in Minkowski (t, z) coordinates and Milne (τ, η) coordinates coincide. We present our results in Fig. 3.5, where we show the time evolution of the longitudinal and transverse electric and magnetic fields strength during and after the collision for two different values of $Q_s R_\gamma = 1/4$ and $Q_s R_\gamma = 1/16$ corresponding to different longitudinal thickness of the colliding nuclei. Since we want to focus on the creation of the Glasma, we have subtracted the field strength associated with Weiszaecker-Williams fields of the colliding charges, i.e. we consider $E^2_{\text{Glasma}}(t, z) = E^2(t, z) - E^2_{WW}(t, z)$, and we have defined the origin of the coordinate system such that at $t = 0$ the charge distributions of the colliding nuclei maximally overlap with each other.

During the collision longitudinal electric and magnetic fields build up monotonically as the two nuclei pass through each other, while the transverse electric and magnetic components experience rapid changes. By the time that the incoming nuclei have passed each other, which corresponds to $Q_s t \simeq 0.25$ in the left panel and $Q_s t \simeq 1$ in the right panel, the transverse electric and magnetic fields become small again and longitudinal electric and magnetic fields dominate the energy density. While close to the boost-invariant limit for $Q_s R_\gamma = 1/16$ the longitudinal electric and magnetic fields have approximately the same magnitude, the longitudinal magnetic field strength is suppressed compared to the longitudinal electric field for $Q_s R_\gamma = 1/4$ i.e away from the boost invariant limit. Similar behaviour was observed in [46] along with stronger dependency on infrared regulator m.
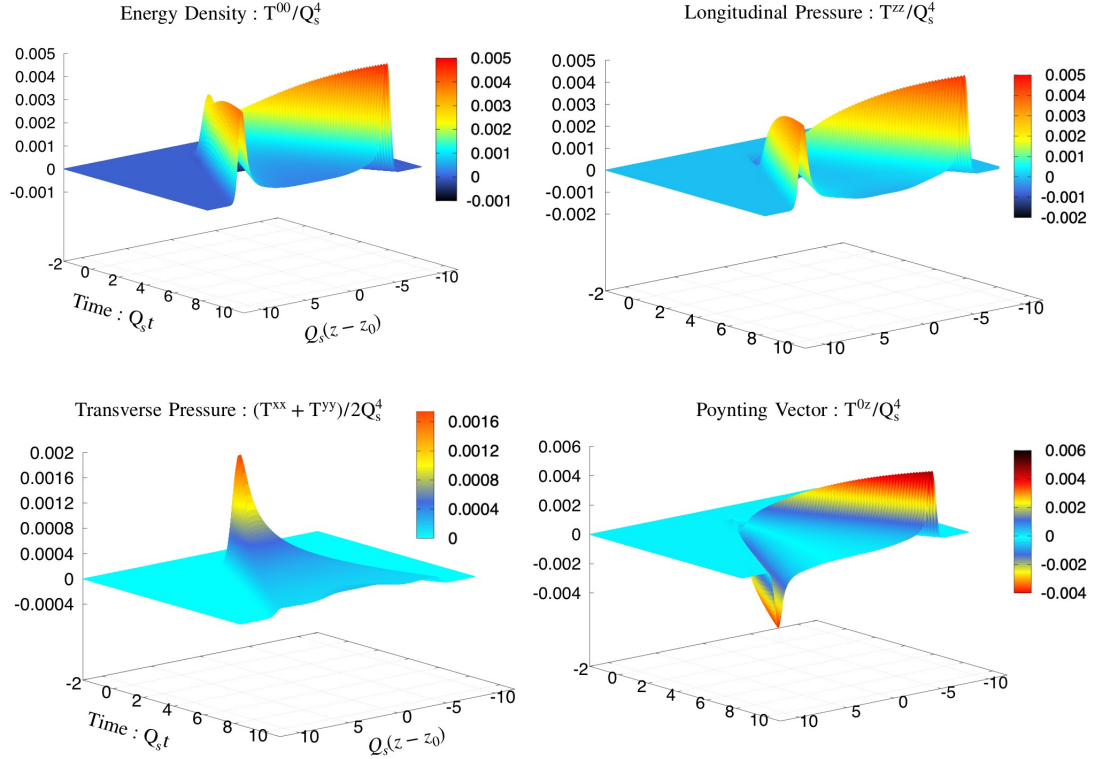
Figure 3.7: Space-time evolution of the non-zero components of the energy momentum tensor: T^{00}/Q_s^4, T^{ZZ}/Q_s^4, $(T^{XX} + T^{YY})/2Q_s^4$ and T^{0Z}/Q_s^4 obtained after averaging over the transverse plane in the Minkowski coordinates. Simulations are performed for a single event of a thick nuclei $(Q_s R_\gamma = 0.5)$

Eventually, as the colliding nuclei have passed through each other, transverse electric and magnetic fields are regenerated from their longitudinal counterparts, until at late times the different components become of comparable magnitude. Similar to the boost-invariant case, the different field intensities at the center of the collision $(z = \eta = 0)$ then start to decay as approximately $\propto 1/\tau$ as indicated by the black dashed lines in Fig. 3.5 Next we will investigate the dependence of the initial energy deposition and early time dynamics on the longitudinal thickness. In Fig. 3.6 we present the evolution of transverse magnetic and longitudinal electric fields for different values of $Q_s R_\gamma$ characterizing the longitudinal thickness of the colliding nuclei.[1] Alongside the results from 3+1D numerical simulations, we also show res-

---

[1]Similar behavior can be observed for the longitudinal magnetic and transverse electric components which are not depicted here.

ults for the boost invariant limit, obtained by performing $2 + 1$D boost-invariant classical Yang-Mills simulations for the same color charge distributions, using the infinite Wilson lines $V_{L/R}(x_\perp)$ as an input. Starting from the collision of thick nuclei with $Q_s R_\gamma = 1/2$, where the collision takes a significant amount of time and the evolution of $B_\perp^2(t, z = 0)$ and $E_\parallel^2(t, z = 0)$ shows a smooth transition between the different stages, the decrease/increase of the transverse magnetic/longitudinal electric field strength during the collision sharpens significantly as the collision becomes shorter and shorter for smaller values of $Q_s R_\gamma$. Conversely, the evolution of the fields after the collision for $Q_s t \gtrsim Q_s R_\gamma$ is rather insensitive to the longitudinal thickness, and the results for 3+1D collisions smoothly approach the boost-invariant result as $Q_s R_\gamma \to 0$. This behaviour was expected since a detector kept far away could never differentiate between a nuclei with or without any longitudinal support.

So far we have focused on the time evolution in the center of the collision ($z = 0$), and we will now analyze space-time evolution of longitudinal profiles of the collision in more detail. Instead of showing results for the individual field strength components, we will focus on the evolution of the dominant components T^{00}, T^{0z}, T^{zz} and T^{ii} of the energy momentum tensor, and similar to our previous result subtract the contributions $T^{00}_{WW} = T^{zz}_{WW} = \pm T^{0z}_{WW}$ of the Weizsaecker-Williams fields to the energy momentum tensor. Primarily, pure Glasma fields can be obtained by subtracting the fields of nuclei before the collision at each lattice point but to make sure that we were not messing around, we preferred taking a long route and performed three independent simulations, where in the first case we simulate the full collision, while the other two simulations simply propagate of the left/right moving charges. The subtraction takes into account the non-zero dispersion of the color charges due to residual discretization errors, and the energy-momentum tensor of the Glasma $T^{\mu\nu}_{\text{Glasma}} = T^{\mu\nu}_{full} - T^{\mu\nu}_{WW,L} - T^{\mu\nu}_{WW,R}$ vanishes identically before the two incoming nuclei collide.

Our results for the space-time evolution evolution of the energy-momentum tensor are compactly summarized in Fig. 3.7, where the different panels show the t, z dependence of the various components of $\langle T^{\mu\nu}_{\text{Glasma}} \rangle_\perp$ in the lab-frame averaged over the transverse plane. By focusing on the evolution of the transverse pressure $(T^{xx} + T^{yy})/2$,

one clearly observes the energy deposition in the central region where $(T^{xx} + T^{yy})/2$ increases during the collision, exhibits a pronounced peak and subsequently decreases due to the rapid longitudinal expansion of the Glasma. However, in addition to the energy deposition in the central region, we also observe rather large contributions to T^{00}, T^{0z} and T^{zz} in the vicinity of the two light-cones. While it is intuitively clear that the non-equilibrium plasma produced away from central region should feature sizeable velocities in the longitudinal direction and therefore contribute significantly to T^{00}, T^{0z} and T^{zz} in the lab-frame, the magnitude of contributions is surprisingly large compared to the transverse pressure. Even though we can not clearly rule out that these contributions may arise due to artifacts of the lattice discretization, we have checked explicitly that the observed behavior remains unchanged when we decrease the lattice spacing, as discussed in more detail in Appendix A. Since to the best of our knowledge such behavior has not been reported previously in the context of 3+1D Glasma simulations, clarifying the detailed structure of the fields in the vicinity of the light-cone will require further numerical and analytical investigations in future.

While the results in Fig. 3.7 were obtained for the collision of rather thick nuclei $(Q_s R_\gamma = 1/2)$, it is also interesting to investigate how the space-time profiles change when varying the longitudinal thickness $Q_s R_\gamma$ of the colliding nuclei. We investigate this behavior in Fig. 3.8, where we present heat-map figures of the space-time evolution of the transverse pressure $(T^{xx} + T^{yy})/2$ for $Q_s R_\gamma = 1/2$, overlayed with the τ, η coordinate system in the forward light-cone, by indicating lines of constant time $Q_s \tau$ and constant space-time rapidity η.

While the results for the collision of thin nuclei $(Q_s R_\gamma = 1/16)$ closely resemble the behavior in the boost invariant limit, as lines of constant transverse pressure $(T^{xx} + T^{yy})/2$ coincide well with lines of proper time $Q_s \tau$ within the central rapidity region $(\eta \lesssim 1)$, clear deviations from boost-invariance emerge when considering the collision of nuclei with a large longitudinal extent $(Q_s R_\gamma = 1/2)$. Most importantly, one observes that for $Q_s R_\gamma = 1/2$ the transverse pressure is significantly reduced towards the edges of the forward light-cone, indicating a non-trivial space-time rapidity profile around mid-rapidity.
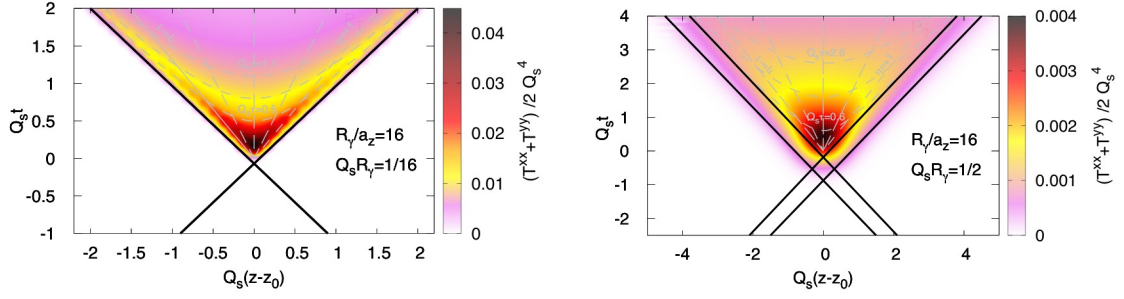
Figure 3.8: Heat-map figures for the space-time evolution of the transverse pressure $\langle P_T(t,z)\rangle_\perp$ overlayed with grey dashed τ, η lines for thin nuclei $Q_s R_\gamma = 0.0625$ (left) and thick nuclei $Q_s R_\gamma = 0.5$ (right).
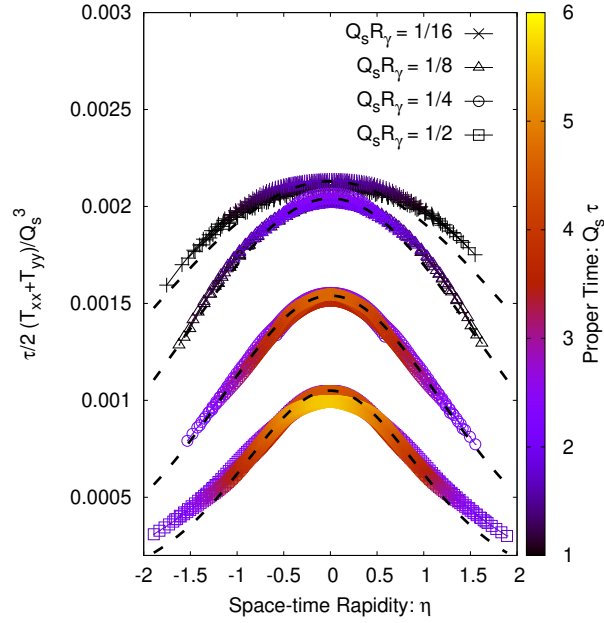
Figure 3.9: Rapidity profiles of the transverse pressure for various nuclear thickness $Q_s R_\gamma$. Color coding shows the different proper-time.

3.2.3 Space-time rapidity profiles

So far, we have leveraged our framework to study the space-time picture of the collision in Minkowksi space. Now we will look at the non-trivial rapidity dependence of the observables, which arises naturally by including the longitudinal thickness of the colliding nuclei. Even though the mapping of (t, z) data into (τ, η) coordinates is in principle straightforward, the availability of information on a discrete t, z grid [2] poses additional challenges, as a straightforward interpolation between data points can become problematic in the vicinity of the light cones. Due to these technical difficulties, we will re-strict ourselves to an investigation of the rapidity range $\eta \in (-1.25, 1.25)$, and show the corresponding result for different τ as a function of η. We further note that the conversion of Minkowski (t, z) space results to Milne coordinates τ, η can in fact be quite sensitive to the definition of the origin of the coordinate system, and we will always fix the origin $t = 0, z = 0$ at the space-time point, where the center of mass of the two nuclei coincides.

In Fig. 3.9, we present the evolution of transverse pressure $\tau(T^{xx} + T^{yy})/2$ as a function of η for different values of $Q_s R_\gamma$. Different color codings in Fig. 3.9 correspond to the results obtained at different proper times τ, and the scaling of the transverse pressure by a factor of τ has been chosen such that – beyond time scales $\tau \sim 1/Q_s$ – the quantity $\tau(T^{xx} + T^{yy})/2$ shown in Fig. 3.9 becomes independent of proper time τ in the boost-invariant high-energy limit. Starting from the collision of thin nuclei with $Q_s R_\gamma = 1/16$, we observe the emergence of a boost-invariant plateau for $\eta \in (-0.8, 0.8)$, as already seen in the bottom panel of Fig. 3.8, where shortly after the collision the contours of constant transverse pressure follows the line of constant proper time τ. When increasing the longitudinal thickness of the colliding nuclei, the transverse pressure of the Glasma created around mid-rapidity decreases and we see how the profiles are no longer flat around the central rapidity even for the late times $Q_s t \gg Q_s R_\gamma$. Empirically, we find that the resulting rapidity profiles can be

---

[2]Even though the time step a_t is typically small, we only create output of the energy momentum tensor every 100 steps, in order to keep the overall data size reasonable.

$Q_s R_\gamma$	η_R	$\tau P_T / Q_s^3 (\eta = 0)$
1/16	2.48	0.0021
1/8	1.69	0.0020
1/4	1.20	0.0015
1/2	0.98	0.0010

Table 3.1: Parameters of fit function defined in Eqn. 3.41

reasonably well described by the following functional form, which is indicated by the black dashed lines in Fig. 3.9,

$$\tau P_T(\eta) = \frac{\tau P_T(\eta = 0)}{\cosh(\eta/\eta_R)} \, , \qquad (3.41)$$

where $\tau P_T(\eta = 0)$ is the pressure at mid-rapidity and η_R describes the rapidity width. By looking at the extracted values of η_R and $\tau P_T(\eta = 0)$ in Tab. 3.1, one observes that the rapidity width η_R exhibits a strong dependence on the width $Q_s R_\gamma$ of the colliding nuclei, whereas the transverse pressure $\tau P_T(\eta = 0)$ of the Glasma at mid-rapidity only decreases slowly with increasing thickness of the colliding nuclei, as can also be seen directly from Fig. 3.9.

When analyzing the rapidity dependence of the other components of the energy-momentum tensor, it is convenient to switch to the local rest frame (LRF), defined by the condition that u_{LRF}^μ is a time-like eigenvector of the energy-momentum tensor $T^\mu_{\ \nu} u_{LRF}^\nu = \epsilon_{LRF} u_{LRF}^\mu$. The reason for this vague choice is twofold: firstly, the $\tau - \eta$ frame is suitable for boost-invariant collision and secondly, this frame is quite sensitive to the definition of origin, as mentioned earlier.

By diagonalizing the average stress-energy tensor $T^\mu_{\ \nu, Glasma}$ of the Glasma,[3] one gets the energy density and longitudinal pressure P_L in this frame as

$$\epsilon_{LRF} = \frac{1}{2}\left(T^{00} - T^{zz} + \sqrt{\left(T^{00} + T^{zz}\right)^2 - 4T^{0z}T^{0z}}\right)$$
$$P_{L_{LRF}} = \frac{1}{2}\left(T^{00} - T^{zz} - \sqrt{\left(T^{00} + T^{zz}\right)^2 - 4T^{0z}T^{0z}}\right) \qquad (3.42)$$

We show our results in Fig. 3.10, where we present results for the energy density

---

[3]Note that, as discussed previously, the energy-momentum tensor of the Glasma $T^{\mu\nu}_{Glasma}$ is obtained by subtracting the contributions of the Weiszaecker-Williams fields of the colliding nuclei, prior to the diagonalization procedure
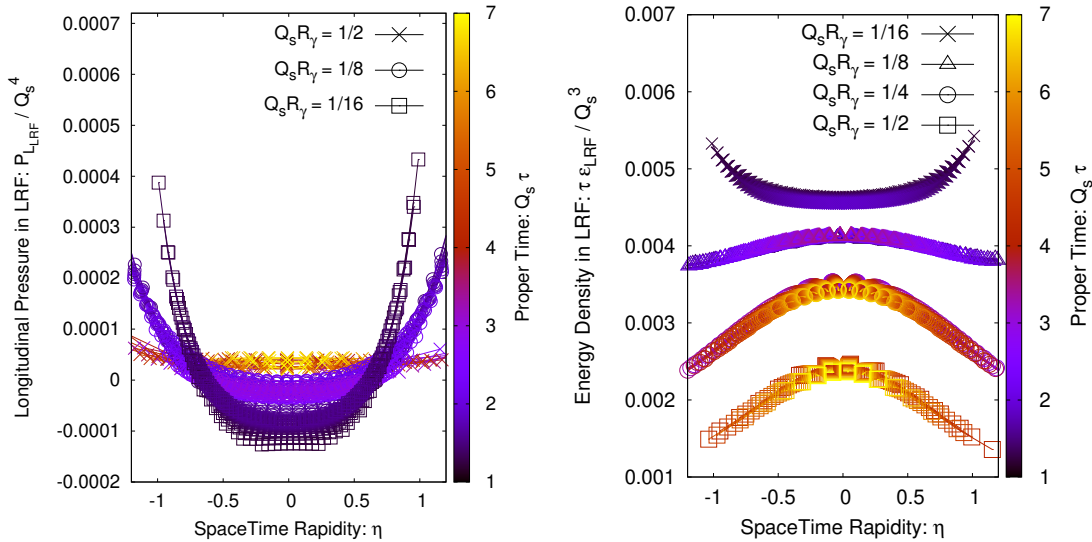
Figure 3.10: Rapidity profiles of the longitudinal pressure (left) and the energy density (right) in local-rest frame for different thickness of the colliding nuclei.

$\tau\, \epsilon_{LRF}$ and longitudinal pressure $P_{L_{LRF}}$ for different values of $Q_s R_\gamma$. Starting with the evolution of the longitudinal pressure depicted in the left panel, we find that for collisions of thick nuclei, the longitudinal pressure almost vanishes as the two nuclei have passed through each other, as seen for $Q_s R_\gamma = 1/2$ at late times. With decreasing thickness, the longitudinal pressure starts out from negative values around mid-rapidity, and subsequently relaxes towards zero, in qualitative agreement with the well established behavior in the high-energy boost-invariant limit [28, 87]. Conversely, the rise of the longitudinal pressure $P_{L_{LRF}}$ at larger rapidities signifies clear deviations from boost invariance, and can be attributed to the spurious presence of fields on/near the light-cones in Fig. 3.7

In the right panel of Fig. 3.10 we present energy density for different longitudinal extent of nuclei, at late times where longitudinal pressure almost vanishes (left panel), such that $\epsilon_{LRF} \simeq 2P_T$ and $\tau\epsilon_{LRF} \simeq const$ is approximately constant. Similar to Fig. 3.9, we again notice the emergence of a boost-invariant plateau in the high-energy limit ($Q_s R_\gamma = 1/16$), whereas for the collision of thick nuclei at lower energies ($Q_s R_\gamma = 1/2, 1/4$) we see contrasting result which again signifies broken boost-invariance.

3.3 3+1 D Collisions with realistic color charge distributions

So far we have considered a simplistic model of color charge distributions inside each nucleus, to perform a detailed investigation of the longitudinal dynamics of the Glasma during and shortly after the collision. Evidently, to connect these simulations to realistic heavy-ion collisions, it is necessary to develop a more physical model of the color charge distributions, which reflect both the longitudinal and transverse structure of the colliding nuclei. Similar to the discussion in the boost invariant high energy limit [18, 83, 84], the basic idea of our construction will be to connect the color charge distributions $\rho_{L/R}(x^\pm, \boldsymbol{x}_\perp)$, to measurements of hadronic structure functions from the deep-inelastic scattering experiments. Below we develop a model of the three-dimensional structure of the color charge distribution based on the small-x transverse momentum distribution (TMDs), and subsequently perform simulations within this framework to study the effect of longitudinal fluctuations of the color charge distributions.

3.3.1 Connection to small-x TMDs

Generally speaking, the three-dimensional parton of nucleons and nuclei is encoded in an underlying Wigner distribution [116, 117] that contains information on the position and momenta of single partons inside a nucleon or nucleus. By disregarding position or momentum information, the Wigner distribution reduces to a transverse momentum parton distribution (TMD) or respectively to a generalized parton distribution (GPD). Conversely, if both position and momentum information are discarded, one obtains the standard collinear parton distribution function (PDF).

Even though a modeling of the color charge distribution based on the Wigner function would be desirable, little is known about this fundamental object, and we will therefore consider a parametrization of the color charge densities based on TMDs, with the three dimensional spatial structure of nucleons and nuclei imposed by hand according to a Monte Carlo Glauber model. Specifically, we will assume that the

position and momentum dependence of the color charge distribution inside a nucleon can be factorized as

$$\left\langle \rho^a(x)\rho^b(y) \right\rangle = \delta^{ab} T\left(\frac{x+y}{2}\right)\Gamma(x-y) \, , \tag{3.43}$$

where $T\left(\frac{x+y}{2}\right)$ captures the spatial structure of the colliding nucleon, and thus varies on length scales $\sim R_p$ and $\sim R_p/\gamma$, where R_p is the proton radius, whereas the Fourier transform of $\Gamma(x-y)$ describes the transverse and longitudinal momentum dependence of color charges inside the nucleus, such that e.g. in the transverse plane $\Gamma(x-y)$ typically varies on distance scales $\sim 1/Q_s$.

Now in order to constrain the behavior of $\Gamma(x-y)$, we consider the small-x limit operator definition of the dipole gluon TMD for a left moving nucleus [118, 119]

$$x_2 G^{(2)}(x_2, \boldsymbol{k}_\perp) = \frac{4}{\langle p_A | p_A \rangle} \int_{-\infty}^{\infty} d\xi^+ d\xi'^+ \frac{d^2\boldsymbol{\xi}_\perp d^2\boldsymbol{\xi}'_\perp}{(2\pi)^3} e^{ix_2 p^-(\xi^+ - \xi'^+)} e^{-i\boldsymbol{k}_\perp(\boldsymbol{\xi}_\perp - \boldsymbol{\xi}'_\perp)}$$
$$\left\langle p_A | \mathrm{Tr}\left[F_\xi^{i-} U_{[\xi,\xi']} F_{\xi'}^{i-} U_{[\xi',\xi]} \right] | p_A \right\rangle \tag{3.44}$$

where $x_2 = k^-/p^-$ is the longitudinal momentum fraction and $k_\perp$ is the transverse momentum of the gluons. The gauge links $U_{[\xi,\xi']}$ and $U_{[\xi',\xi]}$ connecting the points ξ and ξ' ensures a gauge invariant definition of the TMD distributions.

Within the Color Glass Condensate effective theory, the matrix element $\langle p_A|...|p_A\rangle/\langle p_A|p_A\rangle$, is replaced by an average $\langle . \rangle$ over the color charge distribution [118, 119]

$$x_2 G^{(2)}(x_2, \boldsymbol{k}_\perp) = 4 \int_{-\infty}^{\infty} d\xi^+ d\xi'^+ \frac{d^2\boldsymbol{\xi}_\perp d^2\boldsymbol{\xi}'_\perp}{(2\pi)^3} e^{ix_2 p^-(\xi^+ - \xi'^+)} e^{-i\boldsymbol{k}_\perp(\boldsymbol{\xi}_\perp - \boldsymbol{\xi}'_\perp)}$$
$$\left\langle \mathrm{Tr}\left[F_\xi^{i-} U_{[\xi,\xi']} F_{\xi'}^{i-} U_{[\xi',\xi]} \right] \right\rangle \tag{3.45}$$

Based on eqn. (3.4,3.15) the non-abelian field strength tensor $F^{i-}(\xi)$ and gauge links $U_{[\xi,\xi']}, U_{[\xi',\xi]}$, can be calculated as functional of the color charge density ρ, such that the x_2 and $\boldsymbol{k}_\perp$ dependence of the dipole TMD $x_2 G^{(2)}(x_2, \boldsymbol{k}_\perp)$ is in fact entirely determined by specifying the $n-$point correlation functions of the color charge density.

Evidently, the general relation between the correlation functions of ρ and the dipole TMD is rather complicated, and we will thus simplify the problem by considering

Gaussian correlations of color charges in the dilute limit, where the expression in Eq. (3.45), can be expanded to lowest non-trivial order in ρ's.

$$x_2 G^{(2)}(x_2, \boldsymbol{k}_\perp) = 4(N_c^2 - 1) \int_{-\infty}^{\infty} \frac{d^2 \boldsymbol{\Delta \xi} d\Delta \xi^+}{(2\pi)^3} e^{ix_2 p^- \cdot \Delta \xi^+} e^{-i\boldsymbol{k}_\perp \Delta \xi} \int d^2 \bar{\boldsymbol{\xi}} d\bar{\xi}^+ \frac{d^2 \boldsymbol{q}_\perp \, d^2 \boldsymbol{q}'_\perp}{(2\pi)^4}$$
$$e^{i\boldsymbol{q}_\perp (\bar{\boldsymbol{\xi}} + \boldsymbol{\Delta \xi}/2)} e^{i\boldsymbol{q}'_\perp (\bar{\boldsymbol{\xi}} - \boldsymbol{\Delta \xi}/2)} \left\langle \frac{iq_i}{\boldsymbol{q}_\perp^2} \frac{iq'_i}{\boldsymbol{q}'^2_\perp} \rho(\bar{\xi}^+ + \Delta \xi^+/2, \boldsymbol{q}_\perp) \rho(\bar{\xi}^+ - \Delta \xi^+/2, \boldsymbol{q}'_\perp) \right\rangle$$

(3.46)

where we have used the average $\bar{\xi} = (\xi + \xi')/2$ and difference coordinate and $\Delta \xi = \xi - \xi'$. On evaluating the above two-point correlation functions according to Eq. (3.43) and using the dirac delta function, one gets

$$x_2 G^{(2)}(x_2, \boldsymbol{k}_\perp) = \frac{4 N_c C_F}{(2\pi)^3} \frac{\tilde{\Gamma}(\boldsymbol{k}_\perp, x_2 p^-)}{\boldsymbol{k}_\perp^2} S_\perp$$

(3.47)

where $p^- = \sqrt{s_{NN}/2}$ is the large light-component of momentum of the nucleon in the lab frame and $S_\perp = \int d\xi^+ \int d^2 \boldsymbol{\xi}_\perp T(\boldsymbol{\xi}_\perp, \xi^+)$ is the transverse area of the nucleon. Based on Eq. (3.47), where $\tilde{\Gamma}$ denotes the Fourier transform of $\Gamma(x - y)$, one then concludes that the $\boldsymbol{k}_\perp$ dependence of the $x_2 G^{(2)}(x_2, \boldsymbol{k}_\perp)$ determines the transverse structure of the correlation function $\Gamma(x - y)$, whereas the longitudinal structure of the correlation function $\Gamma(x - y)$ is related to the x_2 dependence of the TMD.

Now in order to employ Eq. (3.47) to determine the correlation function, we still need a parametrization of the gluon TMD $x_2 G^{(2)}(x_2, k_\perp)$ as input to the calculation. We will employ the GBW Model [120] – a simple phenomenological model that has been fit to small-x deep-inelastic scattering data – where

$$x_2 G^{(2)}(x_2, \boldsymbol{k}_\perp)\Big|_{x_2 = x_0} = \frac{N_c S_\perp}{2\pi^3 \alpha_s} \frac{\boldsymbol{k}_\perp^2}{Q_s^2(x_2)} \exp\left[-\frac{\boldsymbol{k}_\perp^2}{Q_s^2(x_2)} \right]$$

(3.48)

with the saturation scale $Q_s(x)$ parameterized as [120]

$$Q_s(x) = Q_0 x^{-\lambda}(1 - x) \, ,$$

(3.49)

with $\lambda = 0.144$ and the value of Q_0 being set to 0.5 GeV. Since the color charges are assumed to be x^- independent, the light-cone component k^+ vanishes identically for each source, such that in terms of the spatial momenta $k^- = -\sqrt{2}k_z$ and the

momentum fraction is given by $x_2 = \frac{k^-}{p^-}$. Based on Eq. (3.48), the correlation function $\tilde{\Gamma}(\boldsymbol{k}_\perp, k_z)$ of the initial color charges is then obtained as

$$\tilde{\Gamma}(\boldsymbol{k}_\perp, k_z) = \frac{8\pi}{g^2} \frac{N_c}{N_c^2 - 1} \frac{\boldsymbol{k}_\perp^4}{Q_s^2(x_2)} \exp\left(-\frac{\boldsymbol{k}_\perp^2}{Q_s^2(x_2)}\right) \tag{3.50}$$

which can be used to sample individual configurations of the color charge density as discussed below.

3.3.2 Sampling of realistic color charge distributions

When describing the color charge distributions of atomic nuclei, we follow the Monte Carlo Glauber Model and sample the position x_i of the $i = 1, \cdots, A$ individual nucleons according to a Wood-Saxon distribution. Each individual nucleon is assigned a three-dimensional thickness profile

$$T_i(x, y, z) = \frac{\gamma}{\sqrt{2\pi R_p^2}} e^{\frac{-(x-x_i)^2 - (y-y_i)^2 - (z-z_i)^2\gamma^2}{2R_p^2}} \tag{3.51}$$

such that the overall thickness of the nucleus is given by

$$T(x, y, z) = \sum_{i=1}^{A} T_i(x, y, z) . \tag{3.52}$$

which according to Eq. (3.47) is normalized such that $\int d^3x \, T(x) = 2\pi R_p^2 \, A$, where $R_p = 2\text{GeV}^{-1}$ is the proton radius. Since the spatial distribution T typically varies on distance scales $\sim R_p \ll 1/Q_s$, the color charge distribution inside the nuclei is then sampled according to

$$\rho_{L/R}^a(t, x, y, z) = g a_x a_y a_z \sqrt{T(x, y, z)} \int d^2\boldsymbol{k}_\perp dk_z \sqrt{\tilde{\Gamma}(t, \boldsymbol{k}_\perp, k_z)} \tilde{\zeta}^a(\boldsymbol{k}_\perp, k_z) e^{i\boldsymbol{k}_\perp \boldsymbol{x}_\perp + k_z z} \tag{3.53}$$

where $\zeta(\boldsymbol{x}_\perp, z) = 1/a^{3/2}\chi_{RNG}(\boldsymbol{x}_\perp, z)$ are Gaussian random numbers and $\tilde{\zeta}(\boldsymbol{k}_\perp, k_z)$ denotes their Fourier transform. Based on the initial conditions for the charge density profiles in Eq. (3.53), we then proceed as described in Sec. 3.1 to set up the initial conditions and simulate the dynamics of the collision. We note that due to the presence of longitudinal fluctuations, a finer discretization in the longitudinal (z)

direction is required in this case, and unless stated otherwise, we will employ $Q_0 a_\perp = 0.33$ and $R_p/a_z = 256$ in our numerical studies.

3.3.3 Numerical results for realistic charges

We now proceed to the study of the collision dynamics for realistic charge profiles, and consider head on ($b = 0$) Au-Au collisions for center of mass energies of 130 and 200 GeV. Since the basic features of the reaction dynamics remain essentially the same as for the simplistic charge profiles discussed in Sec. 3.1, we will focus our investigation on the violations of boost invariance and study the longitudinal fluctuations which emerge naturally within our framework.

We illustrate the full $3 + 1$ D structure in Fig. 3.11, which shows the different phases of the collision for one particular event of head-on Au-Au collision at $\sqrt{s_{NN}} = 200$ GeV. In the left panel, we show the energy density T_{WW}^{00} associated with the color fields of the incoming nuclei, which are well separated at $t = -0.37$ fm/c before the collision. Grey spheres overlaid to the energy density profile indicate the positions of nucleons, which dominate the longitudinal and transverse large scale structure of the energy density inside the nucleus. Small scale fluctuations of the color charge distribution results in additional inhomogeneities, clearly visible in the second nucleus. The central panel of Fig. 3.11 shows the three dimensional profile of the transverse pressure $(T^{xx} + T^{yy})/2$ at the time of the collision $t = 0$ fm/c i.e. when the incoming nuclei maximally overlap with each other. Since at this point, some of the individual nucleon-nucleon collisions have already taken plane, one starts to see formation of Glasma flux tubes of varying length, along with their fluctuations in the longitudinal and transverse direction. Subsequently, the Glasma flux tubes expand into longitudinal and transverse space, as can be seen from the right panel, showing the transverse pressure for a late time $t = 0.6$ fm/c after the collision. Despite the fact that the individual flux tubes are stretched out along the longitudinal direction, as a consequence of fluctuation one observes clear non-uniformities of the flux tubes, along with asymmetries in the forward and backward profiles.

Since at late times the rapid longitudinal expansion of the system stretches out the
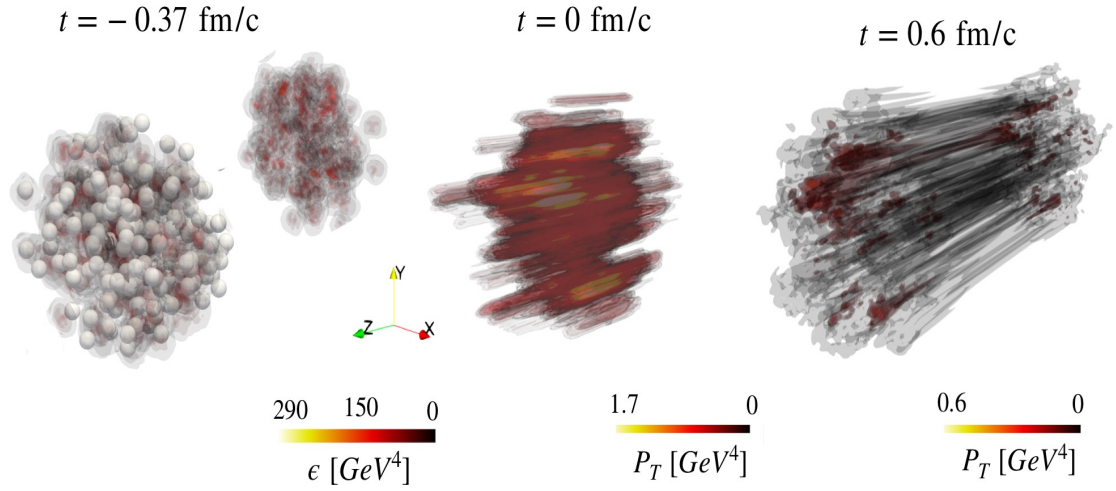
Figure 3.11: Illustration of 3D energy density with the position of nucleons as indicated by small grey spheres (left), transverse pressure during the collision (center) and after the collision (right) for a single event of $Au - Au$ collision at 200 GeV.

Figure 3.12: Three dimensional rendered view of transverse pressure at $\tau \simeq 0.4$ fm/c in Milne coordinates for a single event of Au-Au collision at $\sqrt{s_{NN}} = 130$ GeV.
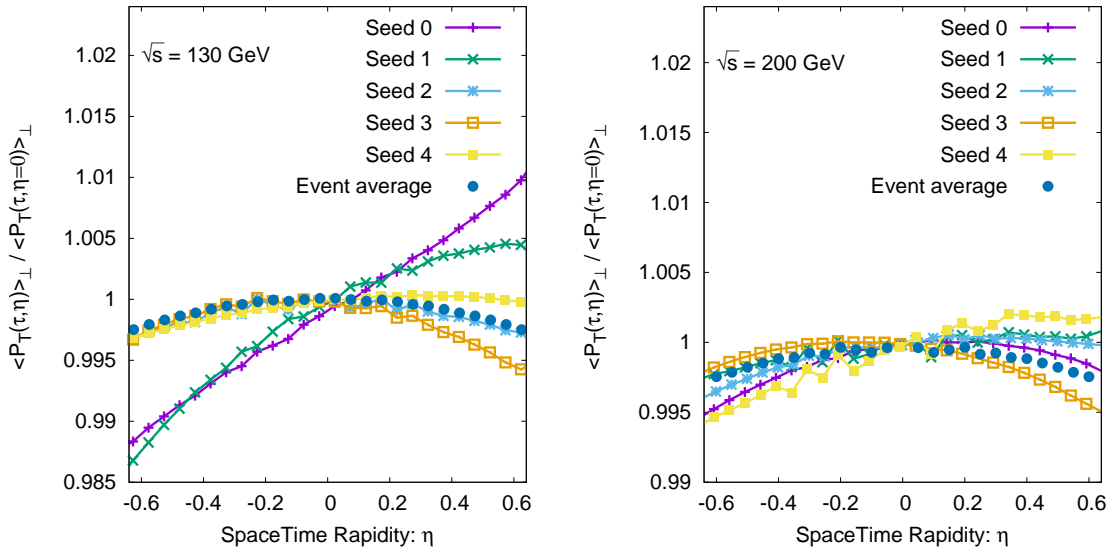
Figure 3.13: Integrated transverse pressure as a function of space-time rapidity for average and individual runs at center of mass energies of 130 and 200 GeV

longitudinal profiles, some of the features of the Glasma are not clearly visible in the above figure and it is advantageous to visualize the corresponding structure in Milne coordinates. We illustrate this in Fig. 3.12, where we show the three dimensional profile for a head-on Au-Au collision at 130 GeV in x, y and η coordinates at $\tau \simeq$ 0.4 fm/c, which characterises the rapidity fluctuations. We note that due to limited availability of points near the light cone, we restrict ourselves to the central rapidity range $\eta \in [-0.8, 0.8]$. Since at times $\tau \simeq 0.4$ fm/c the color charges of the colliding nuclei have escaped the central region, the transverse pressure profiles around mid rapidity are well described by approximately boost invariant flux tubes of varying transverse extent, and resemble the structures put forward in various models of the longitudinal structure of the initial state [121, 122]. By careful inspection of individual flux tubes in Fig. 3.12 one also observes longitudinal fluctuations, albeit the amplitude of the longitudinal variations is significantly smaller compared to the variations in the transverse plane.

Now in order to further analyze the longitudinal fluctuations, we consider the rapidity profiles of the transverse pressure $\langle P_T(\tau, \eta) \rangle_\perp$ averaged over the transverse plane. In Fig. 3.13 we show the ratio of $\langle P_T(\tau, \eta) \rangle_\perp$ relative to its value $\langle P_T(\tau, \eta = 0) \rangle_\perp$ at mid-rapidity at $\tau \simeq 0.75$ fm/c for head-on Au+Au collisions at two different
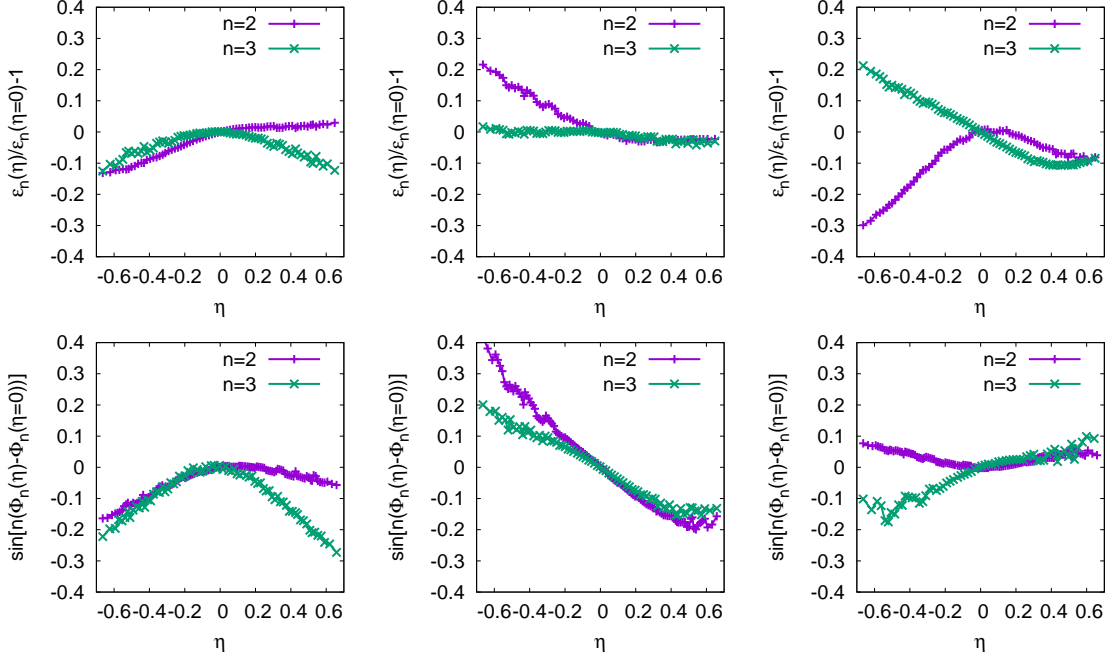
Figure 3.14: Change in eccentricity relative to value at mid rapidity (top) and corresponding alteration in event plane angle (bottom) as a function of rapidity for three different events of head-on Au-Au collision at $\sqrt{s} = 130$ GeV

energies $\sqrt{s_{NN}} = 130$, 200 GeV in the left and right panels. Different curves in each panel correspond to the results for five individual events (labeled as Seed 0-4), along with the symmetrized average over all events. Generally, the fluctuations in the accessible rapidity window $-0.6 < \eta < 0.6$ are relatively small $\lesssim 1\%$, and appear to decrease with increasing center of mass energy, as the longitudinal profile gets stretched out over a larger rapidity range. It is also interesting to observe that the dominant fluctuation in individual events around mid-rapidity appears to be a forward/backward asymmetry.

As the fluctuation in the initial state and corresponding initial energy deposition maps to the anisotropy in azimuthal distribution of final state particle. We characterize this asymmetry in the event geometry using n-th order spatial eccentricity

$$\boldsymbol{\epsilon}_n(\eta) = \epsilon_n(\eta)e^{in\Phi_n} = \frac{\int dr^2 \varepsilon(r,\phi,\eta)r^n e^{in\phi}}{\int dr^2 \varepsilon(r,\phi,\eta)r^n} \tag{3.54}$$

where $\phi = \tan^{-1}(y/x)$ is the azimuthal angle and ε is the energy density approximated in terms of $T^{\tau\tau}$. We demonstrate how geometry varies on event-by-event basis by presenting eccentricity relative to its value at mid-rapidity and corresponding al-
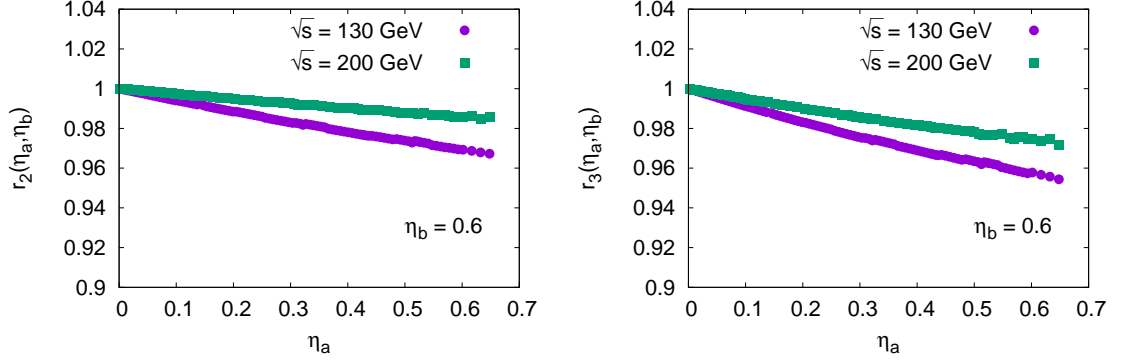
Figure 3.15: The factorization ratio $r_2(\eta_a, \eta_b)$ (left) and $r_3(\eta_a, \eta_b)$ (right) obtained from initial spatial eccentricity as a function of rapidity for central Au-Au collision

teration in the event plane angle Φ_n, expressed as $\sin\left[n(\Phi_n(\eta) - \Phi_n(0))\right]$, for three randomly chosen events of Au-Au collision at $\sqrt{s} = 130$ GeV. It is clear from the top panel of Fig. 3.14 that ϵ_2 and ϵ_3 do not follow a certain trend and may increase (decrease) together or separately. Similarly one sees a distinguishable variation in the event plane angle which is related to the fact that different nucleons controls energy deposition at different rapidity and therefore the measured twist may or may not change monotonically as shown in the bottom panel of Fig. 3.14.

The variation in event plane angle from particle to particle leads to breakdown of factorization relation $V_n^{ab} = v_n^a v_n^b$, where V_n^{ab} is the Fourier coefficient (anisotropic flow) obtained from two particle correlation function of a pair of particle a and b with Fourier coefficient v_a and v_b respectively [24, 123]. This decorrelation of the anisotropic flow in the forward and backward direction is characterised using initial state $\boldsymbol{\epsilon_n}$ as

$$r_n(\eta_a, \eta_b) = \frac{\left\langle \mathrm{Re}[\boldsymbol{\epsilon}_\mathrm{n}(-\eta_\mathrm{a}).\boldsymbol{\epsilon}_\mathrm{n}^*(\eta_\mathrm{b})]\right\rangle}{\left\langle \mathrm{Re}[\boldsymbol{\epsilon}_\mathrm{n}(\eta_\mathrm{a}).\boldsymbol{\epsilon}_\mathrm{n}^*(\eta_\mathrm{b})]\right\rangle} \qquad (3.55)$$

where $\langle\rangle$ denotes the average over different configurations. The results for central Au-Au collision for two different center of mass energies: 130 and 200 GeV is shown in Fig. 3.15 with $\eta_b = 0.6$ We find that the factorization ratio is less than unity, meaning that the correlation is stronger in the forward direction, as already seen in the experiments [24, 25]. The stronger decorrelation at lower center of mass energies is in agreement with the previous result Fig. 3.13 where strength of fluctuation ceases

with the increase of collision energy. It would be interesting to extend this analysis to larger rapidities and to other centrality classes. However, the former would require simulations on significantly finer and larger lattices, and is therefore beyond the scope of the present work.

3.4 Closing Remarks

We developed a framework to perform $3+1$D simulations of initial energy deposition in heavy-ion collision based on the effective theory of CGC, which takes the finite longitudinal extent of the colliding nuclei into account. Based on a simple model of the color charge distribution, we investigated the detailed dynamics, during and shortly after the collision. While in low energy collisions, where the longitudinal extent of the incoming nuclei $Q_s R_\gamma$ is non-negligible, significant violations of boost invariance can be observed, the results smoothly approach the boost invariant limit [87, 92] at high energies where the longitudinal thickness $Q_s R_\gamma \to 0$ becomes sufficiently small.

Subsequently, we developed a more elaborate model of the three dimensional color charge distribution in a large nucleus, where the large scale structure of the nucleus is determined by the longitudinal and transverse positions of nucleons, while small scale fluctuations in the longitudinal and transverse directions are determined by the x and $\mathbf{k}_\perp$ dependence of transverse momentum dependent parton distributions. Based on this model, we obtained first results regarding the three dimensional structure and its fluctuations at two different center of mass energies, which show encouraging trends e.g. the longitudinal rapidity profiles and fluctuations appear to become stretched with increasing center of mass energy, which was not necessarily the case in a previous attempt to generalize the IP-Glasma initial state to $3 + 1$ dimensions [41]. We also used this model to study the decorrelation of the initial spatial eccentricity, which is consistent with the experimental observation.

Due to the significant computational cost of performing $3 + 1$D classical Yang-Mills simulations of the space-time dynamics our numerical results have so far been limited to the central rapidity window for a few head-on collisions, and it would certainly be interesting to extend the analysis to larger rapidities and higher center of mass

energies and perform a more systematic study of the various effects as a function of the centrality of the events. Evidently, to make contact with experimental observations, such phenomenological studies should be performed within the physical $SU(3)$ gauge group of QCD, where the formalism developed within this thesis can be applied in exactly the same way, albeit further increasing the computational cost of the simulations. Beyond the improvement of numerical simulations (see also [47]), it would also be important to develop further analytical insights into the $3+1$ D space-time evolution of the Glasma, which could e.g. be obtained by analyzing the perturbative dilute limit along the lines of [124].

Another interesting problem could be studying the production of quark-antiquark pairs from classical 3+1 D Yang-Mills field. By coupling Dirac equation to the background Glasma field, one can study the dynamics of fermions, which can help us in understanding the chemical thermalization in the pre-equilibrium. Although one can obtain analytical results for dilute-dense collision [125, 126] but revisiting this problem with a fully non-perturbative 3+1 D solution will lead to interesting phenomenological applications [127, 128]

Chapter 4

An Analytical study towards dilute 3D Glasma

In the last chapter we developed a framework to solve the 3+1 D classical Yang-Mills equation and leveraged it to study the longitudinal dynamics of the fireball. Even though the numerical scheme is free from any numerical instabilities but huge computational cost hinders us from examining the transverse dynamics for the physical $SU(3)$ gauge group of QCD. In this chapter we present an analytical approach to gain further insight from the overlapping region of the colliding nuclei. We start by setting up the the formalism in Section 4.1 by assuming perturbation on top of the background fields. In Section 4.2, we obtain analytic expressions for the color fields produced in the forward light cone by using a dummy field approach. We then employ a simple model of nuclear collision geometry to derive an analytic expression for transverse pressure in Section 4.3 and extend it to compare our results to 3+1D classical Yang-Mills simulation in Section 4.4

4.1 General formalism

In order to recapitulate, we quickly go over the fields and color currents of the incoming nuclei prior to the collision in the CGC framework. Using light cone coordinates $x^{\pm} = (x^0 \pm x^3)/\sqrt{2}$, the color current of a nucleus moving along x^+ (denoted as "A") is given by

$$\mathcal{J}_A^{\mu}(x^+, \mathbf{x}_{\perp}) = \delta_-^{\mu} \rho_A^a(x^+, \mathbf{x}_{\perp}) t^a, \tag{4.1}$$

where $\mathbf{x}_\perp = (x^1, x^2)$ are transverse coordinates and t^a are the generators of the gauge group. Within the CGC framework, the color current depends only on one of the two light cone coordinates (in this case x^+) due to static nature of the large-x partons. The color field $\mathcal{A}^\mu$ sourced by Eq. (4.1) is a solution to the Yang-Mills equations

$$\mathcal{D}_\mu \mathcal{F}^{\mu\nu}(x^+, x^-, \mathbf{x}_\perp) = \mathcal{J}_A^\nu(x^+, \mathbf{x}_\perp), \tag{4.2}$$

with the gauge covariant derivative

$$\mathcal{D}_\mu \mathcal{F}^{\mu\nu} = \partial_\mu \mathcal{F}^{\mu\nu} - ig\left[\mathcal{A}_\mu, \mathcal{F}^{\mu\nu}\right], \tag{4.3}$$

and the non-Abelian field strength tensor given by

$$\mathcal{F}^{\mu\nu} = \partial^\mu \mathcal{A}^\nu - \partial^\nu \mathcal{A}^\mu - ig\left[\mathcal{A}^\mu, \mathcal{A}^\nu\right]. \tag{4.4}$$

Using appropriate boundary conditions in the asymptotic past $x^0 \to -\infty$, the solution to Eq. (4.2) in covariant gauge $\partial_\mu \mathcal{A}^\mu = 0$ is given as

$$\mathcal{A}^-(x^+, \mathbf{x}_\perp) = \phi_A(x^+, \mathbf{x}_\perp) = -(\nabla_\perp^2)^{-1}\rho_A(x^+, \mathbf{x}_\perp), \tag{4.5}$$

with all other components of $\mathcal{A}^\mu$ vanishing. The current and color field in Eqs. (4.1) and (4.5) solve the gauge covariant continuity equation

$$\mathcal{D}_\mu \mathcal{J}^\mu(x) = 0. \tag{4.6}$$

Similarly, we can consider a nucleus moving along x^- (denoted as "B") with the analogous current and color field

$$\mathcal{J}_B^\mu(x^-, \mathbf{x}_\perp) = \delta_+^\mu \rho_B^a(x^-, \mathbf{x}_\perp)t^a, \tag{4.7}$$

$$\mathcal{A}^+(x^-, \mathbf{x}_\perp) = \phi_B(x^-, \mathbf{x}_\perp) = -(\nabla_\perp^2)^{-1}\rho_B(x^-, \mathbf{x}_\perp). \tag{4.8}$$

Now, in order to describe the collision of the incoming nuclei in the forward light-cone, we need to solve the following equations

$$\mathcal{D}_\mu \mathcal{F}^{\mu\nu}(x) = \mathcal{J}_A^\mu(x) + \mathcal{J}_B^\mu(x), \tag{4.9}$$

$$\mathcal{D}_\mu \mathcal{J}_A^\mu(x) = 0, \tag{4.10}$$

$$\mathcal{D}_\mu \mathcal{J}_B^\mu(x) = 0, \tag{4.11}$$

with initial conditions specified in the asymptotic past as

$$\lim_{x^0 \to -\infty} \mathcal{A}^\mu(x) = \delta_-^\mu \, \phi_A(x^+, \mathbf{x}_\perp) + \delta_+^\mu \, \phi_B(x^-, \mathbf{x}_\perp), \tag{4.12}$$

$$\lim_{x^0 \to -\infty} \mathcal{J}_A^\mu(x) = \delta_-^\mu \rho_A(x^+, \mathbf{x}_\perp), \tag{4.13}$$

$$\lim_{x^0 \to -\infty} \mathcal{J}_B^\mu(x) = \delta_+^\mu \rho_B(x^-, \mathbf{x}_\perp). \tag{4.14}$$

In general, there are no closed form solutions for Eq. (4.9). However, in the ultra-relativistic limit where the nuclei becomes infinitesimally thin,

$$\rho_{(A,B)}(x^\pm, \mathbf{x}_\perp) \simeq \delta(x^\pm)\tilde{\rho}_{(A,B)}(\mathbf{x}_\perp), \tag{4.15}$$

the solution to Eq. (4.9) is invariant under boosts along $z = x^3$ and a partial analytical solution is feasible. In this case one can determine the Glasma initial conditions on the boundary of the light-cone ($x^+ > 0$ with $x^- = 0$ or $x^- > 0$ with $x^+ = 0$) [86] which due to boost-invariance are naturally expressed in proper time $\tau = \sqrt{2x^+ x^-}$ and space-time rapidity $\eta = 1/2 \ln(x^+/x^-)$ coordinates. The solution at $\tau = 0^+$ in the temporal axial gauge ($\mathcal{A}^\tau = 0$) takes the form

$$\mathcal{A}^i(\tau = 0^+, \mathbf{x}_\perp) = \alpha_A^i(\mathbf{x}_\perp) + \alpha_B^i(\mathbf{x}_\perp), \tag{4.16}$$

$$\mathcal{A}^\eta(\tau = 0^+, \mathbf{x}_\perp) = \frac{ig}{2}\left[\alpha_A^i(\mathbf{x}_\perp), \alpha_B^i(\mathbf{x}_\perp)\right], \tag{4.17}$$

where the color fields $\alpha_{(A,B)}^i$

$$\alpha_{(A,B)}^i(\mathbf{x}_\perp) = \frac{1}{ig}V_{(A,B)}(\mathbf{x}_\perp)\partial^i V_{(A,B)}^\dagger(\mathbf{x}_\perp), \tag{4.18}$$

are expressed in terms of light-like Wilson lines

$$V_A^\dagger(\mathbf{x}_\perp) = \lim_{x^+ \to \infty} \mathcal{P} \exp\left(ig \int_{-\infty}^{x^+} dx'^+ \phi_A(x'^+, \mathbf{x}_\perp)\right), \tag{4.19}$$

$$V_B^\dagger(\mathbf{x}_\perp) = \lim_{x^- \to \infty} \mathcal{P} \exp\left(ig \int_{-\infty}^{x^-} dx'^- \phi_B(x'^-, \mathbf{x}_\perp)\right). \tag{4.20}$$

Using equations (4.16) and (4.17) as the initial condition, the solution at late times $\tau > 0$ is either obtained perturbatively, by expanding in proper time τ [32–35] or numerically using real time lattice simulations [18, 28, 92].

Now, in order to model collisions at finite energy it is necessary to go beyond the boost invariant approximation given by Eq. (4.15) and allow for more general color charge densities $\rho_{(A,B)}(x^\pm, \mathbf{x}_\perp)$ which exhibit a non-trivial dependence on the light cone coordinates. Even though a fully non-perturbative numerical solution was obtained in the previous chapter, going beyond certain rapidity window or including LHC energy turned out to highly technical. In this chapter, we derive the semi-analytical results for Eqs. (4.9) – (4.11) using the weak field approximation which allows us to construct the solution perturbatively in powers of $\rho_{(A,B)}(x^\pm, \mathbf{x}_\perp)$

$$A^\mu(x) = \mathcal{A}^\mu(x) + a^\mu(x), \tag{4.21}$$

$$J^\mu(x) = \mathcal{J}^\mu(x) + j^\mu(x), \tag{4.22}$$

where the background fields $\mathcal{A}^\mu = \mathcal{O}(\rho)$ and background currents $\mathcal{J}^\mu = \mathcal{O}(\rho)$ are given by the single nuclei solutions Eqs. (4.1), (4.5) and Eqs. (4.7), (4.8). The perturbative fields a^μ and j^μ capture all higher order corrections $\mathcal{O}(\rho^n)$ with $n > 1$: the color field a^μ describes the (dilute) Glasma itself, while the currents j^μ represent perturbations of the color currents of the nuclei, $\mathcal{J}_A^\mu$ and $\mathcal{J}_B^\mu$, due to non-Abelian color rotation. Expanding to quadratic order in the color charge densities, the background field equations read

$$\partial_\mu \mathcal{F}^{\mu\nu}(x) = \mathcal{J}^\nu(x), \tag{4.23}$$

$$\partial_\mu \mathcal{J}^\mu(x) = 0, \tag{4.24}$$

while the perturbative field equations read

$$\partial_\mu f^{\mu\nu}(x) = j^\nu(x) + ig\,\partial_\mu\left[\mathcal{A}^\mu(x), \mathcal{A}^\nu(x)\right] + ig\left[\mathcal{A}_\mu(x), \partial^\mu \mathcal{A}^\nu(x) - \partial^\mu \mathcal{A}^\mu(x)\right], \quad (4.25)$$

$$\partial_\mu j^\mu(x) = +ig\left[\mathcal{A}_\mu(x), \mathcal{J}^\mu(x)\right], \quad (4.26)$$

with the perturbative field strength tensor

$$f^{\mu\nu}(x) = \partial^\mu a^\nu(x) - \partial^\nu a^\mu(x). \quad (4.27)$$

Since the perturbations accounts for the Glasma created during the collision of the two nuclei, we assume that both perturbative fields and currents vanish in the asymptotic past

$$\lim_{x^0 \to -\infty} a^\mu(x) = 0, \quad (4.28)$$

$$\lim_{x^0 \to -\infty} j^\mu(x) = 0. \quad (4.29)$$

Assuming that the color charges of the colliding nuclei do not change their trajectories and considering the initial conditions in Eq. (4.29), the solution to Eq. (4.26) is straight-forward:

$$j^+(x^+, x^-, \mathbf{x}_\perp) = ig \int_{-\infty}^{x^+} dz^+ \left[\phi_A(z^+, \mathbf{x}_\perp), \rho_B(x^-, \mathbf{x}_\perp)\right], \quad (4.30)$$

$$j^-(x^+, x^-, \mathbf{x}_\perp) = ig \int_{-\infty}^{x^-} dz^- \left[\phi_B(z^-, \mathbf{x}_\perp), \rho_A(x^+, \mathbf{x}_\perp)\right]. \quad (4.31)$$

In covariant gauge, $\partial_\mu a^\mu = 0$, Eq. (4.25) simplifies to

$$\partial^2 a^\mu(x) = S^\mu(x), \quad (4.32)$$

where $S^\mu(x)$ are a-independent source terms given by

$$S^+(x^+, x^-, \mathbf{x}_\perp) = +ig\Big(\partial_- \big[\phi_A(x^+, \mathbf{x}_\perp), \phi_B(x^-, \mathbf{x}_\perp)\big] + \int\limits_+ \big[\phi_A(x^+, \mathbf{x}_\perp), \rho_B(x^-, \mathbf{x}_\perp)\big]\Big),$$

(4.33)

$$S^-(x^+, x^-, \mathbf{x}_\perp) = -ig\Big(\partial_+ \big[\phi_A(x^+, \mathbf{x}_\perp), \phi_B(x^-, \mathbf{x}_\perp)\big] + \int\limits_- \big[\rho_A(x^+, \mathbf{x}_\perp), \phi_B(x^-, \mathbf{x}_\perp)\big]\Big),$$

(4.34)

$$S^i(x^+, x^-, \mathbf{x}_\perp) = -ig\Big(\big[\phi_A(x^+, \mathbf{x}_\perp), \partial^i\phi_B(x^-, \mathbf{x}_\perp)\big] - \big[\partial^i\phi_A(x^+, \mathbf{x}_\perp), \phi_B(x^-, \mathbf{x}_\perp)\big]\Big).$$

(4.35)

For future convenience, we are introducing a shorthand notation

$$\int\limits_\pm f(x^\pm) \equiv \int\limits_{-\infty}^{x^\pm} dz^\pm f(z^\pm).$$

(4.36)

We emphasise that the choice of covariant gauge provides us an independent solution for the different components of a^μ in Eq. (4.32). Analyzing the $x^\pm$ dependence of the source terms in Eqs. (4.33) – (4.34), we find that $S^\pm(x)$ are only non-zero along the boundaries of the future light-cone, whereas $S^i(x)$ only has support in vicinity of the collision center $x^+ = x^- = 0$. Requiring causality and appropriate initial conditions given by Eq. (4.28), we can formally solve the field equations in Eq. (4.32) using

$$a^\mu(x) = \int\limits_y G(x - y)S^\mu(y),$$

(4.37)

with the retarded propagator given by

$$G(z) = -\frac{1}{2\pi}\Theta(z^0)\delta(z^\mu z_\mu).$$

(4.38)

4.2 Dummy field approach for $3 + 1$D Yang-Mills

Even though the above equations are quite neat, the convolution of the Green's function with the source terms is quite non-trivial and therefore we introduce a

comprehensible way to solve these equations analytically. To begin with, we recast the source terms in Eqs. (4.33) – (4.35) as

$$S^+(x) = \int_{p_\perp} \int_{q_\perp} \left(+\frac{\partial}{\partial x^-} + q_\perp^2 \int_{x^+} \right) \left(-gf^{abc}t^c \tilde{\phi}_A^a(x^+, p_\perp) \tilde{\phi}_B^b(x^-, q_\perp) \right) e^{-i(p+q)_\perp \cdot x_\perp} \quad (4.39)$$

$$S^-(x) = \int_{p_\perp} \int_{q_\perp} \left(-\frac{\partial}{\partial x^+} - p_\perp^2 \int_{x^-} \right) \left(-gf^{abc}t^c \tilde{\phi}_A^a(x^+, p_\perp) \tilde{\phi}_B^b(x^-, q_\perp) \right) e^{-i(p+q)_\perp \cdot x_\perp}$$

$$\quad (4.40)$$

$$S^i(x) = +\int_{p_\perp} \int_{q_\perp} i(p^i - q^i) \left(-gf^{abc}t^c \tilde{\phi}_A^a(x^+, p_\perp) \tilde{\phi}_B^b(x^-, q_\perp) \right) e^{-i(p+q)_\perp \cdot x_\perp} \quad (4.41)$$

where $\int_{p_\perp} = \int \frac{d^2 p_\perp}{(2\pi)^2}$ and define a dummy source

$$S_d(x^+, x^-, p_\perp, q_\perp) = -gf^{abc}t^c \tilde{\phi}_A^a(x^+, p_\perp) \tilde{\phi}_B^b(x^-, q_\perp) \quad (4.42)$$

such that the expression for the source terms simplifies to

$$S^+(x) = \int_{p_\perp} \int_{q_\perp} \left(\frac{\partial}{\partial x^-} + q_\perp^2 \int_{x^+} \right) S_d(x^+, x^-, p_\perp, q_\perp) e^{-i(p+q)_\perp \cdot x_\perp}, \quad (4.43)$$

$$S^-(x) = \int_{p_\perp} \int_{q_\perp} \left(-\frac{\partial}{\partial x^+} - p_\perp^2 \int_{x^-} \right) S_d(x^+, x^-, p_\perp, q_\perp) e^{-i(p+q)_\perp \cdot x_\perp}, \quad (4.44)$$

$$S^i(x) = \int_{p_\perp} \int_{q_\perp} i(q^i - p^i) S_d(x^+, x^-, p_\perp, q_\perp) e^{-i(p+q)_\perp \cdot x_\perp}. \quad (4.45)$$

Now, using the general form of Eq. (4.37), the solution for the transverse gauge field is given by

$$a^i(x) = \int_y G(x - y) S^i(y)$$

$$= \int dy^+ dy^- \int_{y_\perp} G(x - y) \int_{p_\perp} \int_{q_\perp} i(p^i - q^i) S_d(y^+, y^-, p_\perp, q_\perp) e^{-i(p+q)_\perp \cdot y_\perp}$$

$$= \int dy^+ dy^- \int_{p_\perp} \int_{q_\perp} i(p^i - q^i) S_d(y^+, y^-, p_\perp, q_\perp) \int_{y_\perp} G(x - y) e^{-i(p+q)_\perp \cdot y_\perp}. \quad (4.46)$$

Using the redefinition $z^\mu = x^\mu - y^\mu$ we can solve the integral over $y_\perp$:

$$\int_{y_\perp} G(x-y)e^{-i(p+q)_\perp \cdot y_\perp} = -e^{-i(p+q)_\perp \cdot x_\perp} \int_0^\infty d\rho\rho \int_0^{2\pi} d\theta \frac{1}{2\pi}\Theta(z)\delta(2z^+z^- - \rho^2)e^{-i|p+q|\rho\cos\theta}$$

$$= -e^{-i(p+q)_\perp \cdot x_\perp}\Theta(z^0)\int_0^\infty d\rho\rho\,\delta(2z^+z^- - \rho^2)J_0(|p+q|\rho)$$

$$= -\frac{1}{2}\Theta(z^0)\Theta(\tau)J_0(|p+q|\sqrt{2z^+z^-})e^{-i(p+q)_\perp \cdot x_\perp}, \qquad (4.47)$$

where $\rho = |z_\perp|$ and $|p+q| = |(p+q)_\perp|$. The two Heaviside functions imply that this integral is only non-vanishing in the forward light cone. On inserting this result into Eq. (4.46), we get

$$a^i(x) = -\frac{1}{2}\int_{p_\perp}\int_{q_\perp} i(p^i - q^i)\int_0^\infty dz^+ \int_0^\infty dz^- S_d(x^+ - z^+, x^- - z^-, p_\perp, q_\perp)\times$$

$$J_0(|p+q|\sqrt{2z^+z^-})e^{-i(p+q)_\perp \cdot x_\perp} \qquad (4.48)$$

Similarly, the solution for light-cone gauge fields can be given as

$$a^+(x) = -\frac{1}{2}\int_{p_\perp}\int_{q_\perp}\left(+\frac{\partial}{\partial x^-} + q_\perp^2\int_{x^+}\right)\int_0^\infty dz^+ \int_0^\infty dz^- S_d(x^+ - z^+, x^- - z^-, p_\perp, q_\perp)\times$$

$$J_0(|p+q|\sqrt{2z^+z^-})e^{-i(p+q)_\perp \cdot x_\perp}, \qquad (4.49)$$

$$a^-(x) = -\frac{1}{2}\int_{p_\perp}\int_{q_\perp}\left(-\frac{\partial}{\partial x^+} - p_\perp^2\int_{x^-}\right)\int_0^\infty dz^+ \int_0^\infty dz^- S_d(x^+ - z^+, x^- - z^-, p_\perp, q_\perp)\times$$

$$J_0(|p+q|\sqrt{2z^+z^-})e^{-i(p+q)_\perp \cdot x_\perp}. \qquad (4.50)$$

In regards to the dummy source, we define the dummy fields

$$a_d(x^+, x^-, p_\perp, q_\perp) = \frac{g}{2}\int_0^\infty dz^+ \int_0^\infty dz^- f_{abc}t^c\tilde{\phi}_A^a(x^+ - z^+, p_\perp)\tilde{\phi}_B^b(x^- - z^-, q_\perp)\times$$

$$J_0(|p+q|\sqrt{2z^+z^-}) \qquad (4.51)$$

which shortens the expression for the gauge fields to

$$a^i(x) = \int\limits_{p_\perp} \int\limits_{q_\perp} i(p^i - q^i) a_d(x^+, x^-, p_\perp, q_\perp) e^{-i(p+q)_\perp \cdot x_\perp}, \tag{4.52}$$

$$a^+(x) = \int\limits_{p_\perp} \int\limits_{q_\perp} \left(+ \frac{\partial}{\partial x^-} + q_\perp^2 \int\limits_{x^+} \right) a_d(x^+, x^-, p_\perp, q_\perp) e^{-i(p+q)_\perp \cdot x_\perp}, \tag{4.53}$$

$$a^-(x) = \int\limits_{p_\perp} \int\limits_{q_\perp} \left(- \frac{\partial}{\partial x^+} - p_\perp^2 \int\limits_{x^-} \right) a_d(x^+, x^-, p_\perp, q_\perp) e^{-i(p+q)_\perp \cdot x_\perp}. \tag{4.54}$$

We can further simplify the expressions for $a^\pm$ by explicitly carrying out the integration and derivative on the dummy fields in (4.53) and (4.54). Starting with the derivative term in Eq. (4.53), we use integration by parts to find

$$\partial_-^{(x)} a_d(x^+, x^-, p_\perp, q_\perp) = \frac{g}{2} f_{abc} t^c \int\limits_0^\infty dz^+ \int\limits_0^\infty dz^- \tilde{\phi}_A^a(x^+ - z^+, p_\perp) \tilde{\phi}_B^b(x^- - z^-, q_\perp) \times$$

$$\partial_-^{(z)} J_0(|p + q| \tau_z) + \frac{g}{2} f_{abc} t^c \int\limits_0^\infty dz^+ \tilde{\phi}_A^a(x^+ - z^+, p_\perp) \tilde{\phi}_B^b(x^-, q_\perp). \tag{4.55}$$

where $\tau_z = \sqrt{2z^+ z^-}$. The second term in the above equation is the boundary term for $z^- \to 0$, which is proportional to the color potential $\tilde{\phi}_B^b(x^-, q_\perp)$ that vanishes far inside the future light-cone. Using

$$\partial_\pm \tau_z = z^\mp / \tau_z, \tag{4.56}$$

$$\partial_\pm J_0(|p + q| \tau_z) = -J_1(|p + q| \tau_z) |p + q| \frac{z^\mp}{\tau_z}, \tag{4.57}$$

we find

$$\partial_-^{(x)} a_d(x^+, x^-, p_\perp, q_\perp) \simeq -\frac{g}{2} f_{abc} t^c \int\limits_0^\infty dz^+ \int\limits_0^\infty dz^- \tilde{\phi}_A^a(x^+ - z^+, p_\perp) \tilde{\phi}_B^b(x^- - z^-, q_\perp) \times$$

$$|p + q| \frac{z^+}{\tau_z} J_1(|p + q| \tau_z). \tag{4.58}$$

where we used $\simeq$ to denote that this expression is strictly valid inside the future light cone.

Now we can examine the term involving an integration in Eq. (4.53)

$$\int_{-\infty}^{x^+} d\tilde{x}^+ a_d(\tilde{x}^+, x^-, p_\perp, q_\perp) = \frac{g}{2} f_{abc} t^c \int_{-\infty}^{x^+} d\tilde{x}^+ \int_0^{+\infty} dz^+ \int_0^{+\infty} dz^- \tilde{\phi}_A^a(\tilde{x}^+ - z^+, p_\perp) \times$$

$$\tilde{\phi}_B^b(x^- - z^-, q_\perp) J_0(|p + q|\tau_z). \tag{4.59}$$

The integration over z^+ and $\tilde{x}^+$ can be re-arranged in the following way:

$$\int_0^{+\infty} dz^+ \int_{-\infty}^{x^+} d\tilde{x}^+ f(\tilde{x}^+ - z^+) g(z^+, z^-) = \int_0^{+\infty} dz^+ \int_{-\infty}^{x^+ - z^+} d\tilde{x}^+ f(\tilde{x}^+) g(z^+, z^-)$$

$$= \int_{-\infty}^{x^+} d\tilde{x}^+ f(\tilde{x}^+) \int_0^{x^+ - \tilde{x}^+} dz^+ g(z^+, z^-)$$

$$= \int_0^{+\infty} dz^+ f(x^+ - z^+) \int_0^{z^+} d\tilde{z}^+ g(\tilde{z}^+, z^-). \tag{4.60}$$

Equation (4.59) can therefore be written as

$$\int_{-\infty}^{x^+} d\tilde{x}^+ a_d(\tilde{x}^+, x^-, p_\perp, q_\perp) = \frac{g}{2} f_{abc} t^c \int_0^{+\infty} dz^+ \int_0^{+\infty} dz^- \tilde{\phi}_A^a(\tilde{x}^+ - z^+, p_\perp) \tilde{\phi}_B^b(x^- - z^-, q_\perp) \times$$

$$\int_0^{z^+} d\tilde{z}^+ J_0(|p + q|\sqrt{2\tilde{z}^+ z^-}). \tag{4.61}$$

The integral over the Bessel function

$$\int_0^{z^+} d\tilde{z}^+ J_0(|p + q|\sqrt{2\tilde{z}^+ z^-}) = \frac{1}{|p + q|} \frac{\tau_z}{z^-} J_1(|p + q|\tau_z), \tag{4.62}$$

leads to

$$\int_{-\infty}^{x^+} d\tilde{x}^+ a_d(\tilde{x}^+, x^-, p_\perp, q_\perp) = \frac{g}{2} f_{abc} t^c \int_0^{+\infty} dz^+ \int_0^{+\infty} dz^- \tilde{\phi}_A^a(\tilde{x}^+ - z^+, p_\perp) \tilde{\phi}_B^b(x^- - z^-, q_\perp) \times$$

$$\frac{1}{|p + q|} \frac{\tau_z}{z^-} J_1(|p + q|\tau_z). \tag{4.63}$$

Combining Eqs. (4.58) and (4.63) yields the required expression for a^+ field. One

can perform a similar calculation to obtain a related expression for a^- field. With this, we can write all the components of the gauge fields as:

$$a^+ \simeq \frac{g}{2} f_{abc} t^c \int_{p,q} \int_0^{+\infty} dz^+ dz^- \tilde{\phi}_A^a(\tilde{x}^+ - z^+, p_\perp) \tilde{\phi}_B^b(x^- - z^-, q_\perp) \left(-(p+q)_\perp^2 + 2q_\perp^2\right) \times$$

$$\frac{1}{|p+q|} \frac{z^+}{\tau_z} J_1(|p+q|\tau_z) e^{-i(p+q)\cdot x}, \tag{4.64}$$

$$a^- \simeq \frac{g}{2} f_{abc} t^c \int_{p,q} \int_0^{+\infty} dz^+ dz^- \tilde{\phi}_A^a(\tilde{x}^+ - z^+, p_\perp) \tilde{\phi}_B^b(x^- - z^-, q_\perp) \left(+(p+q)_\perp^2 - 2p_\perp^2\right) \times$$

$$\frac{1}{|p+q|} \frac{z^-}{\tau_z} J_1(|p+q|\tau_z) e^{-i(p+q)\cdot x} \tag{4.65}$$

$$a^i = \frac{g}{2} f_{abc} t^c \int_{p,q} i(p^i - q^i) \int_0^{+\infty} dz^+ \int_0^{+\infty} dz^- \tilde{\phi}_A^a(\tilde{x}^+ - z^+, p_\perp) \tilde{\phi}_B^b(x^- - z^-, q_\perp) \times$$

$$J_0(|p+q|\tau_z) e^{-i(p+q)\cdot x} \tag{4.66}$$

These are the fundamental results of our analytical calculation. At this stage, one can check that our gauge condition $\partial_\mu a^\mu = 0$, still holds. With these non-zero fields, we can now explore the space-time dynamics for different nuclear models.

4.3   Nuclear Model & Transverse Pressure

Using the above analytical calculation, the longitudinal structure of the Glasma at late times can be obtained by considering a model for the color charge distribution inside a nucleus. We assume a simple MV-like model given by

$$\left\langle \rho^a(x^+, x_\perp) \rho^b(x'^+, x'_\perp) \right\rangle = g^2 \mu^2 T_R(\frac{x^+ + x'^+}{2}) U_\epsilon(x^+ - x'^+) \delta^{ab} \delta^{(2)}(x_\perp - x'_\perp) \tag{4.67}$$

where the functions T and U are normalised Gaussian functions with width R and ϵ identified as the Lorentz contracted nuclear length and correlation length respectively. The constant μ is the MV model parameter which is related to saturation momentum Q_s via the relation $Q_s \propto g^2\mu$. In order to enforce color neutrality on average, one point function is assumed to be zero.

Based on the above model, we can now address a wide range of observables that would aid in the characterization of a dilute Glasma. In particular, it would be interesting

to consider the various components of the energy-momentum tensor which in the continuum limit takes the following form

$$
\begin{aligned}
T^{\mu\nu} &= -\mathcal{F}^{a,\mu\rho}\mathcal{F}^{a,\nu}{}_{\rho} + \frac{1}{4}g^{\mu\nu}\mathcal{F}^{a,\rho\sigma}\mathcal{F}^a_{\rho\sigma} \\
&= 2\operatorname{Tr}\Big[\underbrace{-f^{\mu\rho}f^{\nu}{}_{\rho} + \frac{1}{4}g^{\mu\nu}f^{\rho\sigma}f_{\rho\sigma}}_{\text{Perturbative}} \underbrace{- \big(F^{\mu\rho}f^{\nu}{}_{\rho} + f^{\mu\rho}F^{\nu}{}_{\rho}\big) + \frac{1}{2}g^{\mu\nu}f^{\rho\sigma}F_{\rho\sigma}}_{\text{Mixed Term}} \\
&\quad \underbrace{- F^{\mu\rho}F^{\nu}{}_{\rho} + \frac{1}{4}F^{\rho\sigma}F^{\rho\sigma}}_{\text{Background}} \Big]
\end{aligned}
\tag{4.68}
$$

However, for the purpose of this thesis, we will be considering the transverse pressure as it is solely generated during the collision and hence has no contribution from the background and the mixed part. The transverse pressure is given by

$$
p_T = \varepsilon_{E,L} + \varepsilon_{B,L}
\tag{4.69}
$$

where $\varepsilon_{E,L}$ and $\varepsilon_{B,L}$ are the longitudinal electric and longitudinal magnetic field given by

$$
\varepsilon_{E,L} = \left\langle \operatorname{Tr} f^2_{+-} \right\rangle
\tag{4.70}
$$

$$
\varepsilon_{B,L} = \frac{1}{2}\left\langle \operatorname{Tr} f^2_{ij} \right\rangle
\tag{4.71}
$$

Longitudinal Magnetic field

To get the longitudinal magnetic field, we first calculate the corresponding field strength f_{ij} with Eq. (4.52)

$$
f_{ij} = \partial_i a_j - \partial_j a_i = 2\int_{p,q} (q^i p^j - p^i q^j)a_d(x^+, x^-, p_\perp, q_\perp)e^{-i(p+q)_\perp \cdot x_\perp}.
\tag{4.72}
$$

The square of the above expression contains integrals over four color potentials, arising from the dummy fields. Since it is quite convenient to solve such integrals in Fourier space, we write the correlation function in Eq. (4.67) as

$$
\left\langle \rho^a(x^+, p_\perp)\rho^b(x'^+, q_\perp) \right\rangle = g^2\mu^2 T_R\big(\frac{x^+ + x'^+}{2}\big)U_\epsilon(x^+ - x'^+)\delta^{ab}\delta^{(2)}(p_\perp + q_\perp)
\tag{4.73}
$$

Exploiting the fact that the nuclear model is diagonal in momentum space we have

$$
\begin{aligned}
\varepsilon_{B,L} &= \frac{1}{2}\left\langle \mathrm{Tr}\, f_{ij}^2 \right\rangle \\
&= 4\int_{p,q}(p_\perp^2 q_\perp^2 - (p\cdot q)_\perp^2)\left\langle \mathrm{Tr}\left[a_d(x^+,x^-,p_\perp,q_\perp)a_d(x^+,x^-,-p_\perp,-q_\perp)\right]\right\rangle \\
&= \frac{g^2}{2}N_c(N_c^2-1)\int_{p,q}\int_{z^\pm}\int_{\bar z^\pm}(p_\perp^2 q_\perp^2 - (p\cdot q)_\perp^2)\left\langle \tilde\phi_A(x^+ - z^+,p_\perp)\tilde\phi_A(x^+ - \bar z^+,-p_\perp)\right\rangle \times \\
&\quad \left\langle \tilde\phi_B(x^- - z^-,q_\perp)\tilde\phi_B(x^- - \bar z^-,-q_\perp)\right\rangle J_0(|p+q|\tau_z)J_0(|p+q|\tau_{\bar z}) \\
&= \frac{g^2}{2}N_c(N_c^2-1)\int_{p,q}\int_{z^\pm}\int_{\bar z^\pm}J_0(|p+q|\tau_z)J_0(|p+q|\tau_{\bar z})(p_\perp^2 q_\perp^2 - (p\cdot q)_\perp^2)C_A(p_\perp)\times \\
&\quad C_B(q_\perp)T_A(x^+ - \frac{z^+ + \bar z^+}{2})T_B(x^- - \frac{z^- + \bar z^-}{2})U_A(\bar z^+ - z^+)U_B(\bar z^- - z^-)
\end{aligned}
$$

(4.74)

where we have used the shorthand notation $\int_{z^\pm}\int_{\bar z^\pm} = \int_0^\infty dz^+ \int_0^\infty dz^- \int_0^\infty d\bar z^+ \int_0^\infty d\bar z^-$ and evaluated the color structures as $f_{abc}f_{abc} = N_c(N_c^2 - 1)$. To obtain the last equality, we have used Eqs. (4.5) and (4.8), and replaced the gauge fields correlators with our nuclear model such that the overall transverse dependence is characterised by

$$
C(p_\perp) = \frac{g^2\mu^2}{(p_\perp^2 + m^2)^2}e^{-\frac{p_\perp^2}{\lambda^2}}.
$$

(4.75)

It is obvious from the Eq. (4.74) that one can perform a change of variables to average and difference coordinate, and since T and U are both Gaussian function, we can change the limits of integration to

$$
\int_0^\infty dz^+ \int_0^\infty dz^- \int_0^\infty d\bar z^+ \int_0^\infty d\bar z^- = \int_0^\infty dZ^+ \int_{-2Z^+}^{+2Z^+} d\delta z^+ \int_0^\infty dZ^- \int_{-2Z^-}^{+2Z^-} \delta dz^-
$$

(4.76)

The resultant expression for the longitudinal magnetic field is then given by

$$
\begin{aligned}
\varepsilon_{B,L} &= \frac{g^2}{2}N_c(N_c^2-1)\int_{p,q}\int_0^\infty dZ^+ \int_0^\infty dZ^- \int_{-2Z^+}^{+2Z^+} d\delta z^+ \int_{-2Z^-}^{+2Z^-} d\delta z^- \left(p_\perp^2 q_\perp^2 - (p\cdot q)_\perp^2\right) \times \\
&\quad C_A(p_\perp)C_B(q_\perp)T_A(x^+ - Z^+)T_B(x^- - Z^-)U_A(\delta z^+)U_B(\delta z^-) \times \\
&\quad J_0\Big(|p+q|\tau_z\Big)J_0\Big(|p+q|\tau_{\bar z}\Big)
\end{aligned}
$$

(4.77)

with $\tau_z = \sqrt{2(Z^+ + \delta z^+/2)(Z^- + \delta z^-/2)}$ and $\tau_{\bar{z}} = \sqrt{2(Z^+ - \delta z^+/2)(Z^- - \delta z^-/2)}$

Longitudinal Electric field

In order to calculate the longitudinal electric field, we start again with the calculation of the associated field strength f_{+-} by using Eqs. (4.53) and (4.54)

$$
\begin{aligned}
f_{+-} &= \partial_+ a^+ - \partial_- a^- \\
&= \int_{p,q} \Big(\underbrace{2\partial_+ \partial_- a_d(x^+, x^-, p_\perp, q_\perp)}_{Q} + (p_\perp^2 + q_\perp^2) a_d(x^+, x^-, p_\perp, q_\perp) \Big) e^{-i(p+q)_\perp \cdot x_\perp}
\end{aligned}
$$

$$(4.78)$$

Since we have already calculated the derivative of the dummy field in Eq. (4.58), we differentiate it again with respect to to x^+ to get the first term of the above expression (denoted by Q)

$$
\begin{aligned}
Q &\simeq -g f_{abc} t^c \int_0^\infty dz^+ \int_0^\infty dz^- \partial_+^{(x)} \tilde{\phi}_A^a(x^+ - z^+, p_\perp) \tilde{\phi}_B^b(x^- - z^-, q_\perp) |p+q| \frac{z^+}{\tau_z} J_1(|p+q|\tau_z) \\
&= -g f_{abc} t^c \int_0^\infty dz^+ \int_0^\infty dz^- \tilde{\phi}_A^a(x^+ - z^+, p_\perp) \tilde{\phi}_B^b(x^- - z^-, q_\perp) |p+q| \partial_+^{(z)} \left(\frac{z^+}{\tau_z} J_1(|p+q|\tau_z) \right) \\
&= -\frac{g}{2} f_{abc} t^c \int_0^\infty dz^+ \int_0^\infty dz^- \tilde{\phi}_A^a(x^+ - z^+, p_\perp) \tilde{\phi}_B^b(x^- - z^-, q_\perp) |p+q|^2 J_0(|p+q|\tau_z),
\end{aligned}
$$

$$(4.79)$$

The first approximation relates to the omission of boundary terms that are not relevant within the forward light-cone. To get the final equality, we used the Bessel identity

$$\frac{2}{x} J_1(x) = J_0(x) + J_2(x).$$

$$(4.80)$$

The field strength in Eq. (4.78) is then obtained by summing (4.79) with the expanded form of dummy field

$$f_{+-} = -g f_{abc} t^c \int_{p,q} \int_0^\infty dz^+ \int_0^\infty dz^- \tilde{\phi}_A^a(x^+ - z^+, p_\perp) \tilde{\phi}_B^b(x^- - z^-, q_\perp) (p \cdot q)_\perp J_0(|p+q|\tau_z).$$

$$(4.81)$$

Dilute	3+1D CYM [1]	3+1D CPIC [113]
$g^2\mu$	$\frac{g^2\bar{\mu}}{\sqrt{2}}$	$g^2\mu$
R	$\frac{R_\gamma}{2}$	$\frac{R_\gamma}{2}$
m/Λ	m/Λ	m/Λ

Table 4.1: Parameters for comparing (semi-)analytical results with $3+1$ D simulations

With this, the expression for the longitudinal electric field takes the following form

$$
\begin{aligned}
\varepsilon_{E,L} &= \left\langle \mathrm{Tr}\left[f_{+-}^2\right]\right\rangle \\
&= \frac{g^2}{2}N_c(N_c^2-1)\int\limits_{p,q}\int\limits_{z^\pm}\int\limits_{\bar{z}^\pm}\left\langle\tilde{\phi}_A(x^+-z^+,p_\perp)\tilde{\phi}_A(x^+-\bar{z}^+,-p_\perp)\right\rangle \times \\
&\quad \left\langle\tilde{\phi}_B(x^--z^-,q_\perp)\tilde{\phi}_B(x^--\bar{z}^-,-q_\perp)\right\rangle(p\cdot q)_\perp^2 J_0(|p+q|\tau_z)J_0(|p+q|\tau_{\bar{z}}) \\
&= \frac{g^2}{2}N_c(N_c^2-1)\int\limits_{p,q}\int\limits_0^\infty dZ^+\int\limits_0^\infty dZ^-\int\limits_{-2Z^+}^{+2Z^+}d\delta z^+\int\limits_{-2Z^-}^{+2Z^-}d\delta z^-(p\cdot q)_\perp^2 C_A(p_\perp)C_B(q_\perp)\times \\
&\quad J_0(|p+q|\tau_z)J_0(|p+q|\tau_{\bar{z}})T_A(x^+-Z^+)T_B(x^--Z^-)U_A(\delta z^+)U_B(\delta z^-).
\end{aligned}
$$

(4.82)

Using Eqs. (4.77) and (4.82), the resultant expression for the transverse pressure is given as

$$
\begin{aligned}
p_T &= \frac{g^2}{2}N_c(N_c^2-1)\int\limits_{p,q}\int\limits_0^\infty dZ^+\int\limits_0^\infty dZ^-\int\limits_{-2Z^+}^{+2Z^+}d\delta z^+\int\limits_{-2Z^-}^{+2Z^-}d\delta z^- p_\perp^2 q_\perp^2 C_A(p_\perp)C_B(q_\perp)\times \\
&\quad T_A(x^+-Z^+)T_B(x^--Z^-)U_A(\delta z^+)U_B(\delta z^-)J_0(|p+q|\tau_z)J_0(|p+q|\tau_{\bar{z}}).
\end{aligned}
$$

(4.83)

This is the main result of this chapter which shows the dependence of the transverse pressure on the longitudinal structure of the colliding nuclei. We also note that by regularising the color potential in the dummy sources (4.42) as $\phi_{A/B}(x^\pm,x)\equiv\delta(x^\pm)\phi_{A/B}(x_\perp)$, the result for $3+1$ D reduces to the result for $2+1$ D [86, 129, 130] (refer to Appendix B for more details)

$$
p_T = \frac{g^2}{2}N_c(N_c^2-1)\int\limits_{p,q}C_A(p_\perp)C_B(q_\perp)J_0^2(|p+q|\tau)p_\perp^2 q_\perp^2 \tag{4.84}
$$

4.4 Numerical results & comparisons to 3+1 D simulations

As the basic features of the reaction dynamics for $3 + 1$ D collisions have already been examined in detail using real time lattice simulation. Here we determine the effectiveness of our analytical calculation based on the weak-field approximations by comparing them with full 3+1 D simulations. In our $3 + 1$ D simulations, we defined the color charge density using $\rho^a(x, y, z) = \rho^{a(2D)}(x, y)T(z)$, which leads to a less general model given by

$$\left\langle \rho^a(z, x_\perp)\rho^b(z', x'_\perp) \right\rangle_{3D} = g^2 \underline{\mu}^2 \tilde{T}_{R_\gamma}(z)\tilde{T}_{R_\gamma}(z')\delta^{ab}\delta^{(2)}(x_\perp - x'_\perp) \tag{4.85}$$

Since the color charges are assumed to be x^- independent, we can write the above two-point function in light-cone coordinate system as

$$\left\langle \rho^a(x^+, x_\perp)\rho^b(x'^+, x'_\perp) \right\rangle_{3D} = g^2 \mu'^2 \tilde{T}_{R'}(x^+)\tilde{T}_{R'}(x'^+)\delta^{ab}\delta^{(2)}(x_\perp - x'_\perp), \tag{4.86}$$

where

$$\underline{\mu} = \sqrt{2}\mu' \tag{4.87}$$

$$R_\gamma = \sqrt{2}R' \tag{4.88}$$

Now on comparing Eqs. (4.67) and (4.86), we find that the correlators can be matched by equating the factorised longitudinal dependence as

$$\mu^2 T_R(\frac{x^+ + x'^+}{2})T_\epsilon(x^+ - x'^+) = \mu'^2 T_{R'}(x^+)T_{R'}(x'^+). \tag{4.89}$$

By multiplying the two Gaussians on the left, we find that for $\epsilon = 2R$, the cross terms cancel and then the resultant relations are given as

$$R = \frac{R_\gamma}{2} \tag{4.90}$$

$$\mu = \frac{\underline{\mu}}{\sqrt{2}} \tag{4.91}$$
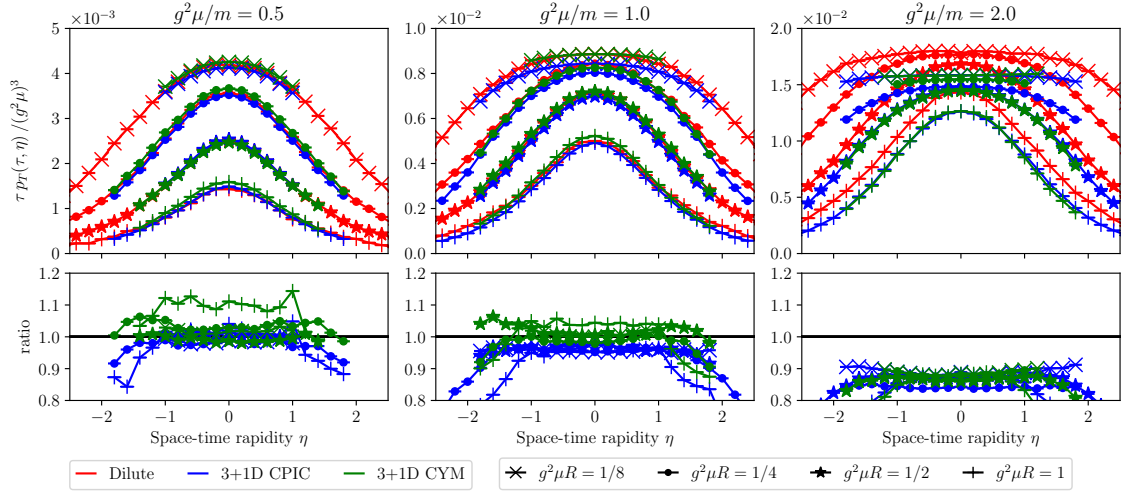
Figure 4.1: Transverse pressure as a function of rapidity for three different simulation parameters in the dilute limit: $g^2\mu/m = 0.5$ (left), $g^2\mu/m = 1.0$ (middle) and $g^2\mu/m = 2.0$ (right) compared to results from two different numerical schemes (3+1D CPIC [113] and 3+1D CYM [1]). In the dilute approximation, the transverse pressure is evaluated at $m\tau = 8$, while the 3+1D simulations are evaluated at $g^2\mu\tau = 1$ in the case of $g^2\mu R \in \{1/8, 1/4\}$ and $g^2\mu\tau = 2$ for $g^2\mu R \in \{1/2, 1\}$. The only exception is $g^2\mu R = 1$ and $g^2\mu/m = 2$, where we use $g^2\mu\tau = 2$. These plots were made by David Müller.

In Table 4.1, we have summarized the parameters for the analytical results obtained from Monte-Carlo integration (Dilute) and two different 3+1 D simulation schemes (3+1D CYM and 3+1D CPIC) with which we will determine the extent to which the results of our weak-field approximations agree with the fully non-perturbative real time lattice simulations.

We note that the non-linearity which measures the strength of diluteness of a model, can be controlled by the dimensionless ratio of the color charge density $g^2\mu$ and the infrared regulator m. We vary this dimensionless parameter and compare the transverse pressure as obtained from the analytical result and the result from 3+1 D simulations, for different longitudinal extent of the colliding nuclei in Fig. 4.1. The transverse discretization of the lattice in the two scheme were set to be same: $ma_\perp = 0.125$ and $ma_\perp N_\perp = 16$ with $m/\Lambda = 5$. Since the two simulation relies on completely different numerical schemes, the longitudinal discretization of the lattice is different, however in both cases, the discretization is chosen such that the nucleus is properly
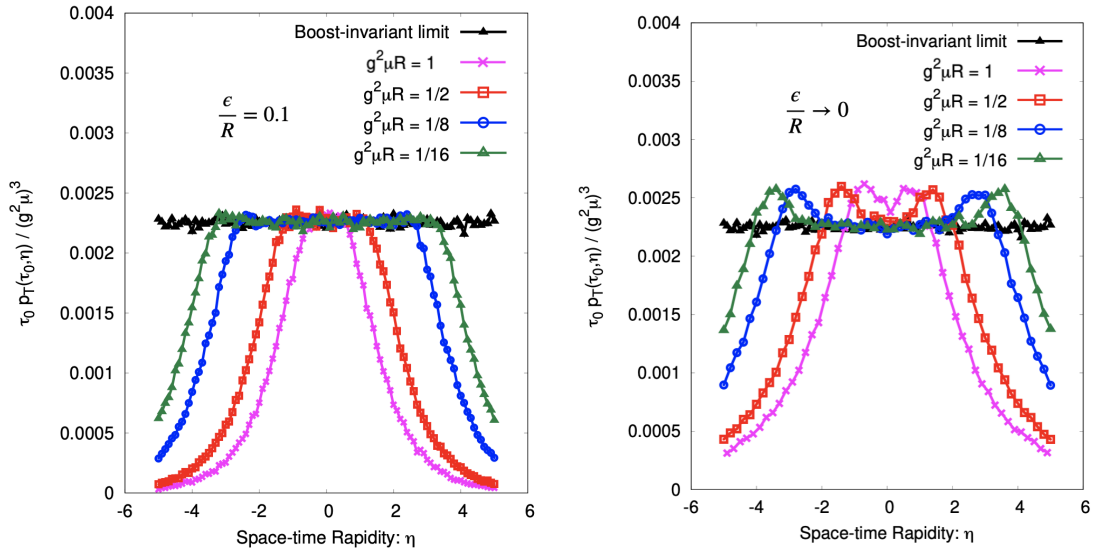
Figure 4.2: Transverse pressure corresponding to two different limits of coherence length: $\epsilon/R = 0.1$ (left) and $\epsilon/R \to 0$ (right), for various thickness of the incoming nuclei.

resolved $R_\gamma/a_z \gg 1$, and the two nuclei propagate large enough after the collision i.e $N_z a_z \gg R_\gamma$.

Since, we are interested in late times where in the boost-invariant limit transverse pressure $\tau p_T(\tau)$ becomes independent of the proper-time τ, we scale the transverse pressure in Fig 4.1 with proper time τ. We primarily focus our attention on coherent color fields $\epsilon = 2R$ for which the nuclear model used for analytical calculations and simulations is identical. Before discussing the results of our weak field approximation, we emphasize that the results of two different $3 + 1$ D classical Yang mills implementations are in excellent agreement with each other. We find that, as per our expectation, the analytical calculation works remarkably well in the dilute limit $g^2\mu/m = 0.5$ as seen from the left panel of Fig. 4.1. By increasing the non-linearity of the model $g^2\mu/m \geq 1$, we find that the analytical results in the dilute limit overestimate the transverse pressure; nevertheless the rapidity profiles are still reproduced rather well and the flattening of the rapidity profiles with increasing $g^2\mu/m$ is correctly predicted by the (semi-)analytic calculation. It is further interesting to note that the ratio of the analytical to that of the simulation results are roughly the same for different thickness of the colliding nuclei, which suggests that the non-linearity could effectively be introduced by re-scaling the pressure profile. Besides the signi-
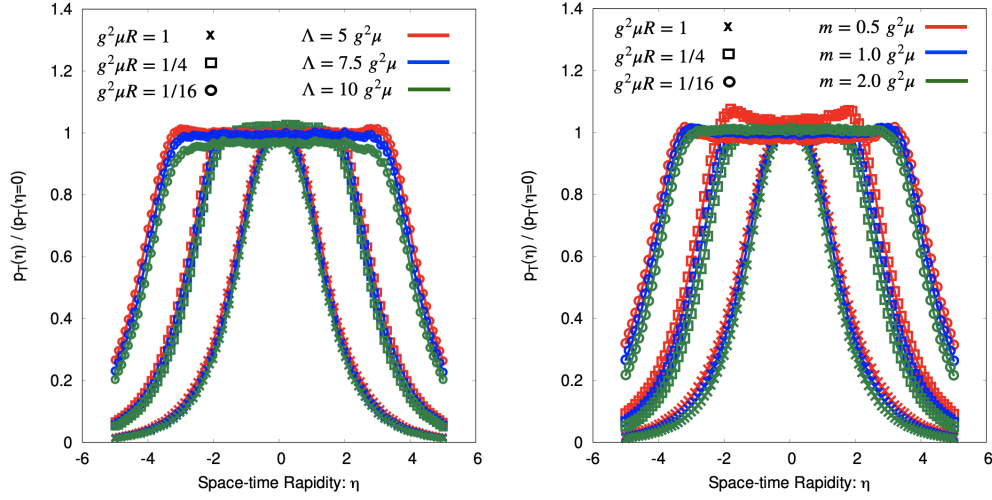
Figure 4.3: Transverse pressure relative to its value at mid-rapidity for different thickness of colliding nuclei along with fixed infrared regulator (left) and fixed UV regulator (right)

ficantly smaller computational cost, another enormous benefit of the semi-analytic calculation is that it is not bounded by lattice size and therefore can estimate result at larger rapidities, as is clearly visible from Fig. 4.1.

Now that we have established that our analytical results reproduces the full 3+1D numerical simulations in the dilute limit, we will further use it to consider the various limits of our nuclear model. We start by looking at the coherence length ϵ/R, which accounts for the randomness of color charges across a fixed longitudinal extent of the nucleus. Naturally, the longitudinal extent of the nucleus is greater than the longitudinal extent of color charge distribution and hence for a physical limit $\epsilon/R < 1$. In Fig 4.2, we plot the transverse pressure for different thicknesses of colliding nuclei while considering two different values of $\epsilon/R = 0.1$ (left panel) and $\epsilon/R \to 0$ (right panel) corresponding to the McLerran-Venugopalan (MV) model. We further include a comparsion of the results of the 3+1D dilute calculation, to the corresponding result in 2+1D boost-invariant limit, which is obtained by integrating Eq. 4.84. We observe that the curves in both the panels approach the same boost-invariant plateau around mid-rapidity, whereas the flanks at larger rapidities are different and depend on the correlation length ϵ/R. By decreasing the thickness of the colliding nuclei $g^2\mu R \to 0$, one approaches the boost invariant limit, where the central plateau extends across all rapidities.

Next we will investigate the dependence of the rapidity profile on the UV and IR regulators. In Fig. 4.3, we plot the transverse pressure normalized to its value at mid-rapidity for different longitudinal extents $g^2\mu R$. In the left panel we fix the UV regulator to $\Lambda = 5g^2\mu$ and vary the infrared regulator m to three different values. Similarly, for the right panel, the IR regulator is set to constant $m = g^2\mu$, and Λ takes three different values. We observe that for a constant proper time $g^2\mu\tau_0 = 5$, the profiles are largely insensitive to the variation. Similar to Fig 4.2, a boost invariant plateau around mid-rapidity emerges upon decreasing the thickness of the colliding nuclei.

4.5   Closing Remarks

We performed the first analytic calculation of the longitudinal profiles of the energy deposition in heavy-ion collisions, by considering the collision of extended nuclei in the dilute limit of the Color Glass Condensate effective field theory of high-energy QCD. We obtained general analytic expressions for the color fields produced in the forward light cone (c.f. Eqns. 4.64, 4.65, 4.66), and employed them to evaluate the rapidity profile of the transverse pressure within a simple specific model of the nuclear collision geometry.

By comparing the (semi-)analytic results in the dilute approximation to non-perturbative 3+1 D classical Yang-Mills simulations, we confirm excellent agreement in the dilute regime. Even beyond the dilute limit, our approximation appears to capture the rapidity profiles rather well, while the overall magnitude of energy deposition is overestimated.

Since our analytic expressions allow for an efficient numerical determination of the energy momentum tensor $T^{\mu\nu}$, the results presented in this thesis provide new opportunities to further explore the longitudinal structure of matter produced in high-energy heavy-ion collisions, to study e.g. the interplay of longitudinal and transverse fluctuations and develop new Monte-Carlo event generators for the initial state of heavy-ion collisions.

In the spirit of the global polarization measurement in non central collisions [131, 132] and the measurement of anomalous transport phenomenon related with the Chiral-Magnetic effect [133–135] at RHIC and LHC energies, it could also be interesting to investigate the angular momentum of Glasma, one and two point function of the energy density and Chern-Simons current, in the near future. Since these initial state correlation are reflected in the collective dynamics of QGP medium, extending the previous boost-invariant calculations [36, 37, 136, 137] to 3+1 D will help in properly characterising the transport properties of the medium.

Chapter 5

Longitudinal structure of initial state in p-Pb collisions

This chapter shows an application of a 3+1 D CGC model to the phenomenological study of azimuthal correlations in p+Pb collisions. Section 5.1 refers to the approach of extending the 2+1 D IP-Glasma model to three dimension by using JIMWLK evolution equations. We would like to emphasize that this formalism also includes the rapidity structure which results from the fluctuation of the color charges within the forward light-cone but in contrast to the framework developed in the previous two chapters, regards the color charges as static. The advantage of using this framework is that it makes simulations significantly less expensive and enables phenomenological studies. In Section 5.2, we study the nature of high and low multiplicity events by computing the gluon multiplicity distribution and dipole scattering amplitude. We then turn to a detailed discussion of event geometry and initial state momentum correlations in Section 5.3.

5.1 The 3D IP-Glasma model

We follow the description of [59, 61, 63, 138–140] which is built on the high-energy factorization of the expectation values of sufficiently inclusive quantities [141–143]. Based on the Color Glass Condensate effective field theory of high-energy QCD, observables $O(y_{\mathrm{obs}})$ at a rapidity y_{obs} can be calculated on an event-by-event basis

$$O(y_{\mathrm{obs}}) = O_{\mathrm{cl}}\Big(V^p_{\mathbf{x}_\perp}(-y_{\mathrm{obs}}), V^{Pb}_{\mathbf{x}_\perp}(+y_{\mathrm{obs}}) \Big) , \qquad (5.1)$$

as a functional of the light-like Wilson lines $V_{\mathbf{x}_\perp}^p(-y_{\text{obs}})$ and $V_{\mathbf{x}_\perp}^{Pb}(+y_{\text{obs}})$ of the projectile (p) and target (Pb), by solving the classical Yang-Mills (CYM) equations $[D_\mu, F^{\mu\nu}] = 0$. Starting from initial conditions $V_{\mathbf{x}_\perp}^{p/Pb}(-y_{\text{max}})$ determined by the IP-Glasma model [18, 19] at the maximal observed rapidity y_{max}, the rapidity evolution of the light-like Wilson lines $V_{\mathbf{x}_\perp}^{p/Pb}(y)$ is calculated by the JIMWLK evolution equation (2.109), which therefore governs the longitudinal structure of observables according to Eq. (5.1). While the factorization in Eq. (5.1) has been proven only for inclusive quantities which encompass measurements at a single rapidity [141], we will use the same prescription to calculate un-equal rapidity correlations on an event-by-event basis. We believe that extension of factorization framework beyond the local observable will at least capture the important effects of unequal rapidity correlations, and refer to [144] for additional discussions of the associated caveats, and provide details of the implementation of the 3D-Glasma model below.

5.1.1 IP-Glasma initial condition

The IP-Glasma model combines a model for the initial color charge density distribution with a solver for the Yang-Mills equations, which govern the initial conditions and evolution of the gluon fields produced in the collision of two nuclei. Here, we use it to determine the nuclei's gluon Wilson lines at the initial rapidities (the largest x values). Wilson lines at smaller x then follow from JIMWLK evolution.

The gluon fields in the incoming nuclei are generated by the moving valence charges according to the Yang-Mills equations $[D_\mu, F^{\mu\nu}] = J^\nu$. The current on the right hand side of this equation is given by the sum of the two nuclei's color currents (the moving large x degrees of freedom)

$$J^\nu = \delta^{\nu+}\rho_{Pb}(\mathbf{x}_\perp)\delta(x^-) + \delta^{\nu-}\rho_p(\mathbf{x}_\perp)\delta(x^+).\tag{5.2}$$

The color charges $\rho_{Pb}(\mathbf{x}_\perp)$ and $\rho_p(\mathbf{x}_\perp)$ will be sampled from a color charge density assuming local Gaussian correlations as in the McLerran-Venugopalan (MV) model [83, 145]. The spatially dependent color charge densities, $g^2\mu_{Pb/p}(x, \mathbf{b}_\perp)$ are determ-

ined using the IPSat model [146, 147], as described in Appendix C. It provides the saturation scale as a function of the nuclear thickness function at a given Bjorken x.

In fact, in IP-Glasma we self-consistently determine $Q_s(x, \mathbf{b}_\perp)$ by iteratively solving for

$$x = x(\mathbf{b}_\perp) = \frac{Q_s(x, \mathbf{b}_\perp)}{\sqrt{s_{\mathrm{NN}}}} e^{-y}, \tag{5.3}$$

with $\sqrt{s_{\mathrm{NN}}}$ being the center of mass energy of the collision.

The thickness functions, which provide the $\mathbf{b}_\perp$ dependence, are determined from sampling a Woods-Saxon distribution (in the case of the Pb nucleus) and using a 2D Gaussian distribution for every nucleon. The parameters of the model are constrained using deeply inelastic scattering data on protons from HERA [148]. For a detailed description of the implementation used in this work see [149]. The public IP-Glasma code can be found at [150].

In practice, for each nucleus one solves for the Wilson lines numerically, approximating the path ordered exponential by the product [85]

$$V_{\mathbf{x}_\perp}^{Pb/p} = \prod_{k=1}^{N_y} \exp\left(-ig \frac{\rho_{Pb/p}^k(\mathbf{x}_\perp)}{\boldsymbol{\nabla}^2 + \tilde{m}^2} \right). \tag{5.4}$$

Here, $\tilde{m} = 0.2$ GeV is an infrared regulator that is used to avoid unphysical Coulomb tails, $N_y = 50$ is the number of slices in the longitudinal direction, and, as in the McLerran-Venugopalan model, the ρ_{Pb}^k and ρ_p^k have zero mean and their two-point functions satisfy (suppressing the subscripts Pb and p for clarity)

$$\langle \rho_i^a(\mathbf{b}_\perp) \rho_j^b(\mathbf{x}_\perp) \rangle = \frac{g^2 \mu^2(x, \mathbf{b}_\perp)}{N_y} \delta^{ab} \delta^{ij} \delta^{(2)}(\mathbf{b}_\perp - \mathbf{x}_\perp). \tag{5.5}$$

We generate a total of $N_p = 32$ and $N_{Pb} = 8$ configurations of the Wilson lines $V_{\mathbf{x}_\perp}^{p/Pb}(-y_{\max})$ of the proton and lead nuclei at the largest x value, corresponding to the initial rapidity $-y_{\max} = -2.4$, with transverse coordinates $(\mathbf{x}_\perp)$ discretized on a $N_s \times N_s$ lattice with $N_s = 1024$ sites and lattice spacing $a_s = 0.02$ fm.

5.1.2 JIMWLK evolution

Starting from the IP-Glasma initial conditions for the Wilson lines $V_{\mathbf{x}_\perp}^{p/Pb}(-y_{\mathrm{max}})$, we perform the JIMWLK [104, 151–154] evolution from $y = -2.4$ to $y = +2.4$ for each configuration of the proton and nucleus. We store the configurations for various slices in rapidity, in steps of $y = 0.2$

The implementation of the JIMWLK solver is based on the Eq. (5.1), which clearly reflects that the rapidity evolution in two nuclei is different $\pm y_{\mathrm{obs}}^{p/Pb}$ when computing observables at $y_{\mathrm{obs}} \neq 0$. Specifically, we express the JIMWLK hierarchy in terms of a functional Langevin equation for the Wilson lines using Eqs. (2.109) – (2.113). For the purpose of completeness, we again write the JIMWLK equation for each Langevin step as derived in [109]

$$V_{\mathbf{x}_\perp}(y + dy) = \exp\left\{ -i\frac{\sqrt{\alpha_s dy}}{\pi} \int_{\mathbf{z}_\perp} K_{\mathbf{x}_\perp - \mathbf{z}_\perp} \cdot \left(V_{\mathbf{z}_\perp} \boldsymbol{\xi}_{\mathbf{z}_\perp} V_{\mathbf{z}_\perp}^\dagger \right) \right\}$$
$$\times V_{\mathbf{x}_\perp}(y) \exp\left\{ i\frac{\sqrt{\alpha_s dy}}{\pi} \int_{\mathbf{z}_\perp} K_{\mathbf{x}_\perp - \mathbf{z}_\perp} \cdot \boldsymbol{\xi}_{\mathbf{z}_\perp} \right\}, \tag{5.6}$$

with Gaussian noise $\boldsymbol{\xi}_{\mathbf{z}_\perp} = (\xi_{\mathbf{z}_\perp,1}^a t^a, \xi_{\mathbf{z}_\perp,2}^a t^a)$ that is local in transverse coordinate, color, and rapidity: $\langle \xi_{\mathbf{z}_\perp,i}^b(Y) \rangle = 0$ and

$$\langle \xi_{\mathbf{x}_\perp,i}^a(y) \xi_{\mathbf{y}_\perp,j}^b(y') \rangle = \delta^{ab} \delta^{ij} \delta^{(2)}_{\mathbf{x}_\perp \mathbf{y}_\perp} \delta(y - y'). \tag{5.7}$$

Following [110], we employ a regularized JIMWLK kernel

$$K_{\mathbf{x}_\perp - \mathbf{z}_\perp} = m|\mathbf{x}_\perp - \mathbf{z}_\perp| \, K_1(m|\mathbf{x}_\perp - \mathbf{z}_\perp|) \, \frac{\mathbf{x}_\perp - \mathbf{z}_\perp}{(\mathbf{x}_\perp - \mathbf{z}_\perp)^2}, \tag{5.8}$$

which suppresses emission at large distance scales and limits growth in impact parameter space. The modified Bessel function of the second kind $K_1(x)$ behaves as $xK_1(x) = 1 + \mathcal{O}(x^2)$ for small arguments x, leaving the kernel approximately unmodified. In contrast, for large arguments $K_1(x) = \sqrt{\frac{\pi}{2x}} e^{-x}$ decays exponentially.

We note that the only free parameters controlling the JIMWLK evolution in Eq. (5.6) are the (fixed) coupling constant α_s and the infrared regulator m, and we will consider variations of both parameters to assess the sensitivity of our results. We illustrate
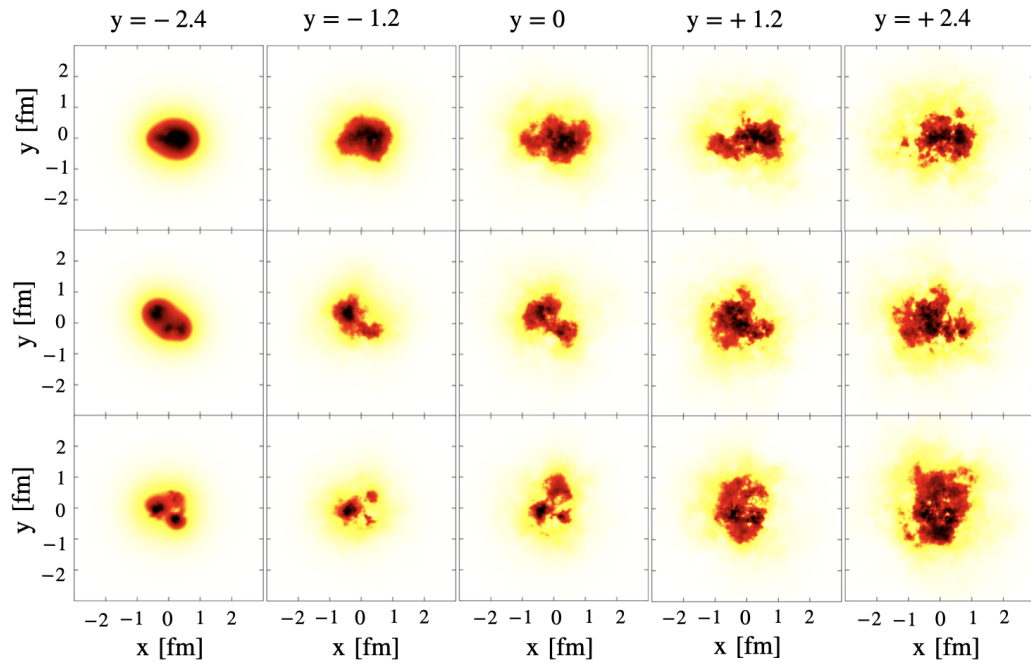
Figure 5.1: Trace of Wilson line as a function of transverse coordinates to show the rapidity evolution of three random proton configurations obtained via JIMWLK evolution. Simulation parameters: $\alpha_s = 0.3$ and $m = 0.2$ GeV

the JIMWLK evolution in Fig. 5.1, where we present the transverse structure of three different protons by plotting trace of Wilson line $1 - \text{Re}[\text{tr}(V_{x_\perp})]/N_c$ at different rapidities. The leftmost column shows the proton structure at $y = -2.4$ with gluon fields concentrated in three hot spots at the position of constituent quarks. We observe that with smaller x or higher rapidities additional fluctuations in the gluon distribution influence the shape of the proton, which largely has an imprint of the gluon distribution at the largest x ($y = -2.4$), as already mentioned in [110]. As x decreases, the saturation scale Q_s increases, which ultimately leads to a decrease in the characteristic transverse length scale $\propto 1/Q_s$, which means that the resulting small-scale structure becomes finer. Later we will see how this significant fluctuation in the gluon distribution of the proton affects the rapidity dependence of the observables.

5.1.3 Event generation & classical Yang-Mills evolution

Having determined N_p proton configurations and N_{Pb} lead configurations over the entire range of rapidities $-2.4 \leq y \leq 2.4$, we proceed to generate events, where for each of the $N_p \times N_{Pb}$ combination of protons and lead nuclei, we perform $N_{\mathbf{b}_\perp} = 16$ collisions with different impact parameter $\mathbf{b}_\perp$, sampled according to a two-dimensional uniform distribution with the restriction $0 < |\mathbf{b}_\perp| < 8$ fm.[1]

Based on the JIMWLK evolved Wilson lines, the initial conditions for the non-vanishing components of the gauge fields $A^i_{\mathbf{x}_\perp}(\tau = 0^+), E^\eta_{\mathbf{x}_\perp}(\tau = 0^+)$ in the forward light-cone at a given rapidity y_{obs} are then given by

$$A^i_{\mathbf{x}_\perp}(\tau = 0^+, Y_{\mathrm{obs}}) = \frac{i}{g}\left[\left(V^p_{\mathbf{x}_\perp}(+y_{\mathrm{obs}})\partial^i V^{p\,\dagger}_{\mathbf{x}_\perp}(+y_{\mathrm{obs}})\right)\right.$$
$$\left. + \left(V^{Pb}_{\mathbf{x}_\perp+\mathbf{b}_\perp}(-y_{\mathrm{obs}})\partial^i V^{Pb\,\dagger}_{\mathbf{x}_\perp+\mathbf{b}_\perp}(-y_{\mathrm{obs}})\right)\right] \tag{5.9}$$

$$E^\eta_{\mathbf{x}_\perp}(\tau = 0^+, y_{\mathrm{obs}}) = \frac{i}{g}\left[\left(V^p_{\mathbf{x}_\perp}(+y_{\mathrm{obs}})\partial^i V^{p\,\dagger}_{\mathbf{x}_\perp}(+y_{\mathrm{obs}})\right)\right.$$
$$\left(V^{Pb}_{\mathbf{x}_\perp+\mathbf{b}_\perp}(-y_{\mathrm{obs}})\partial^i V^{Pb\,\dagger}_{\mathbf{x}_\perp+\mathbf{b}_\perp}(-y_{\mathrm{obs}})\right)\right] \tag{5.10}$$

Starting from the initial conditions in Eqns. (5.9) and (5.10), we then solve the lattice discretized form of the classical Yang-Mills (CYM) equations of motion up to $\tau = 0.2$ fm/c [88], where we determine the energy-momentum tensor $T^{\mu\nu}$ [19], gluon spectra $\frac{dN_g}{d^2\mathbf{p}_\perp dy}$ and gluon multiplicity $dN_g/dy = \int d^2\mathbf{p}_\perp \frac{dN_g}{d^2\mathbf{p}_\perp dy}$ as described in Eqs (2.104)–(2.106).

Based on the factorization formula in Eq. (5.1), the rapidity Y_{obs} dependence of these observables in each event is then calculated as in [41] from a series of independent 2+1D CYM simulations, which according to Eq. (5.6) start from the same Wilson lines $V^p_{\mathbf{x}_\perp}$ and $V^{Pb}_{\mathbf{x}_\perp}$ evolved up to different rapidities $y = \pm y_{\mathrm{obs}}$. We will consider a rapidity range $y_{\mathrm{obs}} \in [-2.4, +2.4]$, where $y_{\mathrm{obs}} = -2.4(+2.4)$ corresponds to no JIMWLK evolution in the proton (lead nucleus), and calculate observables in intervals of $\Delta y = 0.4$, and unless stated otherwise $\alpha_s = 0.15$. This choice of $\alpha_s = 0.15$ has

---

[1]Note that in order to avoid interpolation of $SU(N_c)$ matrices, we round the impact parameter $\mathbf{b}_\perp$ to the next lattice site.
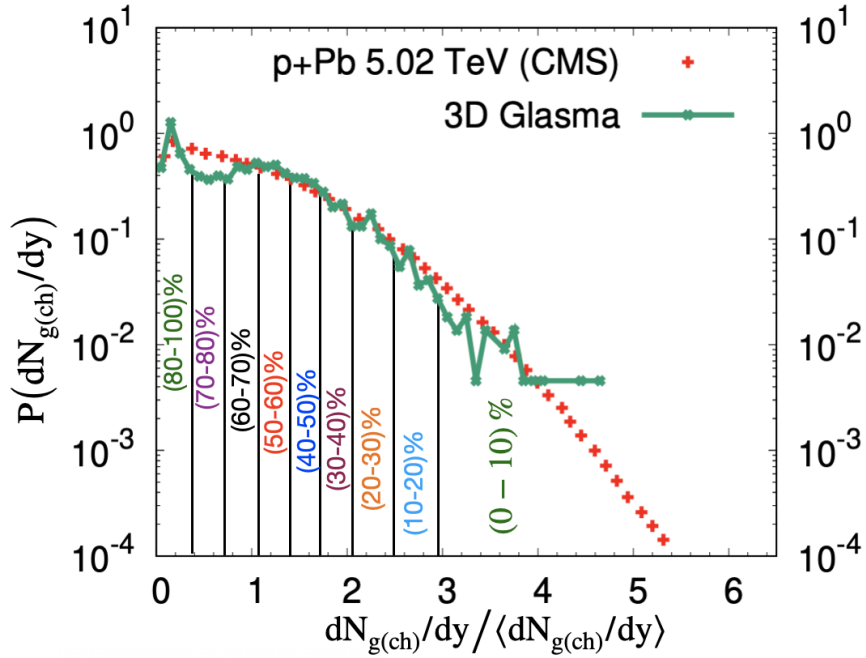
Figure 5.2: Normalized probability distribution $P(dN/dy)$, as a function of dN/dy scaled by its expectation value $\langle dN/dy \rangle$ for $\alpha_s = 0.15$ and $m = 0.2\,\text{GeV}$. Vertical lines mark different centrality classes. Crosses are experimental data for raw reconstructed primary tracks in $\sqrt{s} = 5.02\,\text{TeV}$ p+Pb collisions from the CMS collaboration [155].

been made because the fixed coupling JIMWLK evolution gives rise to a too fast evolution in x which is not phenomenologically viable.

5.1.4 Gluon multiplicity and centrality selection

Based on the above procedure, we obtain a total of $N_{\text{events}} = N_{\text{coll}} \times N_p \times N_{Pb} = 4096$ events, which we further classify into centrality classes according to their gluon multiplicity $g^2 dN_g/dy|_{y_{\text{obs}}=0}$ at mid-rapidity $y_{\text{obs}} = 0$. Since we do not invoke any collision criteria (e.g. $N_{\text{coll}} \geq 1$), we first disregard events with $g^2 dN_g/dy|_{y_{\text{obs}}=0} < 4$ from our event selection and subsequently perform the usual binning. We present the midrapidity gluon multiplicity distribution scaled by the mean multiplicity in Fig. 5.2 and compare to experimental data on the uncorrected reconstructed primary tracks from the CMS Collaboration [155].

The width of the gluon multiplicity distribution agrees well with that of the experimental data on reconstructed tracks. The gluon distribution has some peak and dip structure at small multiplicities, which is not seen in the experimental data, but for

$g^2 dN_{g(ch)}/dy$	$0-5\%$	$40-50\%$	$60-70\%$	$80-90\%$
$m = 0.2$ **GeV**	141.1	52.9	29.2	9.2
$m = 0.4$ **GeV**	129.0	49.0	–	9.9
ALICE	42.6	16.1	9.6	4.3
$g^2 dE_\perp/dy$ **[GeV]**				
$m = 0.2$ **GeV**	454.8	161.8	79.7	20.0
$m = 0.4$ **GeV**	417.7	153.2	–	22.6

Table 5.1: Gluon multiplicity $g^2 dN/dy$ and transverse energy $g^2 dE_\perp/dy$ at mid-rapidity $y = 0$ for $\alpha_s = 0.15$ along with the ALICE data [155] for $dN_{\text{ch}}/d\eta$ for centrality classes $(0-5), (40-50), (60-80)$, and $(80-100)\%$
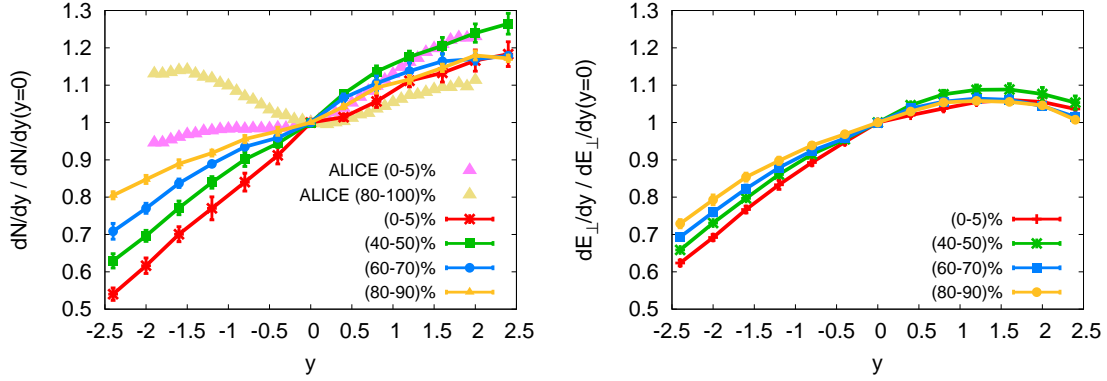
Figure 5.3: Gluon multiplicity relative to its value at $y = 0$ compared to experimental from the ALICE collaboration [156] (left) and transverse energy per unit rapidity $dE_\perp/dy \propto \tau\varepsilon(\tau = 0.2\,\text{fm})$ relative to its value at mid rapidity (right) for different centrality classes. Simulation parameters: $\alpha_s = 0.15$ and $m = 0.2$ GeV

larger multiplicities (equal or greater than the mean) the data is well described. The figure also indicates the centrality classes as obtained from the gluon distribution.

5.2 Global event structure & nature of high multiplicity events

Before we discuss the event-by-event geometry and azimuthal correlations in high-energy p+Pb collisions, it is insightful to briefly comment on the general features of low and high multiplicity events. We first study the rapidity dependence of the multiplicity dN_g/dy and transverse energy $dE_\perp/dy$. In Fig. 5.3 we show dN_g/dy and $dE_\perp/dy$ normalized to their value at mid-rapidity $dN_g/dy|_{y=0}$ and $dE_\perp/dy|_{y=0}$ for different centrality classes $(0-5), (40-50), (60-70)$, and $(80-90)\%$. Values at

mid-rapidity are provided in Table 5.1 where one can essentially see that the ratio of $(0-5)\%$ to $(40-50)\%$ and $(60-70)\%$ roughly matches with the respective ratio for ALICE data.

We observe that the rapidity dependence of both the multiplicity and the transverse energy flattens as one approaches more peripheral events. The gluon distribution generally shows a steeper rapidity dependence than the experimental data from the ALICE Collaboration [155], which is essentially symmetric in the (80-100)% bin. We further observe a non-monotonic behavior with centrality for positive y. This is related to the behavior of the proton's saturation scale, which grows less strongly with rapidity for the most central events compared to other centralities, suppressing the gluon yield at forward rapidities. We will show this behavior of Q_s below in Fig. 5.5.

The transverse energy shows a slightly weaker centrality dependence compared to the gluon multiplicity. This could be a consequence of the transverse energy being more sensitive to the larger of the two Q_s values.

In the following, we extract the average Pb and p saturation scales $Q_s(y)$ for different centralities, which will allow further insight into the properties of low and high multiplicity events. Furthermore, we determine the systems size $S_\perp(y)$ for different centrality classes. Specifically, the saturation scale $Q_s(Y)$ is extracted from the dipole scattering amplitude

$$D(\mathbf{r}_\perp, \mathbf{d}_\perp) = \frac{1}{N_c} \text{tr} \left[V_{\mathbf{d}_\perp + \mathbf{r}_\perp/2} V^\dagger_{\mathbf{d}_\perp - \mathbf{r}_\perp/2} \right] , \quad (5.11)$$

averaged over (dipole) impact parameters $|\mathbf{d}_\perp| < 0.2\,R_p$ from the collision point[2] with R_p being the radius of proton (for more details refer to Appendix C). By following previous works [110], we extract the distance $|\mathbf{r}_\perp|_c$ where the dipole amplitude equals a value of c, i.e.

$$D(|\mathbf{r}_\perp|_c, |\mathbf{d}_\perp| < 0.2R_p) = c , \quad (5.12)$$

---

[2]Based on Eqs. (5.9) and (5.10) the collision point corresponds to the center of mass of the proton and respectively the impact parameter $\mathbf{b}_\perp$ of collision for the lead nucleus.
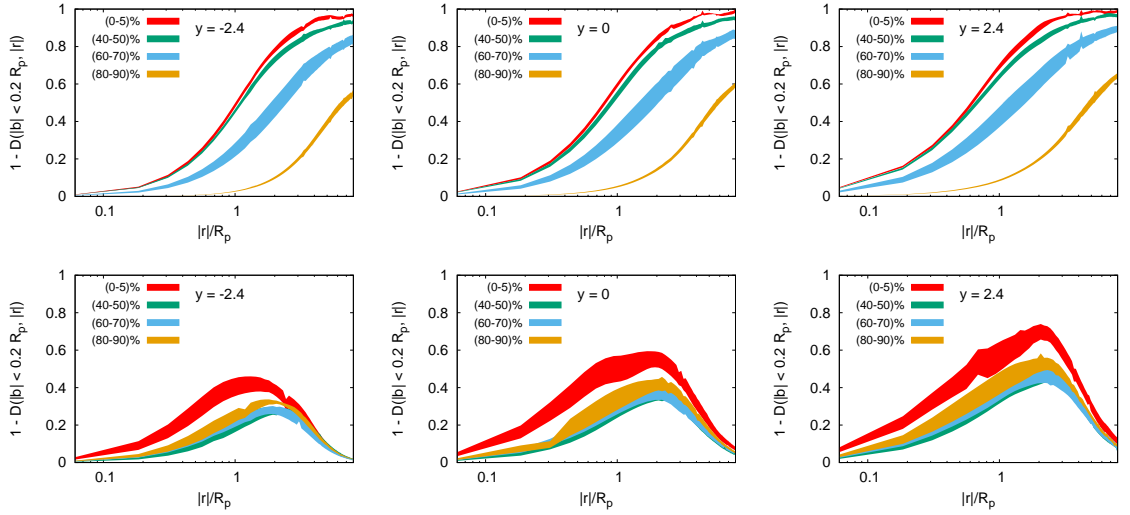
Figure 5.4: Dipole scattering amplitudes $1-D(\mathbf{r}_\perp, |\mathbf{d}_\perp| < 0.2R_p)$ for the lead nucleus (top) and for the proton (bottom) at three different rapidites $y = -2.4, 0, +2.4$ as a function of dipole size $|\mathbf{r}_\perp|$ in units of the proton radius R_p.

and calculate $Q_s = 2/|\mathbf{r}_\perp|_c \log^{1/2}(1/c)$ according to the parametrization $D(r) = \exp(-Q_s^2 \mathbf{r}_\perp{}^2/4)$. We employ $c = 0.8$ and 0.9 to estimate the uncertainty of this procedure.

The system size $S_\perp$ is determined from the energy momentum tensor as

$$S_\perp = \frac{\int d^2\mathbf{x}_\perp \; \mathbf{x}_\perp{}^2 \; T^{\tau\tau}(\mathbf{x}_\perp)}{\int d^2\mathbf{x}_\perp \; T^{\tau\tau}(\mathbf{x}_\perp)} \tag{5.13}$$

which we evaluate at $\tau = 0.2$ fm/c after the collision. Before we address saturation scales and system size, we show the dipole scattering amplitude $1 - D(\mathbf{r}_\perp, |\mathbf{d}_\perp| < 0.2R_p)$ for Pb nucleus (top) and proton (bottom) as a function of dipole size $r_\perp$ for a fixed range of impact parameter $|\mathbf{d}_\perp| < 0.2R_p$ for three different rapidities $y = -2.4, 0, +2, 4$ in different centrality classes in Fig. 5.4. Dipole amplitude vanishes if the gluon density is probed by the color charges at the exact same point $r = 0$ but then it gradually rises and reaches a maximum at $r_\perp/R_p \sim 1$. We see that the scattering amplitude saturates $D = 1$ for $(0-5)\%$ and $(40-50)\%$ whereas the other two centrality classes are dilute even at large rapidities in the Pb nucleus. For proton (bottom), the dipole amplitude is much below the saturation level even after full rapidity evolution and starts to fall when the separation between the dipole
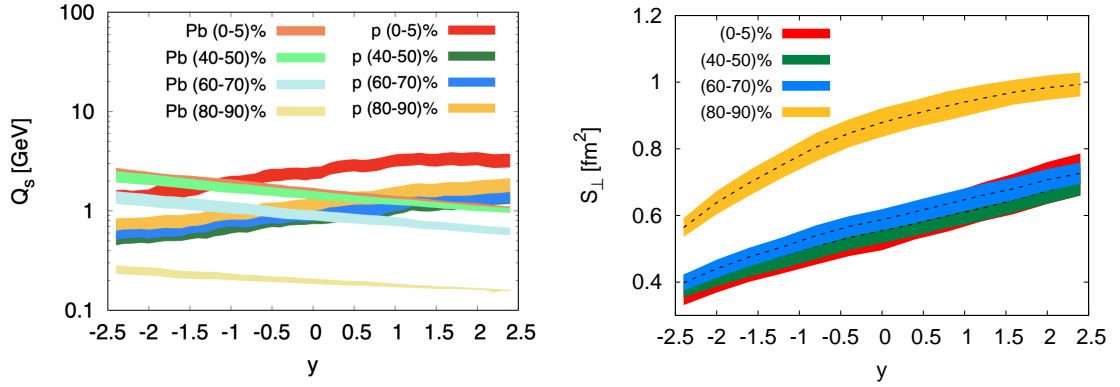
Figure 5.5: Left:Saturation scale $Q_s(y)$ as a function of rapidity y for proton (p) and lead nucleus (Pb) for different centrality classes. Right: System size $S_\perp$ as a function of rapidity y for different centrality classes. All results are for $m = 0.2$ GeV and $\alpha_s = 0.15$.

exceeds the size of proton. We also note that for protons the shape of the curve for peripheral events remains the same and is less dense than the central events.

We have compactly summarized the results for the dependence of saturation scale (left) and system size (right) on rapidity for various centrality classes in Fig. 5.5. The exponential growth of the $Q_s(y) \propto \exp(\pm y_{p/Pb})$ where arises from the JIMWLK evolution. The proton saturation scale Q_s^p is similar in the three more peripheral events, while the nucleus' Q_s^{Pb} depends more strongly on centrality, indicating that the multiplicity is determined by the impact parameter, i.e., the position in the lead nucleus where the proton hits, as well as fluctuations in the lead nucleus. The significant difference in Q_s^p in the top 5% centrality class from other peripheral classes and similarity between Q_s^{Pb} in (0-5) and $(40-50)\%$ class indicates that the high multiplicity events are mainly due to denser protons.

On the right panel of Fig. 5.5, we see that the system size ($S_\perp$) shows almost a linear trend due to growth of the proton size with rapidity, as seen in Fig. 5.1. The most peripheral events show a significantly larger area, which seems counter-intuitive at first. But given the definition of the area measure in (5.13), an overall very small but spread out energy density can lead to a large area. This seems to be the dominant effect in the most peripheral event we studied, while for other centralities the difference in multiplicities is mainly due to the larger of the two Q_s, as the areas are roughly equal.

5.3 Event geometry & initial state moment correlations

Now that we have established the basic features of the events in different centrality classes, we continue to investigate the longitudinal structure of the event geometry and the initial state momentum anisotropy. Before we continue, we would like to note that the gluon spectrum at each rapidity is proportional to $\delta(\eta - y)$ [157], where η is the space-time rapidity. Accordingly, we will be using η and y interchangeably. We follow standard procedure and characterize the event geometry in terms of the eccentricities

$$\varepsilon_n(\eta) = \frac{\int d^2\mathbf{r}_\perp T^{\tau\tau}(\eta, \mathbf{r}_\perp) \, |\mathbf{r}_\perp|^n e^{in\phi_{\mathbf{r}_\perp}}}{\int d^2\mathbf{r}_\perp T^{\tau\tau}(\eta, \mathbf{r}_\perp) \, |\mathbf{r}_\perp|^n} \tag{5.14}$$

Similarly, following [54, 158, 159] the initial state momentum anisotropy can characterized in terms of the anisotropic energy flow

$$\varepsilon_p(\eta) = \frac{\int d^2\mathbf{r}_\perp \ T^{xx}(\eta, \mathbf{r}_\perp) - T^{yy}(\eta, \mathbf{r}_\perp) + 2iT^{xy}(\eta, \mathbf{r}_\perp)}{\int d^2\mathbf{r}_\perp \ T^{xx}(\eta, \mathbf{r}_\perp) + T^{yy}(\eta, \mathbf{r}_\perp)} \tag{5.15}$$

or alternatively as in [159, 160] in terms of the azimuthal anisotropy v_2^g of the produced gluons [3]

$$v_2^g(\eta) = \frac{\int d^2\mathbf{k}_\perp |\mathbf{k}_\perp| \frac{dN}{d\eta d^2\mathbf{k}_\perp} e^{2i\phi_{\mathbf{k}_\perp}}}{\int d^2\mathbf{k}_\perp |\mathbf{k}_\perp| \frac{dN}{d\eta d^2\mathbf{k}_\perp}} \tag{5.16}$$

We evaluate the expression in Eqns. (5.14, 5.15, 5.16) at $\tau = 0.2$ fm/c to calculate $\varepsilon_n, \epsilon_p, v_2^g$ as a function of rapidity η on an event-by-event basis. Subsequently, to quantify the overall rapidity dependence we compute the correlation functions

$$C_\mathcal{O}(\eta_1, \eta_2) = \Big\langle \mathrm{Re}\Big(\mathcal{O}(\eta_1)\mathcal{O}^*(\eta_2)\Big)\Big\rangle \tag{5.17}$$

where $\langle . \rangle$ denotes an event average and $\mathcal{O}$ is any of the above observables. While the correlation function $C_\mathcal{O}$ contains information about both the magnitude and rapidity

---

[3] We note that in the quasi-particle picture the definitions of e_p and v_2^g agree with each other.
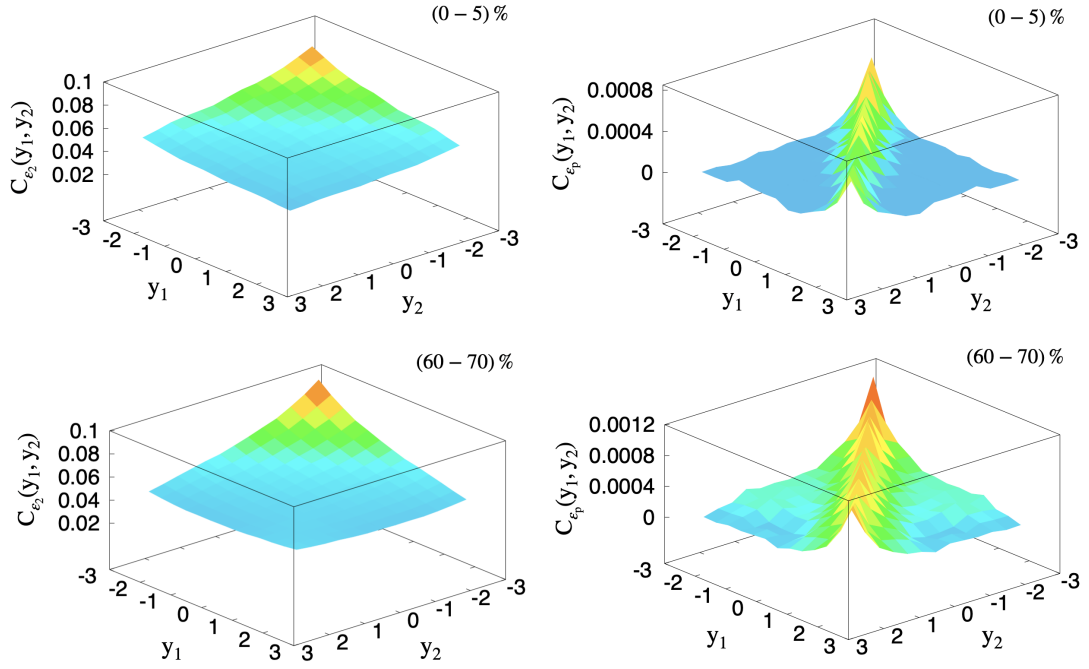
Figure 5.6: Two point correlation function for second order eccentricity C_{ε_2} (top-left) and momentum anisotropy C_{ε_p} (top-right) for $(0-5)\%$ centrality class for $\alpha_s = 0.15$ and $m = 0.2$ GeV. Bottom panel demonstrates the same observable for $(60-70)\%$ centrality class

dependence of the correlation function, we will also consider the normalized rapidity correlation function

$$C_{\mathcal{O}}^N(\eta_1, \eta_2) = \frac{C_{\mathcal{O}}(\eta_1, \eta_2)}{\sqrt{\langle |\mathcal{O}(\eta_1)|^2 \rangle \langle |\mathcal{O}(\eta_2)|^2 \rangle}} \tag{5.18}$$

to further analyze the longitudinal decorrelation of the transverse geometry and initial state momentum correlations. Our results for 3 D structure of event geometry and initial state momentum anisotropy are compactly summarised in Fig. 5.6 where we present the two point correlation function Eq. (5.17) of 2nd order eccentricity ε_2 and momentum anisotropy ϵ_p for $(0-5)\%$ (top) and $(60-70)\%$ (bottom). We observe that geometry is correlated across large rapidity intervals whereas initial state momentum correlations are relatively short range in rapidity for central as well as peripheral events. This can be understood as follows: ϵ_p is sensitive to microscopic momentum space correlations within the proton, so even a single gluon emission easily changes the color structure and thereby destroys the correlations, whereas melting the entire geometry of a colliding system is much more difficult. This clearly
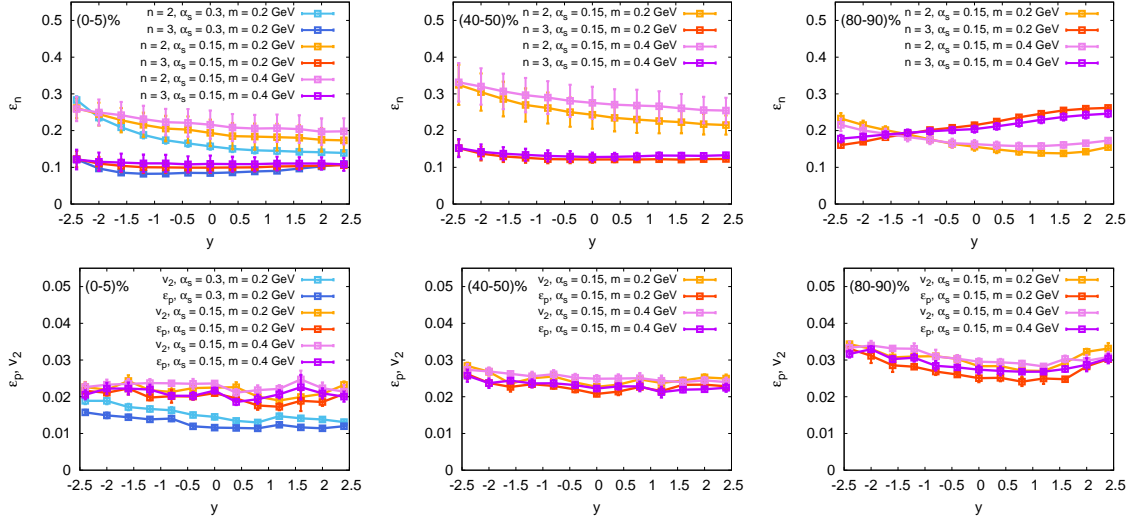
Figure 5.7: Geometric eccentricities $\sqrt{\langle|\varepsilon_n^2(\eta)|^2\rangle}$ (top) and initial momentum anisotropies $\sqrt{\langle|\varepsilon_p(\eta)|^2\rangle}$ and $\sqrt{\langle|v_2^g(\eta)|\rangle}$ for different centrality classes 0-5% (left), 40-50% (center) and 80-90% (right) as a function of rapidity.

excludes any other qualitative understanding of the long-range azimuthal correlation in terms of event multiplicity, as in [53], where the dominant mechanism for events with low multiplicity is ascribed to the intrinsic momentum space correlation. As these 3 D plots contain a lot of information, but its hard to see quantitatively, we will try to decipher the basic features of the observables below.

We show the geometric eccentricities $\sqrt{\langle|\varepsilon_n^2(\eta)|^2\rangle}$ (top) and initial momentum anisotropies $\sqrt{\langle|\varepsilon_p(\eta)|^2\rangle}$ and $\sqrt{\langle|v_2^g(\eta)|\rangle}$ (bottom) as a function of rapidity for three different classes $(0-5)$, $(40-50)$ and $(80-90)\%$ for $m = 0.2$ GeV and $m = 0.4$ GeV in Fig. 5.7. We observe that the curve remains essentially the same for different values of infrared regulator m in all the centrality classes. In most cases ε_2 decreases with increasing rapidity, and does so more rapidly for larger α_s and smaller m, as expected by how these parameters affect the JIMWLK evolution speed. For our standard parameters of $m = 0.2\,\mathrm{GeV}$ and $\alpha_s = 0.15$ the rapidity dependence is rather weak. For the most peripheral bin ε_2 has a shallow minimum as a function of rapidity. The triangularity ε_3 has an even weaker rapidity dependence than ε_2 in the two more central bins, and increases with increasing rapidity in the most peripheral bin. Given the comparable size of ε_2 and ε_3 in this bin, one might expect the observed anti-correlation between the two quantities, as it is difficult geometrically

to generate a large ε_2 and ε_3 at the same time (This can be seen most easily when arranging just three hot spots. A maximal triangularity goes along with a reduced ellipticity and vice versa.)

The bottom panel in Fig. 5.7 shows the rapidity dependence of the initial state anisotropy ε_p and the gluon elliptic momentum anisotropy v_2^g for the same centrality classes and parameter sets as the eccentricities above. First, it is clear to see that both quantities follow each other closely. The anisotropy of the energy momentum tensor is thus a good predictor of the gluon momentum anisotropy in the situation where strong final state interactions are not included. When those are included, the response to the initial spatial anisotropy will dominate the produced particles' momentum anisotropy in all but the most peripheral events [54, 159]. The rapidity dependence is negligible in most cases, with the case using $\alpha_s = 0.3$ in the most central bin showing the strongest decrease with increasing rapidity. In the most peripheral bin the two quantities show a minimum around $y = 1$.

In Fig. 5.8, the rapidity dependence of ε_2 (left), ε_3 (center) and v_2^{g4} (right) is shown for different centralities or $m = 0.2$ GeV and $\alpha_s = 0.15$. While ε_2 is maximal for 40-50% central collisions, and minimal in the most peripheral bin, ε_3 increases monotonically towards more peripheral events and shows the strongest centrality dependence on the lead going side. The magnitude and centrality dependence of v_2 is only very weakly dependent on the rapidity. As has been observed previously [54, 66], the initial momentum anisotropy driven v_2^g increases with decreasing multiplicity (towards more peripheral events), which can be intuitively understood within the color-domain model [58, 65, 161], where only partons originating from the same color domain are correlated with each other. We show here that this is true for all studied rapidities. Furthermore, the value of v_2^g is largely independent of rapidity in all the centrality bins.

We demonstrate the normalized two point correlation function $C_N(\Delta\eta) = \int d\eta \, C_N(\eta + \Delta\eta/2, \eta - \Delta\eta/2)$ for geometry (top) and initial state momentum anisotropy (bottom) as a function of rapidity separation $\alpha_s\Delta\eta$ for three different centrality classes $(0-5)$

---

[4]As ε_p is basically equivalent to the v_2^g, we only show the centrality dependence of v_2^g.
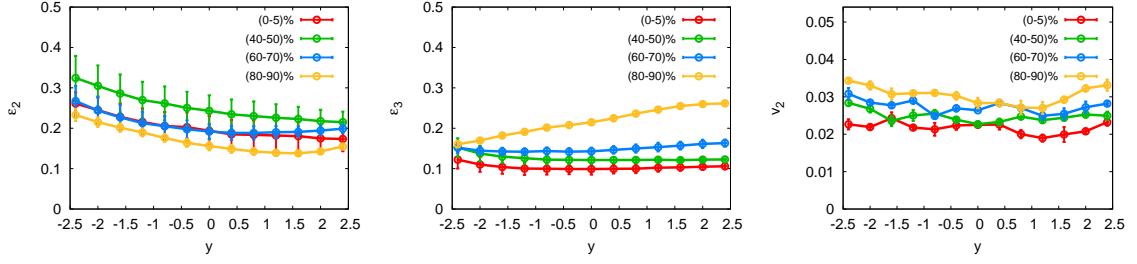
Figure 5.8: Comparison of the rapidity dependence of $\sqrt{\langle|\varepsilon_2^2(\eta)|^2\rangle}$ (left), $\sqrt{\langle|\varepsilon_3^2(\eta)|^2\rangle}$ (center) and $\sqrt{\langle|v_2^g(\eta)|\rangle}$ (right) for different centrality classes for $m = 0.2$ GeV and $\alpha_s = 0.15$
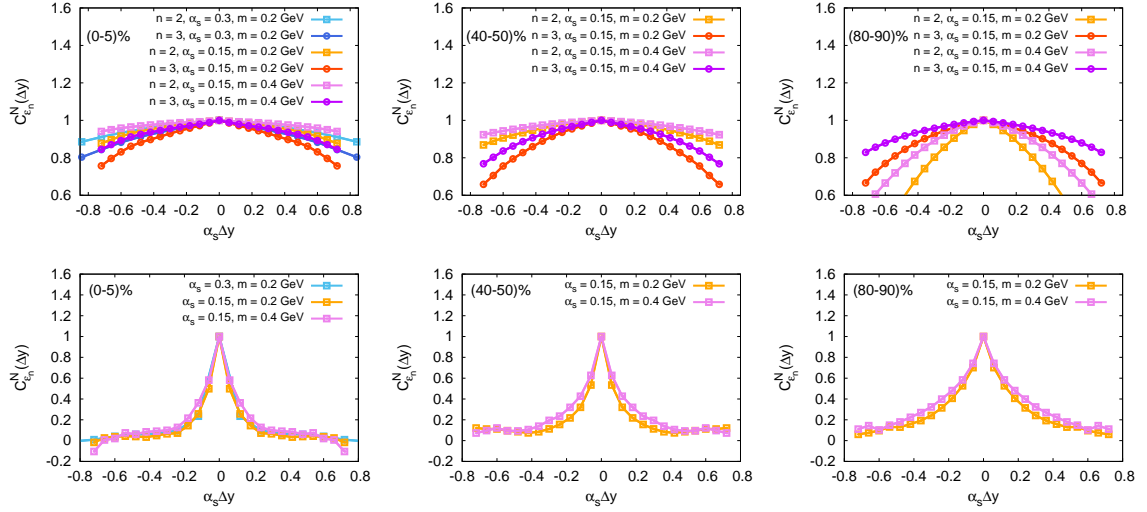
Figure 5.9: Normalized two point correlation function $C^N(\Delta\eta) = \int d\eta\ C^N(\eta + \Delta\eta/2, \eta - \Delta\eta/2)$ for geometric eccentricities $\varepsilon_2, \varepsilon_3$ (top) and initial state momentum anisotropies ε_p, v_2^g (bottom) different centrality classes 0-5% (left), 40-50% (center) and 80-90% (right) as a function of the rapidity separation $\alpha_s\Delta\eta$.
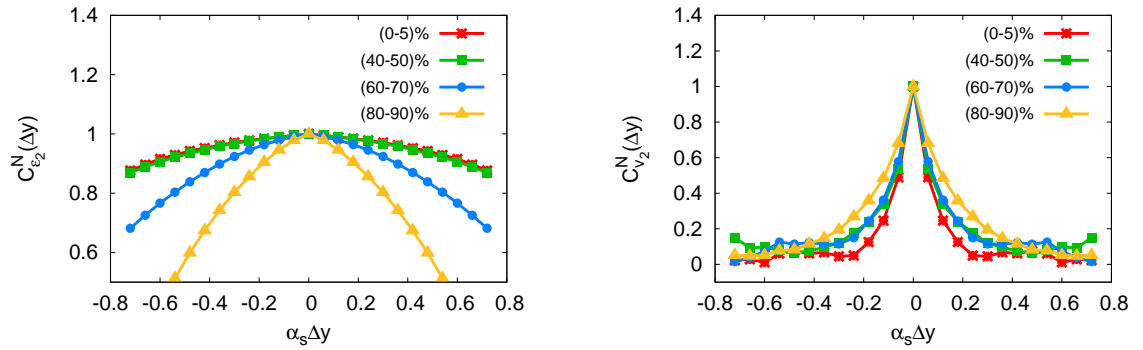
Figure 5.10: Comparison of the normalized correlation function of the geometric eccentricity $C_{\varepsilon_2}^N(\Delta\eta)$ and initial state momentum anisotropy $C_{v_2^g}^N(\Delta\eta)$ for different centrality classes for $\alpha_s = 0.15$ and $m = 0.2$ GeV

(left), $(40 - 50)$ (center) and $(80 - 90)\%$ (right) for $m = 0.2$ GeV and $m = 0.4$ GeV in Fig. 5.9. We observe that the correlation in geometry persists at larger rapidity intervals whereas it dies out quickly in initial state momentum anisotropies. The results presented in top panel mildly depend on the infrared regulator m whereas the dependency on coupling constant in top as well as bottom panel is absorbed in the scaling $\alpha_s \Delta\eta$. For $m = 0.2$ GeV, one sees a slightly faster decorrelation and the effects are more pronounced for the more peripheral events.

The dependency of the normalized correlation function $C^N(\Delta\eta)$ of the geometric eccentricity ε_2 and initial state momentum anisotropy v_2^g on different centrality classes are shown in Fig. 5.10. Again we find that the correlation in geometry (left) is relatively long-ranged in rapidity as compared to initial momentum anisotropy (right) where the correlation never exceeds the width of $1/\alpha_s$ units in rapidity. We further note that the decorrelation of the geometry is faster in more peripheral events where fluctuations play a more prominent role; conversely the decorrelation of initial state momentum correlations occurs less rapidly in more peripheral events.

After examining the rapidity correlation of the event geometry and the initial state momentum correlation, we would now like to connect our results with the experimental observations of long-range rapidity correlation in small systems. We find that the correlation from initial event-geometry are long-ranged in rapidity and hence are more likely to be transformed into momentum correlations by strong final state interaction and get detected in form of ridge in high-multiplicity pp and pA collisions. We find that for low multiplicity events, initial event geometry decorrelates faster and is consistent with the current status of experimental runs where currently no signal of collectivity has been observed in small-systems.

5.4   Closing Remarks

In this chapter, we investigate the event geometry and initial state correlations which are accepted as possible explanations for collective behaviour in high-multiplicity events in proton-proton and proton-nucleus collisions. Within the CGC framework, we follow the approach of extending the IP-Glasma model to three dimension by

using the JIMWLK evolution equation which provides the rapidity dependence by evolving the Wilson lines of the incoming gluon distribution.

Based on this formalism, we collide the proton with Pb nucleus at 5.02 TeV, and first investigate the global event structure and nature of high and low multiplicity events. By comparing the gluon multiplicity with the experimental data from ALICE collaboration, we find that the gluon distribution shows a rather steeper rapidity dependence compared to the ALICE data but the ratio of multiplicity in central to more peripheral events turns out to be roughly same. We also obtained results for the saturation scale Q_s and found that Q_s^{Pb} has a rather strong centrality dependence compared to Q_s^p which remains roughly the same for peripheral collisions.

Subsequently, we characterize the event geometry using the eccentricities ε_n and the initial state momentum anisotropy using the anisotropic energy flow ϵ_p and the azimuthal anisotropy of the produced gluons v_2^g. We find that the event geometry is correlated across large rapidity intervals whereas initial state momentum correlations are relatively short range in rapidity. Based on our results, we conclude that that experimental observations of collectivity in small systems which extend across large rapidity separations, should likely be interpreted as an imprints of the initial event geometry.

In future, we would take a step forward and calculate observables like anisotropic flow coefficients after full hydrodynamic evolution by appending the 3 D IP-Glasma code to MUSIC [162], which is a numerical software for relativistic viscous hydrodynamics. We will also try to work on the caveats of this framework as discussed in [41] in order to gain additional insights into the small-systems.

Chapter 6

Conclusion

In this chapter, we summarize our main results and provide outline for the future extension of the work done. We refer the readers to the Sections 3.4, 4.5 and 5.4 for a detailed overview of the respective chapters.

The central goal of this work is to relax the assumption of boost invariance and provide a first principle insight into the longitudinal structure of heavy-ion collisions within the color glass condensate framework.

We first developed a framework to perform $3+1$ D classical Yang-Mills simulations which takes the finite-thickness of the colliding nuclei into account and hence provides a legitimate way of studying the initial energy deposition in heavy-ion collisions. In contrast to the boost-invariant collision where initial conditions are available at the boundary of forward light-cone, the collision of nuclei with finite longitudinal extent relies on the solution of incoming nuclei prior to the collision. Therefore the resultant numerical simulation provides a natural insight into the collision itself as well as the dynamics of the Glasma.

Within a simple model of the color charge distribution of each nucleus, we perform a detailed investigation of the dynamics during and shortly after the collision as a function of the longitudinal thickness of the colliding nuclei $Q_s R_\gamma$ and demonstrate that for $Q_s R_\gamma \to 0$, boost-invariant limit is recovered. However, for non negligible values of $Q_s R_\gamma$, significant violation of boost-invariance are observed.

Subsequently, we develop a more physical model that connects the color charge distributions in the colliding nuclei to the parton distributions inside the nuclei. In

this model, the large scale structure of the nucleus is obtained by 3 D Monte Carlo Glauber model whereas the small scale fluctuations are determined by parameterizing small-x TMDs. Based on this model, we studied the pre-equilibrium state at two different center of mass energies and obtained the first result regarding the three dimensional structure and its fluctuation which ceases with the increasing $\sqrt{s}$. We further used this model to study the decorrelation of n-th order anisotropic flow and obtained a significant result for the event-plane decorrelation that encourages us to make a direct comparison with the experimental data in the future.

Due to high computational cost, our results were limited to a small rapidity window and head-on collisions at RHIC energies, and therefore in the future we would like to optimize the framework in order to access a larger rapidity range and to systematically examine the $3 + 1$ D Yang Mills dynamics as a function of the centrality of events. In addition to improving numerical simulations, it would be interesting to investigate the production of quark-antiquark pairs in the background of non-Abelian gauge fields.

In Chapter 4, we considered the collision of extended nuclei in the dilute limit of the color glass condensate and obtained the first analytical results for the longitudinal profiles of the initial energy deposition in heavy-ion collisions.

By assuming perturbation on top of the pre-collision gauge fields, we determine the analytical expressions for the color fields produced in the forward light cone by solving the linearized Yang-Mills equation. We then employ a MV-like model with factorized longitudinal dependence of nuclear collision geometry and use it to evaluate the transverse pressure. With this, we compare the rapidity profiles of (semi-)analytic results in dilute approximation with the 3+1 D CYM implementation and obtain excellent agreement in the dilute regime. Beyond the dilute regime, the energy deposition is over-estimated but the rapidity profiles are captured quite well which suggests that the denseness of a colliding system can be factorized into some scaling constant. We also examined the coherence length ϵ/R for two different limits and found that both approach the same boost-invariant plateau as the thickness of the colliding nuclei decreases.

Our analytic expression allows for an efficient way of determining the energy momentum tensor $T^{\mu\nu}$ to desirable rapidity range. In the future, we would like to develop new Monte Carlo event generators for the initial state of heavy ion collisions, which will open the door to exciting phenomenological studies such as Chiral-Vortical effect [131, 132] and Chiral- Magnetic effect [133–135].

In the last chapter, we have worked on a phenomenological application of $3 + 1$ D color glass condensate model with a motive to understand the origin of collectivity in small system at LHC energies. Since our framework for $3+1$ D collisions still needs to be optimized, we follow the approach of extending the impact parameter dependent Glasma model (IP-Glasma) to 3D using JIMWLK rapidity evolution of the incoming nuclear gluon distribution [41] to study p+Pb collisions at $\sqrt{s} = 5.02$ TeV.

We first study the rapidity profiles of the saturation scale Q_s and the system size $S_\perp$ at different centralities, and find that Q_s^{Pb} has a rather strong centrality dependence compared to Q_s^p which remains roughly the same for more peripheral events. We then investigate the non-trivial rapidity dependence of the observables and find that the event geometry is correlated across large rapidity intervals whereas initial state momentum correlations are relatively short range in rapidity. Based on this observation, we rule out the understanding of ridge in high multiplicity pp and pA collisions based on the initial state momentum correlations. In future, we will be interested in doing more phenomenology by coupling the IP-Glasma framework to MUSIC [162].

$$p_T = \frac{g^2}{2} N_c(N_c^2 - 1) \int_{p,q} \int_0^\infty dZ^+ \int_0^\infty dZ^- \int_{-2Z^+}^{+2Z^+} d\delta z^+ \int_{-2Z^-}^{+2Z^-} d\delta z^- p_\perp^2 q_\perp^2 C_A(p_\perp) C_B(q_\perp) \times$$

$$T_A(x^+ - Z^+) T_B(x^- - Z^-) U_A(\delta z^+) U_B(\delta z^-) J_0(|p + q|\tau_z) J_0(|p + q|\tau_{\bar{z}}) \qquad (6.1)$$

Appendix A

Discretization effect and approach to the continuum limit

Below we provide additional results for simulations where we vary the various discretization parameters, to illustrate the results presented in the main part of this work do not suffer from significant discretization artifacts.

We present a compact summary of the results in Fig. A.1, where for a fixed value of $Q_s t \simeq 4$, subtracted T^{00} and T^{0z} components of the energy momentum tensor are shown for the thick nuclei ($Q_s R_\gamma = 0.5$). In the first two panels: T^{00} obtained with the lattice discretization used throughout the manuscript ($R_\gamma/a_z = 16; a_t/a_z = 0.08$) is compared against the values obtained with finer longitudinal lattice spacing ($R_\gamma/a_z = 64$) and finer time step ($a_t/a_z = 0.04$). Lattice dimension is taken to be $128^2 \times 1024$ and $128^2 \times 2048$ for $R_\gamma/a_z = 16$ and $R_\gamma/a_z = 64$ respectively. We observe that approaching the continuum limit doesn't shrink the spurious fields in the proximity of light cone. In the other two panels, similar result is shown for T^{0z}, which again shows that the effect of these contributions do not change with finer lattice spacing.

After ruling out the lattice discretization artifact, one could argue that the possible explanation for the huge spikes near the light cone might lie within the numerical scheme. To verify this, we show our results (SSPS) along with the newly obtained results from the people doing 3D simulation with Color Particle in cell (CPIC) Method (pyglams3d) for different values of $Q_s t$ in Fig. A.2. Despite a completely different
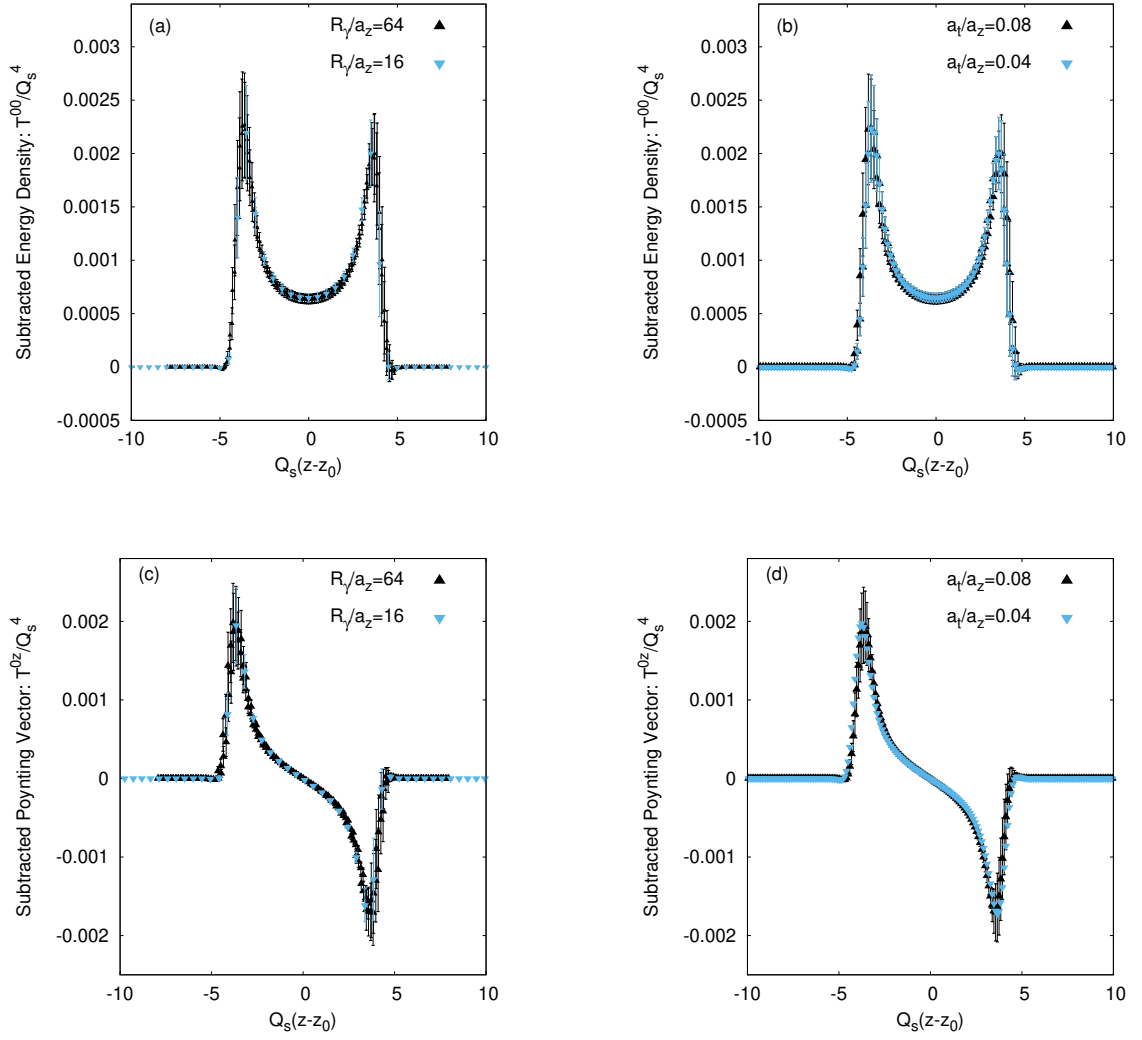
Figure A.1: Discretization effects on the various components of the energy momentum tensor for $Q_s R_\gamma = 0.5$ at $Q_s t \simeq 4$. Effect of finer longitudinal lattice spacing $a_z \to 0$ is shown in panel (a) and (c) whereas that of finer time discretization $a_t/a_z \to 0$ is shown in panel (b) and (d).

numerical scheme, we witness the exact same behaviour which convinces us to do some analytical studies in the dilute limit in future.
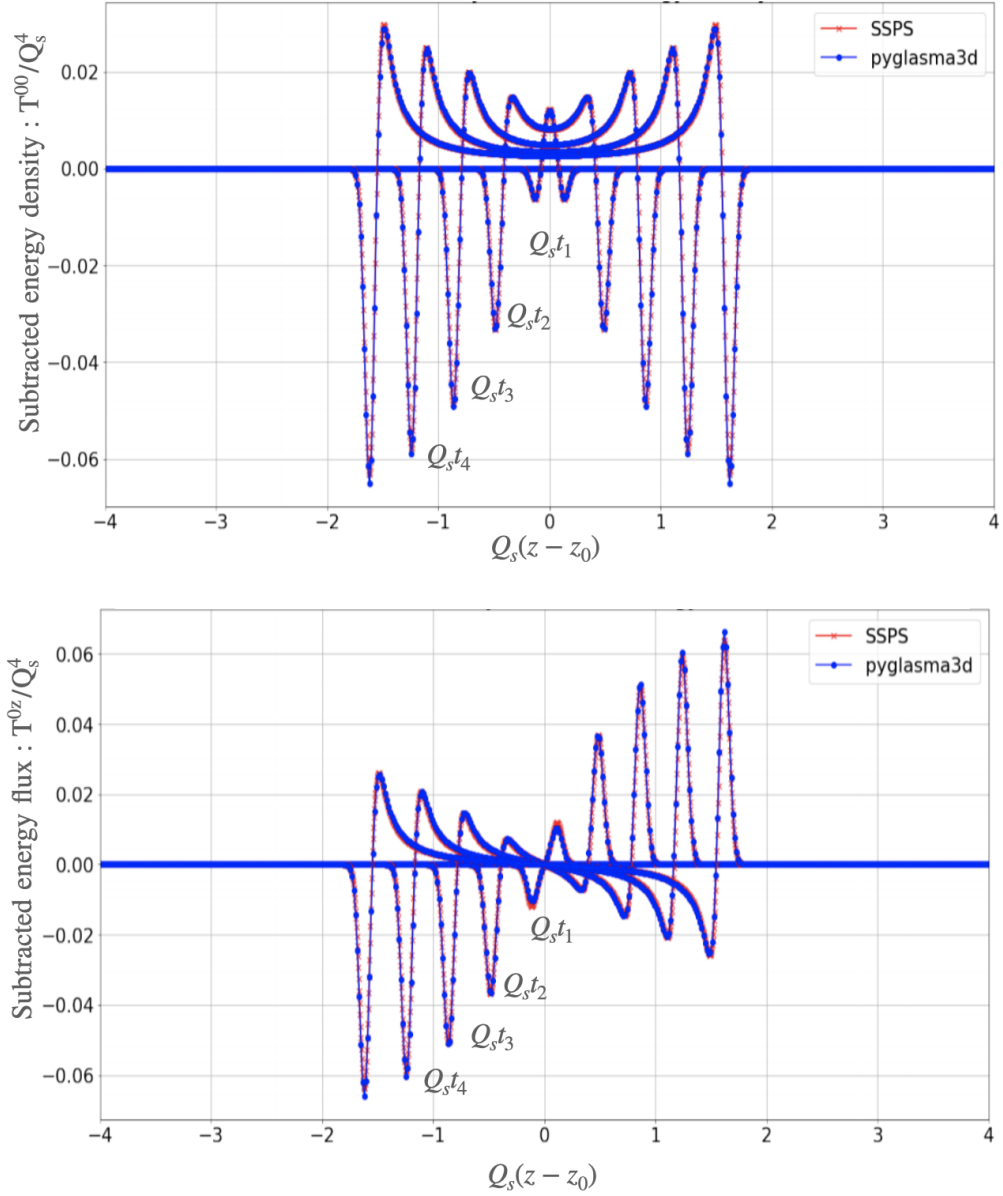
Figure A.2: Subtracted energy density and energy flux, T^{00} (top) and T^{0z} (bottom) for different times $Q_s t_{1,2,...}$ obtained from two different numerical schemes. These plots were provided by David Müller

Appendix B

Analytical results for boost-invariant collisions

In the boost-invariant limit, the color potential in the sources $(4.39) - (4.41)$ can be regularised as

$$\phi_{A/B}(x^\pm, x) \equiv \delta(x^\pm)\phi_{A/B}(x_\perp)$$

The delta function in the above expression simplifies the form of the dummy field in (4.51) as

$$a_d(x^+, x^-, p_\perp, q_\perp) = \frac{g}{2} f_{abc} t^c \tilde{\phi}_A^a(p_\perp) \tilde{\phi}_B^b(q_\perp) J_0\left(|p+q|\sqrt{2x^+x^-}\right) \qquad \text{(B.1)}$$

The different components of the perturbed gauge fields can be obtained by plugging the above expression for the dummy field in $(4.52) - (4.54)$. Since prominent features of the boost-invariant Glasma are easily reflected in the proper time-rapidity coordinate system, one can apply a coordinate transformation

$$a_\tau = \frac{1}{\tau}(x^+ a^- + x^- a^+) = a^\tau$$
$$a_\eta = (x^+ a^- - x^- a^+) = -\tau^2 a^\eta$$

to obtain the gauge fields in $\tau - \eta$ coordinates. With this, we can evaluate the different components of electric and magnetic fields using $(2.98) - (2.101)$. As we have already performed a detailed calculation for longitudinal electric and longitudinal magnetic field in Section 4.3, we abstain ourselves from rederiving it and simply replace the
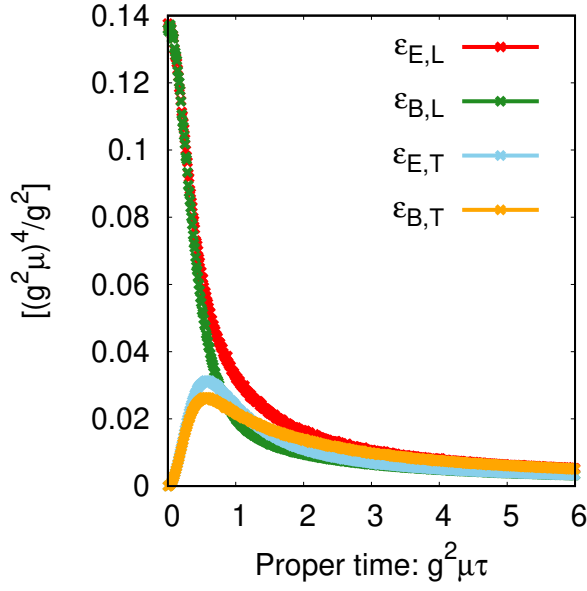
Figure B.1: Longitudinal and transverse component of electric and magnetic field, computed (semi-) analytically for SU(3) gauge group.

Gaussian function T and U in (4.74) and (4.82) with delta function to obtain the required expression in $2+1$ D. The different components of the electric and magnetic fields are then given as [1]

$$\varepsilon_{B,L} = \frac{g^2}{2} N_c (N_c^2 - 1) \int_{p,q} C_A(p_\perp) C_B(q_\perp) J_0^2(|p+q|\tau)(p \times q)^2 \qquad \text{(B.2)}$$

$$\varepsilon_{E,L} = \frac{g^2}{2} N_c (N_c^2 - 1) \int_{p,q} C_A(p_\perp) C_B(q_\perp) J_0^2(|p+q|\tau)(p \cdot q)^2 \qquad \text{(B.3)}$$

$$\varepsilon_{B,T} = \frac{g^2}{2} N_c (N_c^2 - 1) \int_{p,q} C_A(p_\perp) C_B(q_\perp) J_1^2(|p+q|\tau)(p \cdot q)^2 \qquad \text{(B.4)}$$

$$\varepsilon_{E,T} = \frac{g^2}{2} N_c (N_c^2 - 1) \int_{p,q} C_A(p_\perp) C_B(q_\perp) J_1^2(|p+q|\tau)(p \times q)^2 \qquad \text{(B.5)}$$

where $\tau = \sqrt{2x^+ x^-}$, and $p \times q$ and $p \cdot q$ are the cross and dot product of two dimensional vector p and q. These results agree with the analytical calculation done

---

[1] A calculation similar to the one in section 4.3 can be carried out to obtain the transverse components.

for dilute Glasma in [86, 129, 130]. On summing the two contributions – $\varepsilon_{B,L}$ and $\varepsilon_{E,L}$ – one obtains the transverse pressure p_T

$$p_T = \frac{g^2}{2}N_c(N_c^2-1)\int_{p,q} C_A(p_\perp)C_B(q_\perp)J_0^2(|p+q|\tau)p_\perp^2 q_\perp^2 \qquad \text{(B.6)}$$

In Fig. B.1, we plot the above expressions for the longitudinal and transverse components of electric and magnetic field as a function of proper-time. As already seen in the literature [86, 129, 130], the evolution starts with non-zero longitudinal electric and magnetic field which are equal at $\tau = 0$ and then slowly decoheres to generate the transverse fields. We also note that the longitudinal magnetic field is suppressed compared to longitudinal electric field, as already observed in the fully-non perturbative simulation in Fig 3.5.

Appendix C

IP-Sat Model

The impact parameter dependent dipole saturation model (IP-Sat) [147] is a model to extract the saturation scale by fitting the dipole cross section to Deep Inelastic Scattering (DIS) data [147, 148]. By introducing the impact parameter of nucleon into the dipole picture, its refines the Golec-Biernat–Wüsthoff (GBW) dipole model [163, 164]. The total cross-section in this model for a dipole with color charges at points $x_\perp$ and $y_\perp$ to pass through a gluon cloud is given as

$$\sigma_{q\bar{q}} = \frac{\pi^2}{N_c} r^2 \alpha_s(\mu^2) xg(x, \mu^2) \tag{C.1}$$

where N_c is number of colors, α_s is coupling constant, $r = |x_\perp - y_\perp|$ is the size of the dipole and $xg(x, \mu^2)$ is the gluon density at some scale μ^2 of interaction. The probability that the dipole at an impact parameter $b = |x(_\perp + y_\perp)/2|$ does not encounter an inelastic scattering on passing through a thin slice dz of the gluon cloud is given as

$$P(b) = 1 - \sigma_{q\bar{q}} \rho(b, z) dz \tag{C.2}$$

where $\rho(b, z)$ is the gluon density normalized as $\int d^2 b dz \rho(b, z) = 1$. Now, the probability for no scattering on passing through the entire proton is given by taking the square of scattering matrix element $S(b)$ which in principle is obtained by exponentiating the above result

$$|S(b)|^2 = \exp\left(-\sigma_{q\bar{q}} \int \rho(b, z) dz\right) \tag{C.3}$$

where $\int \rho(b, z)dz = T(b)$ and $T(b)$ is defined as the thickness function. which is normally taken to be Gaussian

$$T(b) = \frac{1}{2\pi B_G} \exp\left(-b^2/2B_G\right) \tag{C.4}$$

We note that the parameter B_G and $xg(x, \mu^2)$ are obtained by from the fit to the DIS data. The cross section for inelastic scattering at a given impact parameter is given as

$$\frac{d\sigma_{q\bar{q}}}{d^b} = 2[1 - \text{Re S(b)}] = 2\left[1 - \exp\left(-\frac{\pi^2}{2N_c}r^2\alpha_s^2(\mu^2)xg(x, \mu^2)T(b)\right)\right] \tag{C.5}$$

We refer the readers to [147] for exploring various properties of the above dipole cross section. The saturation scale Q_s for a fixed b is obtained by setting a condition that the dipole amplitude $D(r, b) = 1 - \text{Re S(b)}$ is equal to $1 - \exp(-\theta)$ such that

$$Q_s^2 = \frac{\theta}{r_s^2} \tag{C.6}$$

where θ refers to a reference value of dipole amplitude for which saturation is not yet achieved. For real time lattice simulation, dipole amplitude is computed using the correlators of Wilson line as

$$D(b, r) = \frac{1}{N_c}\text{Tr}\left\langle 1 - V^\dagger\left(b + \frac{r}{2}\right)V\left(b - \frac{r}{2}\right)\right\rangle \tag{C.7}$$

The saturation scale Q_s is used to provide the initial color charge density distribution. IP-Glasma [18, 19] which is one of the most successful model for the boost-invariant collision combines this model with a $2 + 1$ D classical Yang-Mills implementation in order to explore the initial state of heavy-ion collisions.

References

[1] Soeren Schlichting and Pragya Singh. '3-D structure of the Glasma initial state – Breaking boost-invariance by collisions of extended shock waves in classical Yang-Mills theory'. In: *Phys. Rev. D* 103.1 (2021), p. 014003. DOI: 10.1103/PhysRevD.103.014003. arXiv: 2010.11172 [hep-ph].

[2] Ulrich W. Heinz and Maurice Jacob. 'Evidence for a new state of matter: An Assessment of the results from the CERN lead beam program'. In: (Jan. 2000). arXiv: nucl-th/0002042.

[3] Miklos Gyulassy and Larry McLerran. 'New forms of QCD matter discovered at RHIC'. In: *Nucl. Phys. A* 750 (2005). Ed. by D. Rischke and G. Levin, pp. 30–63. DOI: 10.1016/j.nuclphysa.2004.10.034. arXiv: nucl-th/0405013.

[4] David J. Gross and Frank Wilczek. 'Ultraviolet Behavior of Nonabelian Gauge Theories'. In: *Phys. Rev. Lett.* 30 (1973). Ed. by J. C. Taylor, pp. 1343–1346. DOI: 10.1103/PhysRevLett.30.1343.

[5] H. David Politzer. 'Reliable Perturbative Results for Strong Interactions?' In: *Phys. Rev. Lett.* 30 (1973). Ed. by J. C. Taylor, pp. 1346–1349. DOI: 10.1103/PhysRevLett.30.1346.

[6] K. Adcox et al. 'Formation of dense partonic matter in relativistic nucleus-nucleus collisions at RHIC: Experimental evaluation by the PHENIX collaboration'. In: *Nucl. Phys. A* 757 (2005), pp. 184–283. DOI: 10.1016/j.nuclphysa.2005.03.086. arXiv: nucl-ex/0410003.

[7] I. Arsene et al. 'Quark gluon plasma and color glass condensate at RHIC? The Perspective from the BRAHMS experiment'. In: *Nucl. Phys. A* 757 (2005), pp. 1–27. DOI: 10.1016/j.nuclphysa.2005.02.130. arXiv: nucl-ex/0410020.

[8] Paul Romatschke and Ulrike Romatschke. 'Viscosity Information from Relativistic Nuclear Collisions: How Perfect is the Fluid Observed at RHIC?' In: *Phys. Rev. Lett.* 99 (2007), p. 172301. DOI: 10.1103/PhysRevLett.99.172301. arXiv: 0706.1522 [nucl-th].

[9] Patrick Steinbrecher. 'The QCD crossover at zero and non-zero baryon densities from Lattice QCD'. In: *Nucl. Phys. A* 982 (2019). Ed. by Federico Antinori et al., pp. 847–850. DOI: 10.1016/j.nuclphysa.2018.08.025. arXiv: 1807.05607 [hep-lat].

[10] N. Brambilla et al. 'QCD and Strongly Coupled Gauge Theories: Challenges and Perspectives'. In: *Eur. Phys. J. C* 74.10 (2014), p. 2981. DOI: 10.1140/epjc/s10052-014-2981-5. arXiv: 1404.3723 [hep-ph].

[11]   Aleksas Mazeliauskas. *Equilibration and collective effects in QCD kinetic theory.* Mazeliauskas_A.pdf. July 2021.

[12]   Soeren Schlichting and Derek Teaney. 'The First fm/c of Heavy-Ion Collisions'. In: *Ann. Rev. Nucl. Part. Sci.* 69 (2019), pp. 447–476. DOI: 10.1146/annurev-nucl-101918-023825. arXiv: 1908.02113 [nucl-th].

[13]   Jürgen Berges et al. 'QCD thermalization: Ab initio approaches and interdisciplinary connections'. In: *Rev. Mod. Phys.* 93.3 (2021), p. 035003. DOI: 10.1103/RevModPhys.93.035003. arXiv: 2005.12299 [hep-th].

[14]   Francesco Becattini. 'Freeze-out dynamics in heavy-ion collisions: Recent advances'. In: *Pramana* 84.5 (2015), pp. 747–755. DOI: 10.1007/s12043-015-0977-9.

[15]   H. -J. Drescher and Y. Nara. 'Effects of fluctuations on the initial eccentricity from the Color Glass Condensate in heavy ion collisions'. In: *Phys. Rev. C* 75 (2007), p. 034905. DOI: 10.1103/PhysRevC.75.034905. arXiv: nucl-th/0611017.

[16]   Hans-Joachim Drescher and Yasushi Nara. 'Eccentricity fluctuations from the color glass condensate at RHIC and LHC'. In: *Phys. Rev. C* 76 (2007), p. 041903. DOI: 10.1103/PhysRevC.76.041903. arXiv: 0707.0249 [nucl-th].

[17]   Michael L. Miller et al. 'Glauber modeling in high energy nuclear collisions'. In: *Ann. Rev. Nucl. Part. Sci.* 57 (2007), pp. 205–243. DOI: 10.1146/annurev.nucl.57.090506.123020. arXiv: nucl-ex/0701025.

[18]   Bjoern Schenke, Prithwish Tribedy and Raju Venugopalan. 'Fluctuating Glasma initial conditions and flow in heavy ion collisions'. In: *Phys. Rev. Lett.* 108 (2012), p. 252301. DOI: 10.1103/PhysRevLett.108.252301. arXiv: 1202.6646 [nucl-th].

[19]   Bjoern Schenke, Prithwish Tribedy and Raju Venugopalan. 'Event-by-event gluon multiplicity, energy density, and eccentricities in ultrarelativistic heavy-ion collisions'. In: *Phys. Rev. C* 86 (2012), p. 034908. DOI: 10.1103/PhysRevC.86.034908. arXiv: 1206.6805 [hep-ph].

[20]   J. Scott Moreland, Jonah E. Bernhard and Steffen A. Bass. 'Alternative ansatz to wounded nucleon and binary collision scaling in high-energy nuclear collisions'. In: *Phys. Rev. C* 92.1 (2015), p. 011901. DOI: 10.1103/PhysRevC.92.011901. arXiv: 1412.4708 [nucl-th].

[21]   H. Niemi, K. J. Eskola and R. Paatelainen. 'Event-by-event fluctuations in a perturbative QCD + saturation + hydrodynamics model: Determining QCD matter shear viscosity in ultrarelativistic heavy-ion collisions'. In: *Phys. Rev. C* 93.2 (2016), p. 024907. DOI: 10.1103/PhysRevC.93.024907. arXiv: 1505.02677 [hep-ph].

[22]   B. B. Back et al. 'Forward-backward multiplicity correlations in s(NN)**(1/2) = 200-GeV Au + Au collisions'. In: *Phys. Rev. C* 74 (2006), p. 011901. DOI: 10.1103/PhysRevC.74.011901. arXiv: nucl-ex/0603026.

[23]   B. I. Abelev et al. 'Growth of Long Range Forward-Backward Multiplicity Correlations with Centrality in Au+Au Collisions at s(NN)**(1/2) = 200-

GeV'. In: *Phys. Rev. Lett.* 103 (2009), p. 172301. DOI: `10.1103/PhysRevLett.103.172301`. arXiv: `0905.0237 [nucl-ex]`.

[24] Vardan Khachatryan et al. 'Evidence for transverse momentum and pseudorapidity dependent event plane fluctuations in PbPb and pPb collisions'. In: *Phys. Rev. C* 92.3 (2015), p. 034911. DOI: `10.1103/PhysRevC.92.034911`. arXiv: `1503.01692 [nucl-ex]`.

[25] Morad Aaboud et al. 'Measurement of longitudinal flow decorrelations in Pb+Pb collisions at $\sqrt{s_{\mathrm{NN}}} = 2.76$ and 5.02 TeV with the ATLAS detector'. In: *Eur. Phys. J. C* 78.2 (2018), p. 142. DOI: `10.1140/epjc/s10052-018-5605-7`. arXiv: `1709.02301 [nucl-ex]`.

[26] Francois Gelis et al. 'The Color Glass Condensate'. In: *Ann. Rev. Nucl. Part. Sci.* 60 (2010), pp. 463–489. DOI: `10.1146/annurev.nucl.010909.083629`. arXiv: `1002.0333 [hep-ph]`.

[27] F. Gelis. 'Color Glass Condensate and Glasma'. In: *Int. J. Mod. Phys. A* 28 (2013), p. 1330001. DOI: `10.1142/S0217751X13300019`. arXiv: `1211.3327 [hep-ph]`.

[28] T. Lappi and L. McLerran. 'Some features of the glasma'. In: *Nucl. Phys. A* 772 (2006), pp. 200–212. DOI: `10.1016/j.nuclphysa.2006.04.001`. arXiv: `hep-ph/0602189`.

[29] Charles Gale et al. 'Event-by-event anisotropic flow in heavy-ion collisions from combined Yang-Mills and viscous fluid dynamics'. In: *Phys. Rev. Lett.* 110.1 (2013), p. 012302. DOI: `10.1103/PhysRevLett.110.012302`. arXiv: `1209.6330 [nucl-th]`.

[30] Scott McDonald et al. 'Hydrodynamic predictions for Pb+Pb collisions at 5.02 TeV'. In: *Phys. Rev. C* 95.6 (2017), p. 064913. DOI: `10.1103/PhysRevC.95.064913`. arXiv: `1609.02958 [hep-ph]`.

[31] Prithwish Tribedy and Raju Venugopalan. 'QCD saturation at the LHC: Comparisons of models to p + p and A + A data and predictions for p + Pb collisions'. In: *Phys. Lett. B* 710 (2012). [Erratum: Phys.Lett.B 718, 1154–1154 (2013)], pp. 125–133. DOI: `10.1016/j.physletb.2012.02.047`. arXiv: `1112.2445 [hep-ph]`.

[32] Rainer J. Fries, Joseph I. Kapusta and Yang Li. 'From color fields to quark gluon plasma'. In: *Nucl. Phys. A* 774 (2006). Ed. by T. Csorgo et al., pp. 861–864. DOI: `10.1016/j.nuclphysa.2006.06.152`. arXiv: `hep-ph/0511101`.

[33] Kenji Fukushima. 'Initial fields and instability in the classical model of the heavy-ion collision'. In: *Phys. Rev. C* 76 (2007). [Erratum: Phys.Rev.C 77, 029901 (2007)], p. 021902. DOI: `10.1103/PhysRevC.76.021902`. arXiv: `0711.2634 [hep-ph]`.

[34] Hirotsugu Fujii, Kenji Fukushima and Yoshimasa Hidaka. 'Initial energy density and gluon distribution from the Glasma in heavy-ion collisions'. In: *Phys. Rev. C* 79 (2009), p. 024909. DOI: `10.1103/PhysRevC.79.024909`. arXiv: `0811.0437 [hep-ph]`.

[35] Guangyao Chen et al. 'Early Time Dynamics of Gluon Fields in High Energy Nuclear Collisions'. In: *Phys. Rev. C* 92.6 (2015), p. 064912. DOI: 10.1103/PhysRevC.92.064912. arXiv: 1507.03524 [nucl-th].

[36] Tuomas Lappi and Sören Schlichting. 'Linearly polarized gluons and axial charge fluctuations in the Glasma'. In: *Phys. Rev. D* 97.3 (2018), p. 034034. DOI: 10.1103/PhysRevD.97.034034. arXiv: 1708.08625 [hep-ph].

[37] Javier L. Albacete, Pablo Guerrero-Rodríguez and Cyrille Marquet. 'Initial correlations of the Glasma energy-momentum tensor'. In: *JHEP* 01 (2019), p. 073. DOI: 10.1007/JHEP01(2019)073. arXiv: 1808.00795 [hep-ph].

[38] Giuliano Giacalone et al. 'Fluctuations in heavy-ion collisions generated by QCD interactions in the color glass condensate effective theory'. In: *Phys. Rev. C* 100.2 (2019), p. 024905. DOI: 10.1103/PhysRevC.100.024905. arXiv: 1902.07168 [nucl-th].

[39] Bjorn Schenke, Sangyong Jeon and Charles Gale. 'Higher flow harmonics from (3+1)D event-by-event viscous hydrodynamics'. In: *Phys. Rev. C* 85 (2012), p. 024901. DOI: 10.1103/PhysRevC.85.024901. arXiv: 1109.6289 [hep-ph].

[40] Piotr Bożek. 'Event-by-event viscous hydrodynamics for Cu–Au collisions at $\sqrt{s_{NN}}$=200 GeV'. In: *Phys. Lett. B* 717 (2012), pp. 287–290. DOI: 10.1016/j.physletb.2012.09.040. arXiv: 1208.1887 [nucl-th].

[41] Bjoern Schenke and Soeren Schlichting. '3D glasma initial state for relativistic heavy ion collisions'. In: *Phys. Rev. C* 94.4 (2016), p. 044907. DOI: 10.1103/PhysRevC.94.044907. arXiv: 1605.07158 [hep-ph].

[42] Scott McDonald, Sangyong Jeon and Charles Gale. 'Exploring Longitudinal Observables with 3+1D IP-Glasma'. In: *Nucl. Phys. A* 1005 (2021). Ed. by Feng Liu et al., p. 121771. DOI: 10.1016/j.nuclphysa.2020.121771. arXiv: 2001.08636 [nucl-th].

[43] Chun Shen and Björn Schenke. 'Dynamical initial state model for relativistic heavy-ion collisions'. In: *Phys. Rev. C* 97.2 (2018), p. 024907. DOI: 10.1103/PhysRevC.97.024907. arXiv: 1710.00881 [nucl-th].

[44] Tolga Altinoluk and Adrian Dumitru. 'Particle production in high-energy collisions beyond the shockwave limit'. In: *Phys. Rev. D* 94.7 (2016), p. 074032. DOI: 10.1103/PhysRevD.94.074032. arXiv: 1512.00279 [hep-ph].

[45] Tolga Altinoluk et al. 'CGC beyond eikonal accuracy: finite width target effects'. In: *EPJ Web Conf.* 112 (2016). Ed. by C. Marquet, B. Pire and F. Sabatie, p. 02001. DOI: 10.1051/epjconf/201611202001.

[46] Daniil Gelfand, Andreas Ipp and David Müller. 'Simulating collisions of thick nuclei in the color glass condensate framework'. In: *Phys. Rev. D* 94.1 (2016), p. 014020. DOI: 10.1103/PhysRevD.94.014020. arXiv: 1605.07184 [hep-ph].

[47] Andreas Ipp and David Müller. 'Broken boost invariance in the Glasma via finite nuclei thickness'. In: *Phys. Lett. B* 771 (2017), pp. 74–79. DOI: 10.1016/j.physletb.2017.05.032. arXiv: 1703.00017 [hep-ph].

[48] Andreas Ipp and David I. Müller. 'Progress on 3+1D Glasma simulations'. In: *Eur. Phys. J. A* 56.9 (2020), p. 243. DOI: 10.1140/epja/s10050-020-00241-6. arXiv: 2009.02044 [hep-ph].

[49] S. A. Bass et al. 'Signatures of quark gluon plasma formation in high-energy heavy ion collisions: A Critical review'. In: *J. Phys. G* 25 (1999), R1–R57. DOI: 10.1088/0954-3899/25/3/013. arXiv: hep-ph/9810281.

[50] B. I. Abelev et al. 'Long range rapidity correlations and jet production in high energy nuclear collisions'. In: *Phys. Rev. C* 80 (2009), p. 064912. DOI: 10.1103/PhysRevC.80.064912. arXiv: 0909.0191 [nucl-ex].

[51] Raghunath Sahoo. 'Possible Formation of QGP-droplets in Proton-Proton Collisions at the CERN Large Hadron Collider'. In: *AAPPS Bull.* 29.4 (2019), pp. 16–21. DOI: 10.22661/AAPPSBL.2019.29.4.16. arXiv: 1908.10566 [nucl-ex].

[52] Kevin Dusling, Wei Li and Björn Schenke. 'Novel collective phenomena in high-energy proton–proton and proton–nucleus collisions'. In: *Int. J. Mod. Phys. E* 25.01 (2016), p. 1630002. DOI: 10.1142/S0218301316300022. arXiv: 1509.07939 [nucl-ex].

[53] Sören Schlichting and Prithwish Tribedy. 'Collectivity in Small Collision Systems: An Initial-State Perspective'. In: *Adv. High Energy Phys.* 2016 (2016), p. 8460349. DOI: 10.1155/2016/8460349. arXiv: 1611.00329 [hep-ph].

[54] Bjoern Schenke, Chun Shen and Prithwish Tribedy. 'Hybrid Color Glass Condensate and hydrodynamic description of the Relativistic Heavy Ion Collider small system scan'. In: *Phys. Lett. B* 803 (2020), p. 135322. DOI: 10.1016/j.physletb.2020.135322. arXiv: 1908.06212 [nucl-th].

[55] Björn Schenke. 'The smallest fluid on earth'. In: (Feb. 2021). arXiv: 2102.11189 [nucl-th].

[56] Björn Schenke. 'Origins of collectivity in small systems'. In: *Nucl. Phys. A* 967 (2017). Ed. by Ulrich Heinz, Olga Evdokimov and Peter Jacobs, pp. 105–112. DOI: 10.1016/j.nuclphysa.2017.05.017. arXiv: 1704.03914 [nucl-th].

[57] Adrian Dumitru et al. 'Glasma flux tubes and the near side ridge phenomenon at RHIC'. In: *Nucl. Phys. A* 810 (2008), pp. 91–108. DOI: 10.1016/j.nuclphysa.2008.06.012. arXiv: 0804.3858 [hep-ph].

[58] Alex Kovner and Michael Lublinsky. 'Angular Correlations in Gluon Production at High Energy'. In: *Phys. Rev. D* 83 (2011), p. 034017. DOI: 10.1103/PhysRevD.83.034017. arXiv: 1012.3398 [hep-ph].

[59] Adrian Dumitru et al. 'The Ridge in proton-proton collisions at the LHC'. In: *Phys. Lett. B* 697 (2011), pp. 21–25. DOI: 10.1016/j.physletb.2011.01.024. arXiv: 1009.5295 [hep-ph].

[60] Alex Kovner and Michael Lublinsky. 'On Angular Correlations and High Energy Evolution'. In: *Phys. Rev. D* 84 (2011), p. 094011. DOI: 10.1103/PhysRevD.84.094011. arXiv: 1109.0347 [hep-ph].

[61] Kevin Dusling and Raju Venugopalan. 'Azimuthal collimation of long range rapidity correlations by strong color fields in high multiplicity hadron-hadron collisions'. In: *Phys. Rev. Lett.* 108 (2012), p. 262001. DOI: 10.1103/PhysRevLett.108.262001. arXiv: 1201.2658 [hep-ph].

[62] Eugene Levin and Amir H. Rezaeian. 'The Ridge from the BFKL evolution and beyond'. In: *Phys. Rev. D* 84 (2011), p. 034031. DOI: 10.1103/PhysRevD.84.034031. arXiv: 1105.3275 [hep-ph].

[63] Kevin Dusling and Raju Venugopalan. 'Explanation of systematics of CMS p+Pb high multiplicity di-hadron data at $\sqrt{s}_{NN}$ = 5.02 TeV'. In: *Phys. Rev. D* 87.5 (2013), p. 054014. DOI: 10.1103/PhysRevD.87.054014. arXiv: 1211.3701 [hep-ph].

[64] Kevin Dusling and Raju Venugopalan. 'Comparison of the color glass condensate to dihadron correlations in proton-proton and proton-nucleus collisions'. In: *Phys. Rev. D* 87.9 (2013), p. 094034. DOI: 10.1103/PhysRevD.87.094034. arXiv: 1302.7018 [hep-ph].

[65] Adrian Dumitru, Larry McLerran and Vladimir Skokov. 'Azimuthal asymmetries and the emergence of "collectivity" from multi-particle correlations in high-energy pA collisions'. In: *Phys. Lett. B* 743 (2015), pp. 134–137. DOI: 10.1016/j.physletb.2015.02.046. arXiv: 1410.4844 [hep-ph].

[66] Björn Schenke, Sören Schlichting and Raju Venugopalan. 'Azimuthal anisotropies in p+Pb collisions from classical Yang–Mills dynamics'. In: *Phys. Lett. B* 747 (2015), pp. 76–82. DOI: 10.1016/j.physletb.2015.05.051. arXiv: 1502.01331 [hep-ph].

[67] Larry McLerran and Vladimir Skokov. 'Finite Numbers of Sources, Particle Correlations and the Color Glass Condensate'. In: *Nucl. Phys. A* 947 (2016), pp. 142–154. DOI: 10.1016/j.nuclphysa.2015.12.005. arXiv: 1510.08072 [hep-ph].

[68] Bjoern Schenke et al. 'Mass ordering of spectra from fragmentation of saturated gluon states in high multiplicity proton-proton collisions'. In: *Phys. Rev. Lett.* 117.16 (2016), p. 162301. DOI: 10.1103/PhysRevLett.117.162301. arXiv: 1607.02496 [hep-ph].

[69] Kevin Dusling, Mark Mace and Raju Venugopalan. 'Multiparticle collectivity from initial state correlations in high energy proton-nucleus collisions'. In: *Phys. Rev. Lett.* 120.4 (2018), p. 042002. DOI: 10.1103/PhysRevLett.120.042002. arXiv: 1705.00745 [hep-ph].

[70] Kevin Dusling, Mark Mace and Raju Venugopalan. 'Parton model description of multiparticle azimuthal correlations in *pA* collisions'. In: *Phys. Rev. D* 97.1 (2018), p. 016014. DOI: 10.1103/PhysRevD.97.016014. arXiv: 1706.06260 [hep-ph].

[71] Mark Mace et al. 'Hierarchy of Azimuthal Anisotropy Harmonics in Collisions of Small Systems from the Color Glass Condensate'. In: *Phys. Rev. Lett.* 121.5 (2018). [Erratum: Phys.Rev.Lett. 123, 039901 (2019)], p. 052301. DOI: 10.1103/PhysRevLett.121.052301. arXiv: 1805.09342 [hep-ph].

[72] Mark Mace et al. 'Systematics of azimuthal anisotropy harmonics in proton–nucleus collisions at the LHC from the Color Glass Condensate'. In: *Phys. Lett. B* 788 (2019). [Erratum: Phys.Lett.B 799, 135006 (2019)], pp. 161–165. DOI: 10.1016/j.physletb.2018.09.064. arXiv: 1807.00825 [hep-ph].

[73] Alex Kovner and Vladimir V. Skokov. 'Does shape matter? v_2 vs eccentricity in small x gluon production'. In: *Phys. Lett. B* 785 (2018), pp. 372–380. DOI: 10.1016/j.physletb.2018.09.001. arXiv: 1805.09297 [hep-ph].

[74] Gert Aarts and Jan Smit. 'Real time dynamics with fermions on a lattice'. In: *Nucl. Phys. B* 555 (1999), pp. 355–394. DOI: 10.1016/S0550-3213(99) 00320-X. arXiv: hep-ph/9812413.

[75] Mark Mace et al. 'Non-equilibrium study of the Chiral Magnetic Effect from real-time simulations with dynamical fermions'. In: *Phys. Rev. D* 95.3 (2017), p. 036023. DOI: 10.1103/PhysRevD.95.036023. arXiv: 1612.02477 [hep-lat].

[76] A. Accardi et al. 'Electron Ion Collider: The Next QCD Frontier: Understanding the glue that binds us all'. In: *Eur. Phys. J. A* 52.9 (2016). Ed. by A. Deshpande, Z. E. Meziani and J. W. Qiu, p. 268. DOI: 10.1140/epja/i2016-16268-9. arXiv: 1212.1701 [nucl-ex].

[77] A. M. Stasto, Krzysztof J. Golec-Biernat and J. Kwiecinski. 'Geometric scaling for the total gamma* p cross-section in the low x region'. In: *Phys. Rev. Lett.* 86 (2001), pp. 596–599. DOI: 10.1103/PhysRevLett.86.596. arXiv: hep-ph/0007192.

[78] F. D. Aaron et al. 'Combined Measurement and QCD Analysis of the Inclusive e+- p Scattering Cross Sections at HERA'. In: *JHEP* 01 (2010), p. 109. DOI: 10.1007/JHEP01(2010)109. arXiv: 0911.0884 [hep-ex].

[79] Larry D. McLerran. 'The Color glass condensate and small x physics: Four lectures'. In: *Lect. Notes Phys.* 583 (2002). Ed. by Willibald Plessas and L. Mathelitsch, pp. 291–334. DOI: 10.1007/3-540-45792-5_8. arXiv: hep-ph/0104285.

[80] L. V. Gribov, E. M. Levin and M. G. Ryskin. 'Semihard Processes in QCD'. In: *Phys. Rept.* 100 (1983), pp. 1–150. DOI: 10.1016/0370-1573(83)90022-4.

[81] Alfred H. Mueller and Jian-wei Qiu. 'Gluon Recombination and Shadowing at Small Values of x'. In: *Nucl. Phys. B* 268 (1986), pp. 427–452. DOI: 10.1016/0550-3213(86)90164-1.

[82] Edmond Iancu and Raju Venugopalan. 'The Color glass condensate and high-energy scattering in QCD'. In: *Quark-gluon plasma 4*. Ed. by Rudolph C. Hwa and Xin-Nian Wang. Mar. 2003. DOI: 10.1142/9789812795533_0005. arXiv: hep-ph/0303204.

[83] Larry D. McLerran and Raju Venugopalan. 'Gluon distribution functions for very large nuclei at small transverse momentum'. In: *Phys. Rev. D* 49 (1994), pp. 3352–3355. DOI: 10.1103/PhysRevD.49.3352. arXiv: hep-ph/9311205.

[84] Larry D. McLerran and Raju Venugopalan. 'Computing quark and gluon distribution functions for very large nuclei'. In: *Phys. Rev. D* 49 (1994), pp. 2233–2241. DOI: 10.1103/PhysRevD.49.2233. arXiv: hep-ph/9309289.

[85] T. Lappi. 'Wilson line correlator in the MV model: Relating the glasma to deep inelastic scattering'. In: *Eur. Phys. J. C* 55 (2008), pp. 285–292. DOI: 10.1140/epjc/s10052-008-0588-4. arXiv: 0711.3039 [hep-ph].

[86] Alex Kovner, Larry D. McLerran and Heribert Weigert. 'Gluon production from nonAbelian Weizsacker-Williams fields in nucleus-nucleus collisions'. In:

Phys. Rev. D 52 (1995), pp. 6231–6237. DOI: `10.1103/PhysRevD.52.6231`. arXiv: `hep-ph/9502289`.

[87] Alex Kovner, Larry D. McLerran and Heribert Weigert. 'Gluon production at high transverse momentum in the McLerran-Venugopalan model of nuclear structure functions'. In: *Phys. Rev. D* 52 (1995), pp. 3809–3814. DOI: `10.1103/PhysRevD.52.3809`. arXiv: `hep-ph/9505320`.

[88] Alex Krasnitz and Raju Venugopalan. 'Nonperturbative computation of gluon minijet production in nuclear collisions at very high-energies'. In: *Nucl. Phys. B* 557 (1999), p. 237. DOI: `10.1016/S0550-3213(99)00366-1`. arXiv: `hep-ph/9809433`.

[89] Scott McDonald. 'Towards fully 3-dimensional simulations of heavy ion collisions in the IP-Glasma initial state framework'. PhD thesis. McGill U., 2020.

[90] T. Lappi. 'Energy density of the glasma'. In: *Phys. Lett. B* 643 (2006), pp. 11–16. DOI: `10.1016/j.physletb.2006.10.017`. arXiv: `hep-ph/0606207`.

[91] Paul Romatschke and Raju Venugopalan. 'A Weibel instability in the melting color glass condensate'. In: *Eur. Phys. J. A* 29 (2006), pp. 71–75. DOI: `10.1140/epja/i2005-10304-y`. arXiv: `hep-ph/0510292`.

[92] Paul Romatschke and Raju Venugopalan. 'The Unstable Glasma'. In: *Phys. Rev. D* 74 (2006), p. 045011. DOI: `10.1103/PhysRevD.74.045011`. arXiv: `hep-ph/0605045`.

[93] Kenji Fukushima and Francois Gelis. 'The evolving Glasma'. In: *Nucl. Phys. A* 874 (2012), pp. 108–129. DOI: `10.1016/j.nuclphysa.2011.11.003`. arXiv: `1106.1396 [hep-ph]`.

[94] Thomas Epelbaum and Francois Gelis. 'Fluctuations of the initial color fields in high energy heavy ion collisions'. In: *Phys. Rev. D* 88 (2013), p. 085015. DOI: `10.1103/PhysRevD.88.085015`. arXiv: `1307.1765 [hep-ph]`.

[95] Aleksi Kurkela et al. 'Matching the Nonequilibrium Initial Stage of Heavy Ion Collisions to Hydrodynamics with QCD Kinetic Theory'. In: *Phys. Rev. Lett.* 122.12 (2019), p. 122302. DOI: `10.1103/PhysRevLett.122.122302`. arXiv: `1805.01604 [hep-ph]`.

[96] Aleksi Kurkela et al. 'Effective kinetic description of event-by-event pre-equilibrium dynamics in high-energy heavy-ion collisions'. In: *Phys. Rev. C* 99.3 (2019), p. 034910. DOI: `10.1103/PhysRevC.99.034910`. arXiv: `1805.00961 [hep-ph]`.

[97] Yuri V. Kovchegov. 'Can thermalization in heavy ion collisions be described by QCD diagrams?' In: *Nucl. Phys. A* 762 (2005), pp. 298–325. DOI: `10.1016/j.nuclphysa.2005.08.009`. arXiv: `hep-ph/0503038`.

[98] Alex Krasnitz and Raju Venugopalan. 'The Initial gluon multiplicity in heavy ion collisions'. In: *Phys. Rev. Lett.* 86 (2001), pp. 1717–1720. DOI: `10.1103/PhysRevLett.86.1717`. arXiv: `hep-ph/0007108`.

[99] T. Lappi. 'Production of gluons in the classical field model for heavy ion collisions'. In: *Phys. Rev. C* 67 (2003), p. 054903. DOI: `10.1103/PhysRevC.67.054903`. arXiv: `hep-ph/0303076`.

[100] Tuomas Lappi and Jarkko Peuron. 'Plasmon mass scale in classical nonequilibrium gauge theory'. In: *Phys. Rev. D* 95.1 (2017), p. 014025. DOI: 10.1103/PhysRevD.95.014025. arXiv: 1610.03711 [hep-ph].

[101] K. Boguslavski et al. 'Spectral function for overoccupied gluodynamics from real-time lattice simulations'. In: *Phys. Rev. D* 98.1 (2018), p. 014006. DOI: 10.1103/PhysRevD.98.014006. arXiv: 1804.01966 [hep-ph].

[102] Juergen Berges et al. 'Universal attractor in a highly occupied non-Abelian plasma'. In: *Phys. Rev. D* 89.11 (2014), p. 114007. DOI: 10.1103/PhysRevD.89.114007. arXiv: 1311.3005 [hep-ph].

[103] Alex Krasnitz, Yasushi Nara and Raju Venugopalan. 'Coherent gluon production in very high-energy heavy ion collisions'. In: *Phys. Rev. Lett.* 87 (2001), p. 192302. DOI: 10.1103/PhysRevLett.87.192302. arXiv: hep-ph/0108092.

[104] Jamal Jalilian-Marian et al. 'The Intrinsic glue distribution at very small x'. In: *Phys. Rev. D* 55 (1997), pp. 5414–5428. DOI: 10.1103/PhysRevD.55.5414. arXiv: hep-ph/9606337.

[105] Jamal Jalilian-Marian et al. 'The Wilson renormalization group for low x physics: Towards the high density regime'. In: *Phys. Rev. D* 59 (1998), p. 014014. DOI: 10.1103/PhysRevD.59.014014. arXiv: hep-ph/9706377.

[106] Heribert Weigert. 'Unitarity at small Bjorken x'. In: *Nucl. Phys. A* 703 (2002), pp. 823–860. DOI: 10.1016/S0375-9474(01)01668-2. arXiv: hep-ph/0004044.

[107] S. Bondarenko, L. Lipatov and A. Prygarin. 'Effective action for reggeized gluons, classical gluon field of relativistic color charge and color glass condensate approach'. In: *Eur. Phys. J. C* 77.8 (2017), p. 527. DOI: 10.1140/epjc/s10052-017-5101-5. arXiv: 1706.00278 [hep-ph].

[108] Jean-Paul Blaizot, Edmond Iancu and Heribert Weigert. 'Nonlinear gluon evolution in path integral form'. In: *Nucl. Phys. A* 713 (2003), pp. 441–469. DOI: 10.1016/S0375-9474(02)01299-X. arXiv: hep-ph/0206279.

[109] T. Lappi and H. Mäntysaari. 'On the running coupling in the JIMWLK equation'. In: *Eur. Phys. J. C* 73.2 (2013), p. 2307. DOI: 10.1140/epjc/s10052-013-2307-z. arXiv: 1212.4825 [hep-ph].

[110] Sören Schlichting and Björn Schenke. 'The shape of the proton at high energies'. In: *Phys. Lett. B* 739 (2014), pp. 313–319. DOI: 10.1016/j.physletb.2014.10.068. arXiv: 1407.8458 [hep-ph].

[111] Alex Krasnitz and Raju Venugopalan. 'The Initial energy density of gluons produced in very high-energy nuclear collisions'. In: *Phys. Rev. Lett.* 84 (2000), pp. 4309–4312. DOI: 10.1103/PhysRevLett.84.4309. arXiv: hep-ph/9909203.

[112] Alex Krasnitz and Raju Venugopalan. 'On colliding ultrarelativistic nuclei on a transverse lattice'. In: *3rd International Conference on Physics and Astrophysics of Quark Gluon Plasma.* June 1997. arXiv: hep-ph/9706329.

[113] Andreas Ipp and David Müller. 'Implicit schemes for real-time lattice gauge theory'. In: *Eur. Phys. J. C* 78.11 (2018), p. 884. DOI: 10.1140/epjc/s10052-018-6323-x. arXiv: 1804.01995 [hep-lat].

[114] Jamal Jalilian-Marian et al. 'The Intrinsic glue distribution at very small x'. In: *Phys. Rev. D* 55 (1997), pp. 5414–5428. DOI: 10.1103/PhysRevD.55.5414. arXiv: hep-ph/9606337.

[115] Yuri V. Kovchegov. 'NonAbelian Weizsacker-Williams field and a two-dimensional effective color charge density for a very large nucleus'. In: *Phys. Rev. D* 54 (1996), pp. 5463–5469. DOI: 10.1103/PhysRevD.54.5463. arXiv: hep-ph/9605446.

[116] Andrei V. Belitsky, Xiang-dong Ji and Feng Yuan. 'Quark imaging in the proton via quantum phase space distributions'. In: *Phys. Rev. D* 69 (2004), p. 074014. DOI: 10.1103/PhysRevD.69.074014. arXiv: hep-ph/0307383.

[117] Xiang-dong Ji. 'Viewing the proton through 'color' filters'. In: *Phys. Rev. Lett.* 91 (2003), p. 062001. DOI: 10.1103/PhysRevLett.91.062001. arXiv: hep-ph/0304037.

[118] Elena Petreska. 'TMD gluon distributions at small x in the CGC theory'. In: *Int. J. Mod. Phys. E* 27.05 (2018), p. 1830003. DOI: 10.1142/S0218301318300035. arXiv: 1804.04981 [hep-ph].

[119] Fabio Dominguez et al. 'Universality of Unintegrated Gluon Distributions at small x'. In: *Phys. Rev. D* 83 (2011), p. 105005. DOI: 10.1103/PhysRevD.83.105005. arXiv: 1101.0715 [hep-ph].

[120] Krzysztof J. Golec-Biernat and M. Wusthoff. 'Saturation effects in deep inelastic scattering at low Q**2 and its implications on diffraction'. In: *Phys. Rev. D* 59 (1998), p. 014017. DOI: 10.1103/PhysRevD.59.014017. arXiv: hep-ph/9807513.

[121] Wojciech Broniowski and Piotr Bozek. 'Longitudinal correlations in the initial stages of ultra-relativistic nuclear collisions'. In: *EPJ Web Conf.* 141 (2017). Ed. by I. -K. Yoo, p. 05003. DOI: 10.1051/epjconf/201714105003. arXiv: 1610.09673 [nucl-th].

[122] Long-Gang Pang et al. 'Decorrelation of anisotropic flow along the longitudinal direction'. In: *Eur. Phys. J. A* 52.4 (2016), p. 97. DOI: 10.1140/epja/i2016-16097-x. arXiv: 1511.04131 [nucl-th].

[123] Long-Gang Pang et al. 'Longitudinal decorrelation of anisotropic flows in heavy-ion collisions at the CERN Large Hadron Collider'. In: *Phys. Rev. C* 91.4 (2015), p. 044904. DOI: 10.1103/PhysRevC.91.044904. arXiv: 1410.8690 [nucl-th].

[124] Tolga Altinoluk and Néstor Armesto. 'Particle correlations from the initial state'. In: *Eur. Phys. J. A* 56.8 (2020), p. 215. DOI: 10.1140/epja/s10050-020-00225-6. arXiv: 2004.08185 [hep-ph].

[125] Jean Paul Blaizot, Francois Gelis and Raju Venugopalan. 'High-energy pA collisions in the color glass condensate approach. 2. Quark production'. In: *Nucl. Phys. A* 743 (2004), pp. 57–91. DOI: 10.1016/j.nuclphysa.2004.07.006. arXiv: hep-ph/0402257.

[126] Hirotsugu Fujii, Francois Gelis and Raju Venugopalan. 'Quark pair production in high energy pA collisions: General features'. In: *Nucl. Phys. A* 780 (2006),

pp. 146–174. DOI: `10.1016/j.nuclphysa.2006.09.012`. arXiv: `hep-ph/0603099`.

[127]   Stephen Scott Adler et al. 'J/psi production and nuclear effects for d+Au and p+p collisions at s(NN)**(1/2) = 200-GeV'. In: *Phys. Rev. Lett.* 96 (2006), p. 012304. DOI: `10.1103/PhysRevLett.96.012304`. arXiv: `nucl-ex/0507032`.

[128]   B. Alessandro et al. 'A New measurement of J/psi suppression in Pb-Pb collisions at 158-GeV per nucleon'. In: *Eur. Phys. J. C* 39 (2005), pp. 335–345. DOI: `10.1140/epjc/s2004-02107-9`. arXiv: `hep-ex/0412036`.

[129]   Adrian Dumitru and Larry D. McLerran. 'How protons shatter colored glass'. In: *Nucl. Phys. A* 700 (2002), pp. 492–508. DOI: `10.1016/S0375-9474(01)01301-X`. arXiv: `hep-ph/0105268`.

[130]   Larry McLerran and Vladimir Skokov. 'Odd Azimuthal Anisotropy of the Glasma for pA Scattering'. In: *Nucl. Phys. A* 959 (2017), pp. 83–101. DOI: `10.1016/j.nuclphysa.2016.12.011`. arXiv: `1611.09870 [hep-ph]`.

[131]   L. Adamczyk et al. 'Global Λ hyperon polarization in nuclear collisions: evidence for the most vortical fluid'. In: *Nature* 548 (2017), pp. 62–65. DOI: `10.1038/nature23004`. arXiv: `1701.06657 [nucl-ex]`.

[132]   Jaroslav Adam et al. 'Global polarization of Λ hyperons in Au+Au collisions at $\sqrt{s_{NN}}$ = 200 GeV'. In: *Phys. Rev. C* 98 (2018), p. 014910. DOI: `10.1103/PhysRevC.98.014910`. arXiv: `1805.04400 [nucl-ex]`.

[133]   B. I. Abelev et al. 'Azimuthal Charged-Particle Correlations and Possible Local Strong Parity Violation'. In: *Phys. Rev. Lett.* 103 (2009), p. 251601. DOI: `10.1103/PhysRevLett.103.251601`. arXiv: `0909.1739 [nucl-ex]`.

[134]   Betty Abelev et al. 'Charge separation relative to the reaction plane in Pb-Pb collisions at $\sqrt{s_{NN}}$ = 2.76 TeV'. In: *Phys. Rev. Lett.* 110.1 (2013), p. 012301. DOI: `10.1103/PhysRevLett.110.012301`. arXiv: `1207.0900 [nucl-ex]`.

[135]   L. Adamczyk et al. 'Beam-energy dependence of charge separation along the magnetic field in Au+Au collisions at RHIC'. In: *Phys. Rev. Lett.* 113 (2014), p. 052302. DOI: `10.1103/PhysRevLett.113.052302`. arXiv: `1404.1433 [nucl-ex]`.

[136]   Pablo Guerrero-Rodrıguez and Tuomas Lappi. 'Evolution of initial stage fluctuations in the glasma'. In: *Phys. Rev. D* 104.1 (2021), p. 014011. DOI: `10.1103/PhysRevD.104.014011`. arXiv: `2102.09993 [hep-ph]`.

[137]   Margaret E. Carrington, Alina Czajka and Stanislaw Mrowczynski. 'Physical characteristics of glasma from the earliest stage of relativistic heavy ion collisions'. In: (May 2021). arXiv: `2105.05327 [hep-ph]`.

[138]   Kevin Dusling et al. 'Long range two-particle rapidity correlations in A+A collisions from high energy QCD evolution'. In: *Nucl. Phys. A* 836 (2010), pp. 159–182. DOI: `10.1016/j.nuclphysa.2009.12.044`. arXiv: `0911.2720 [hep-ph]`.

[139]   T. Lappi, S. Srednyak and R. Venugopalan. 'Non-perturbative computation of double inclusive gluon production in the Glasma'. In: *JHEP* 01 (2010), p. 066. DOI: `10.1007/JHEP01(2010)066`. arXiv: `0911.2068 [hep-ph]`.

[140] Kevin Dusling and Raju Venugopalan. 'Evidence for BFKL and saturation dynamics from dihadron spectra at the LHC'. In: *Phys. Rev. D* 87.5 (2013), p. 051502. DOI: 10.1103/PhysRevD.87.051502. arXiv: 1210.3890 [hep-ph].

[141] Francois Gelis, Tuomas Lappi and Raju Venugopalan. 'High energy factorization in nucleus-nucleus collisions'. In: *Phys. Rev. D* 78 (2008), p. 054019. DOI: 10.1103/PhysRevD.78.054019. arXiv: 0804.2630 [hep-ph].

[142] Francois Gelis, Tuomas Lappi and Raju Venugopalan. 'High energy factorization in nucleus-nucleus collisions. 3. Long range rapidity correlations'. In: *Phys. Rev. D* 79 (2009), p. 094017. DOI: 10.1103/PhysRevD.79.094017. arXiv: 0810.4829 [hep-ph].

[143] Francois Gelis, Tuomas Lappi and Raju Venugopalan. 'High energy factorization in nucleus-nucleus collisions. II. Multigluon correlations'. In: *Phys. Rev. D* 78 (2008), p. 054020. DOI: 10.1103/PhysRevD.78.054020. arXiv: 0807.1306 [hep-ph].

[144] E. Iancu and D. N. Triantafyllopoulos. 'JIMWLK evolution for multi-particle production in Langevin form'. In: *JHEP* 11 (2013), p. 067. DOI: 10.1007/JHEP11(2013)067. arXiv: 1307.1559 [hep-ph].

[145] Larry D. McLerran and Raju Venugopalan. 'Green's functions in the color field of a large nucleus'. In: *Phys. Rev. D* 50 (1994), pp. 2225–2233. DOI: 10.1103/PhysRevD.50.2225. arXiv: hep-ph/9402335.

[146] J. Bartels, Krzysztof J. Golec-Biernat and H. Kowalski. 'A modification of the saturation model: DGLAP evolution'. In: *Phys. Rev. D* 66 (2002), p. 014001. DOI: 10.1103/PhysRevD.66.014001. arXiv: hep-ph/0203258.

[147] Henri Kowalski and Derek Teaney. 'An Impact parameter dipole saturation model'. In: *Phys. Rev. D* 68 (2003), p. 114005. DOI: 10.1103/PhysRevD.68.114005. arXiv: hep-ph/0304189.

[148] Amir H. Rezaeian et al. 'Analysis of combined HERA data in the Impact-Parameter dependent Saturation model'. In: *Phys. Rev. D* 87.3 (2013), p. 034002. DOI: 10.1103/PhysRevD.87.034002. arXiv: 1212.2974 [hep-ph].

[149] Bjoern Schenke, Chun Shen and Prithwish Tribedy. 'Running the gamut of high energy nuclear collisions'. In: *Phys. Rev. C* 102.4 (2020), p. 044905. DOI: 10.1103/PhysRevC.102.044905. arXiv: 2005.14682 [nucl-th].

[150] The official code repository of the IP-Glasma initial conditions is https://github.com/schenke/ipglasma. Here we used v1.0: https://github.com/schenke/ipglasma/releases.

[151] Jamal Jalilian-Marian et al. 'The BFKL equation from the Wilson renormalization group'. In: *Nucl. Phys. B* 504 (1997), pp. 415–431. DOI: 10.1016/S0550-3213(97)00440-9. arXiv: hep-ph/9701284.

[152] Jamal Jalilian-Marian et al. 'The Wilson renormalization group for low x physics: Towards the high density regime'. In: *Phys. Rev. D* 59 (1998), p. 014014. DOI: 10.1103/PhysRevD.59.014014. arXiv: hep-ph/9706377.

[153] Edmond Iancu, Andrei Leonidov and Larry D. McLerran. 'Nonlinear gluon evolution in the color glass condensate. 1.' In: *Nucl. Phys. A* 692 (2001),

pp. 583–645. DOI: 10.1016/S0375-9474(01)00642-X. arXiv: hep-ph/0011241.

[154] Edmond Iancu, Andrei Leonidov and Larry D. McLerran. 'The Renormalization group equation for the color glass condensate'. In: *Phys. Lett. B* 510 (2001), pp. 133–144. DOI: 10.1016/S0370-2693(01)00524-X. arXiv: hep-ph/0102009.

[155] Serguei Chatrchyan et al. 'Observation of Long-Range Near-Side Angular Correlations in Proton-Lead Collisions at the LHC'. In: *Phys. Lett. B* 718 (2013), pp. 795–814. DOI: 10.1016/j.physletb.2012.11.025. arXiv: 1210.5482 [nucl-ex].

[156] Jaroslav Adam et al. 'Centrality dependence of particle production in p-Pb collisions at $\sqrt{s_{NN}}$= 5.02 TeV'. In: *Phys. Rev. C* 91.6 (2015), p. 064905. DOI: 10.1103/PhysRevC.91.064905. arXiv: 1412.6828 [nucl-ex].

[157] Moritz Greif et al. 'Importance of initial and final state effects for azimuthal correlations in p+Pb collisions'. In: *Phys. Rev. D* 96.9 (2017), p. 091504. DOI: 10.1103/PhysRevD.96.091504. arXiv: 1708.02076 [hep-ph].

[158] Alex Krasnitz, Yasushi Nara and Raju Venugopalan. 'Elliptic flow of colored glass in high-energy heavy ion collisions'. In: *Phys. Lett. B* 554 (2003), pp. 21–27. DOI: 10.1016/S0370-2693(02)03272-0. arXiv: hep-ph/0204361.

[159] Giuliano Giacalone, Björn Schenke and Chun Shen. 'Observable signatures of initial state momentum anisotropies in nuclear collisions'. In: *Phys. Rev. Lett.* 125.19 (2020), p. 192301. DOI: 10.1103/PhysRevLett.125.192301. arXiv: 2006.15721 [nucl-th].

[160] Jean-Yves Ollitrault. 'Anisotropy as a signature of transverse collective flow'. In: *Phys. Rev. D* 46 (1992), pp. 229–245. DOI: 10.1103/PhysRevD.46.229.

[161] Adrian Dumitru and Andre V. Giannini. 'Initial state angular asymmetries in high energy p+A collisions: spontaneous breaking of rotational symmetry by a color electric field and C-odd fluctuations'. In: *Nucl. Phys. A* 933 (2015), pp. 212–228. DOI: 10.1016/j.nuclphysa.2014.10.037. arXiv: 1406.5781 [hep-ph].

[162] Bjorn Schenke, Sangyong Jeon and Charles Gale. 'Elliptic and triangular flow in event-by-event (3+1)D viscous hydrodynamics'. In: *Phys. Rev. Lett.* 106 (2011), p. 042301. DOI: 10.1103/PhysRevLett.106.042301. arXiv: 1009.3244 [hep-ph].

[163] Krzysztof J. Golec-Biernat and M. Wusthoff. 'Saturation effects in deep inelastic scattering at low Q**2 and its implications on diffraction'. In: *Phys. Rev. D* 59 (1998), p. 014017. DOI: 10.1103/PhysRevD.59.014017. arXiv: hep-ph/9807513.

[164] Krzysztof J. Golec-Biernat and M. Wusthoff. 'Saturation in diffractive deep inelastic scattering'. In: *Phys. Rev. D* 60 (1999), p. 114023. DOI: 10.1103/PhysRevD.60.114023. arXiv: hep-ph/9903358.